

Alma Mater Studiorum - Università di Bologna

DOTTORATO DI RICERCA IN
MECCANICA E SCIENZE AVANZATE DELL'INGEGNERIA
CICLO XXXI

Settore Concorsuale: Area 09/B1

Settore Scientifico Disciplinare: ING-IND/16

**Investigation into oil quenching
processes of steels to improve
sustainability by experiments
and multi-physical modelling**

Presentata da:

Fabio Lenzi

Supervisore:

Prof. G. Campana

Coordinatore Dottorato:

Prof. M. Carricato

Co-Supervisore:

Prof. I. S. Jawahir

Esame finale anno 2019

Alma Mater Studiorum - University of Bologna

PHD COURSE IN
MECHANICS AND ADVANCED ENGINEERING SCIENCES
CYCLE XXXI

Concoursuale sector: Area 09/B1

Scientific Sector: ING-IND/16

**Investigation into oil quenching
processes of steels to improve
sustainability by experiments
and multi-physical modelling**

PhD Candidate:

Fabio Lenzi

Advisor:

Prof. G. Campana

PhD Director:

Prof. M. Carricato

Co-Advisor:

Prof. I. S. Jawahir

Keywords: Quenching, Distortion, Steel, Oil, Sustainability

Final exam 2019

Acknowledgements

I would like to express my heartfelt gratitude to the numerous people, in a multitude of situations and institutions, who helped me in the many stages of this thesis.

I wish to firstly thank the Ministry of Education, University and Research (MiUR) and the Proterm s.r.l enterprise for all their financial support and cooperation throughout my degree course and project development.

I am also deeply grateful for the opportunity, guidance and instruction offered by the University of Bologna, In particular my professor and mentor Giampaolo Campana who taught me complete commitment to research with a structured-approach and imparted intense curiosity beyond new discoveries. Thanks are warmly extended as well to all the other members of the Centre for Aided and Intelligent Manufacturing (CAIMan) at Bologna University, Mattia Mele for all his friendly cooperation during the work activities, and Barbara Cimatti for her many positive suggestions and involvements in beneficial experiences such as the KES-SDM and GCSM conferences. My excellent colleagues at CAIMan made it a pleasure to work there and something of which to be proud.

Concerning the manuscript phase, I am immensely grateful to Professors I. S. Jawahir and J. Bonvoisin for their considered and precise revisions and comments that guided me in improving the scientific value of this work, and Christopher Marshall for all his advice and editorial assistance in the final completion of this document.

Finally, A special mention must be given to my family, to my dear grandparents and my fiancé Greta. I couldn't have realised this without their patient and loving support.

Contents

Acknowledgements	i
Contents	iii
List of Figures	vii
List of Tables	xiii
Introduction	1
1 Introduction to Sustainable Manufacturing and its Application to Quenching Processes	3
1.1 A Sustainable Approach to Manufacturing	3
1.2 Quenching Deformations	7
1.3 Die-Assisted Oil Quenching process	9
1.4 Introduction to Oily Mediums	13
1.5 Multi-physical quenching modelling	16
1.6 Chapter 1 Summary	19
2 Construction of a Multi-Physical Quenching Model	21
2.1 Introduction	21
2.2 Focus and Specifications of the Quenching Model	21
2.3 Temperature Determination	24
2.4 Implementation of the microstructural evolution	27
2.4.1 Determination of the starting conditions	27
2.4.2 Microstructural development in the heating stage	30
2.4.3 Microstructural development in the cooling stage	34

2.4.4	Nested Conditions between the Heating and the Cooling phases	39
2.5	Evaluation of Quenching Distortions	41
2.5.1	Implemented Material properties	43
2.6	Overview of Modelling Results	43
2.7	Summary of modelling results	47
3	Experimental Investigations	49
3.1	Introduction	49
3.2	Design of the experiment	50
3.3	Metrological inspections	51
3.4	Analysis of the experimental data: An Overview	54
3.5	Volume	56
3.5.1	Determination of Volume Variations	56
3.5.2	OTOQ-Volume variations	58
3.5.3	DAOQ-Volume variations	61
3.5.4	Conclusion concerning volume variations	62
3.6	Inner Diameter	64
3.6.1	OTOQ-Inner diameter variations	65
3.6.2	DAOQ-Inner diameter variations	66
3.6.3	Conclusion regarding inner diameter variations	69
3.7	Outer Diameter	71
3.7.1	OTOQ-Outer diameter variations	71
3.7.2	DAOQ-Outer diameter variations	73
3.7.3	Conclusion regarding outer diameter variations	75
3.8	Thickness	77
3.8.1	OTOQ-Thickness variations	77
3.8.2	DAOQ-Thickness variations	79
3.8.3	Conclusion regarding thickness variations	80
3.9	Shape Tolerance: investigation into the Planarity Tolerance	83
3.10	Comparison between Mineral and Vegetable Quenching Oils	87
3.10.1	Cooling curve analysis	87
3.10.2	Impact comparison	88

3.10.3	Experimental activity	89
3.10.4	Analysis of the experimental data	92
3.11	Summary of Experimental Activities	97
4	Comparison of Model Predictions with Experiments	99
4.1	Introduction	99
4.2	Model setting: definition of the deformations	101
4.3	Influence of HTC's on the Predictions	106
4.3.1	investigation regarding Model1	108
4.3.2	Investigation regarding Model2	115
4.4	Modelling Conclusions	121
	Conclusion	123
	Bibliography	125

List of Figures

1.1	<i>The closed-loop 6R approach for sustainable manufacturing [10]</i>	5
1.2	<i>Volume variations based on several material microstructures [19]</i>	7
1.3	<i>Fish-bone diagram regarding the causes of quenching distortions [20]</i>	8
1.4	<i>Oil circulation inside the quenching tank: (a) eductors located at opposite bottom edges; (b) eductors located under the load [21]</i>	9
1.5	<i>(a) Die Assisted Oil Quenching Machine; (b) typical gear treated on DAOQ machine</i>	10
1.6	<i>In process steps concerning the DAOQ process: (a), (b) placement and centring by means of the expander, (c) the action of the inner and outer upper dies, (d) a complete visualisation of the DAOQ process conditions</i>	11
1.7	<i>Representation of the cooling paths concerning the surface and core of a mechanical part [23]</i>	13
1.8	<i>Qualitative trend of heat transfer coefficient and heat flux across the part throughout the quenching thermal cycle [19]</i>	14
1.9	<i>Example of a cooling curve test [19]</i>	15
1.10	<i>Couplings between the different physical-fields involved in heat treatment simulations [42]</i>	17
2.1	<i>Typical structure of a quenching thermal cycle</i>	22
2.2	<i>Structure of the quenching multi-physical model expressed in terms of temperature, microstructural and deformations couplings</i>	23
2.3	<i>Axisymmetric component utilises for the modelling activity</i>	23
2.4	<i>The temperature time-dependent interface for the OTOQ modelling</i>	25
2.5	<i>The HTC time-dependent interface for the OTOQ modelling</i>	25

2.6	<i>Comparison between real and implemented HTC trends throughout a quenching cooling phase</i>	27
2.7	<i>The Fe-C state diagram utilised for the evaluation of the starting material microstructure</i>	28
2.8	<i>The 100Cr6 starting microstructure for the OTOQ modelling</i>	29
2.9	<i>The 100Cr6 critical temperatures based on the Fe-C diagram</i>	30
2.10	<i>Material implementation according to critical temperature</i>	31
2.11	<i>The HTC and temperature time-dependent interfaces</i>	34
2.12	<i>The cooling path until A_{cm}</i>	35
2.13	<i>The pearlitic and bainitic activation points concerning the diffusive transformations</i>	37
2.14	<i>A quenching thermal cycle addressed to the evaluation of heating and cooling times</i>	39
2.15	<i>Volume variations connected to (a) Cartesian and (b) polar model geometries</i>	42
2.16	<i>OTOQ model to evaluate temperatures, microstructural evolution and deformations</i>	44
2.17	<i>Thermal analysis performed by OTOQ model</i>	45
2.18	<i>Microstructural evolution esteemed by OTOQ model</i>	46
2.19	<i>The radial displacement assessment derived from OTOQ model</i>	46
3.1	<i>The experimental testing geometries</i>	50
3.2	<i>The DAQO process conditions</i>	51
3.3	<i>The manufacturing stage realised for the experimental activities</i>	51
3.4	<i>The CMM machine utilised for the experimental investigations</i>	52
3.5	<i>The sample measurement position utilised during the experiments</i>	53
3.6	<i>The strategy of the inner and outer diameters evaluations during the experimental campaign</i>	53
3.7	<i>The thickness determination: (a) the feeler pin movement; (b) detection points for the measurements</i>	54
3.8	<i>The evaluation of planarity tolerance</i>	55
3.9	<i>The calculated volume variations through the experimental measurements</i>	56

3.10	<i>Volume variations induced by Ph02</i>	58
3.11	<i>The ANOVA main effects concerning (a) materials and (b) geometries of the volume variations induced by Ph02</i>	59
3.12	<i>The ANOVA interaction regarding the volume variations induced by Ph02</i>	60
3.13	<i>Volume variations induced by Ph05</i>	61
3.14	<i>The ANOVA main effects concerning (a) materials and (b) geometries of the volume variations induced by Ph05</i>	62
3.15	<i>The ANOVA interaction regarding the volume variations induced by Ph05</i>	63
3.16	<i>Direct comparison among volume variations induced by Ph02 and Ph05 for the case of 100CrMo7</i>	63
3.17	<i>Direct comparison among volume variations induced by Ph02 and Ph05 for the case of 18NiCrMo5</i>	64
3.18	<i>Direct comparison among volume variations induced by Ph02 and Ph05 for the case of 20MnCr5</i>	64
3.19	<i>Inner diameter variations induced by Ph02</i>	65
3.20	<i>The ANOVA main effects concerning (a) materials and (b) geometries of the inner diameter variations induced by Ph02</i>	66
3.21	<i>The ANOVA interaction regarding the inner diameter variations induced by Ph02</i>	67
3.22	<i>Inner diameter variations induced by Ph05</i>	67
3.23	<i>Inner diameter variations induced by Ph05 compared with Ph04</i>	68
3.24	<i>The ANOVA main effects concerning (a) materials and (b) geometries of the inner diameter variations induced by Ph05</i>	68
3.25	<i>The ANOVA interaction regarding the inner diameter variations induced by Ph05</i>	69
3.26	<i>Inner diameter variations induced by Ph02 and Ph05 for 100CrMo7</i>	70
3.27	<i>Inner diameter variations induced by Ph02 and Ph05 for 18NiCrMo5</i>	70
3.28	<i>Inner diameter variations induced by Ph02 and Ph05 for 20MnCr5</i>	71
3.29	<i>Outer diameter variations induced by Ph02</i>	72
3.30	<i>The ANOVA main effects concerning (a) materials and (b) geometries of the outer diameter variations induced by Ph02</i>	72

3.31	<i>The ANOVA interaction regarding the outer diameter variations induced by Ph02</i>	73
3.32	<i>Outer diameter variations induced by Ph05</i>	74
3.33	<i>The ANOVA main effects concerning (a) materials and (b) geometries of the outer diameter variations induced by Ph05</i>	74
3.34	<i>The ANOVA interaction regarding the outer diameter variations induced by Ph05</i>	75
3.35	<i>Outer diameter variations induced by Ph02 and Ph05 for 100CrMo7</i>	76
3.36	<i>Outer diameter variations induced by Ph02 and Ph05 for 18NiCrMo5</i>	76
3.37	<i>Outer diameter variations induced by Ph02 and Ph05 for 20MnCr5</i>	77
3.38	<i>Thickness variations induced by Ph02</i>	78
3.39	<i>The ANOVA main effects concerning (a) materials and (b) geometries of the thickness variations induced by Ph02</i>	78
3.40	<i>The ANOVA interaction regarding the thickness variations induced by Ph02</i>	79
3.41	<i>Thickness variations induced by Ph05</i>	80
3.42	<i>The ANOVA main effects concerning (a) materials and (b) geometries of the thickness variations induced by Ph05</i>	80
3.43	<i>The ANOVA interaction regarding the thickness variations induced by Ph05</i>	81
3.44	<i>Thickness variations induced by Ph02 and Ph05 for 100CrMo7</i>	81
3.45	<i>Thickness variations induced by Ph02 and Ph05 for 18NiCrMo5</i>	82
3.46	<i>Thickness variations induced by Ph02 and Ph05 for 20MnCr5</i>	82
3.47	<i>Plane 1 - planarity tolerances induced by Ph02 and Ph05 for 100CrMo7</i>	84
3.48	<i>Plane 2 - planarity tolerances induced by Ph02 and Ph05 for 100CrMo7</i>	84
3.49	<i>Plane 1 - planarity tolerances induced by Ph02 and Ph05 for 18NiCrMo5</i>	85
3.50	<i>Plane 2 - planarity tolerances induced by Ph02 and Ph05 for 18NiCrMo5</i>	85
3.51	<i>Plane 1 - planarity tolerances induced by Ph02 and Ph05 for 20MnCr5</i>	86
3.52	<i>Plane 1 - planarity tolerances induced by Ph02 and Ph05 for 20MnCr5</i>	86
3.53	<i>Cooling rate as a function of the oil temperature. Experimental curves of the vegetable (blue curve) and mineral (black curve) quenching medium</i>	88
3.54	<i>Open LCA software model for a soybean vegetable oil</i>	89
3.55	<i>Comparison between mineral and vegetable oils for relevant impacts</i>	90

3.56	(a) Identification of the investigated conical bevel gears; (b) measurement equipment for the evaluation of the planarity tolerances	91
3.57	In-process equipment for the detection of quenching fumes	92
3.58	(a) Martensite microstructure obtained by the usage of mineral and vegetable quenching oils; (b) Experimental evaluation of superficial hardnesses and case depths for both mediums	94
3.59	(a) TOP 5 analysis: Evolution of inner diameters of geometry1 along the process stages; (b) In-line process control: Gaussian distributions of distortions regarding the inner diameters of geometry1	95
4.1	(a) 2D axisymmetric model, (b) microstructural evolution, (c) temperature contour plot, (d) evolution of radial displacements, (e) temperature evolution	100
4.2	The Hardness estimation taking into account the mixture rule	101
4.3	Definition of the proportions among the deformations for model 1	101
4.4	The Overlapping between modelling and experimental outcomes for model 1	103
4.5	Simulated null deformations of inner diameter taking into account model1	104
4.6	The Overlapping between modelling and experimental outcomes for model 2	105
4.7	Simulated null deformations of inner diameter taking into account model2	105
4.8	Matching between HCTs and model boundaries	106
4.9	Evaluation points for each simulation	107
4.10	Temperature analysis concerning the first simulation of Model1: (a) complete thermal cycle; (b) 2D temperature contour plot; (c) changing from heating to cooling phases; (d) cooling path of the evaluation points .	108
4.11	Microstructural evolution concerning Model1: (a) internal, (b) external, (c) middle microstructural evolutions along the cooling phase, (d) detection points	109
4.12	Evolution of radial displacements for internal, external and middle sections	110
4.13	Evolution of axial displacements for internal, external and middle sections	110
4.14	Influence of HTC on the martensitic percentage taking into account the inner section	111

4.15	<i>Influence of HTC's on the martensitic percentage taking into account the middle section</i>	111
4.16	<i>Influence of HTC's on the martensitic percentage taking into account the middle section</i>	112
4.17	<i>Influence of HTC's on the radial displacement in correspondence of the inner section</i>	113
4.18	<i>Influence of HTC's on the radial displacement in correspondence of the middle section</i>	113
4.19	<i>Influence of HTC's on the radial displacement in correspondence of the outer section</i>	114
4.20	<i>Temperature analysis concerning the seventh simulation of Model2: (a) complete thermal cycle; (b) 2D temperature contour plot; (c) changing from heating to cooling phases; (d) cooling path of the evaluation points</i>	115
4.21	<i>Microstructural evolution concerning Model2: (a) internal, (b) external, (c) middle microstructural evolutions along the cooling phase, (d) detection points</i>	116
4.22	<i>Evolution of radial displacements for internal, external and middle sections</i>	117
4.23	<i>Evolution of axial displacements for internal, external and middle sections</i>	117
4.24	<i>influence of HTC's on the martensitic percentage taking into account the inner section</i>	118
4.25	<i>influence of HTC's on the martensitic percentage taking into account the outer section</i>	118
4.26	<i>Influence of HTC's on the radial displacement in correspondence of the inner section</i>	119
4.27	<i>Influence of HTC's on the radial displacement in correspondence of the middle section</i>	120
4.28	<i>Influence of HTC's on the radial displacement in correspondence of the middle section</i>	120

List of Tables

1.1	<i>Manufacturing categories based on the three pillars of sustainability [8]</i>	4
1.2	<i>Comparison between DAOQ and OTOQ in terms of sustainable pillars[22]</i>	12
1.3	<i>Microstructural deformations related to austenitic, pearlitic, bainitic and martensitic transformations [18]</i>	18
1.4	<i>Material properties implemented in the OTOQ quenching model [38]</i>	18
3.1	<i>In-process equipment for the detection of quenching fumes</i>	92
4.1	<i>Realised simulations for both models through Taguchi method</i>	107

Introduction

The work in this thesis centres around a specific phase in the manufacturing of metal components, the quenching process. This integral and mass-performed task in industry is analysed and examined in the context of sustainability in manufacturing using the recently developed framework known as the 6R theory, which individuates the six pillars of Reduce; Reuse; Recover; Redesign; Re-manufacture; Recycle. The research and experimentation discussed concentrate on a virtualisation of the quenching process to investigate different methods and materials and the possible implications their adoption could have for industry. Findings are framed in the construct of 6R theory, in particular the Reduce factor. The research projects presented were conducted at length, in-depth and often manually carried out, focussing on the dimensional and shape variations induced by quenching processes and aiming to precisely define machining allowances and reduce the amount of raw-material utilised to achieve final design requirements. A multi-physical quenching model was realised for the prediction of distortions occurring in a standard manufacturing cycle. The model, aided by physical experimental activities, focused on the evaluation of deformations and took into account varying part geometries and types of steel. A comparison between mineral and vegetable quenching oily mediums was also conducted. The software application employed was tailor-made, using a layered physics approach to predict the range of behaviour of the processed part. Results show that the calculated deformations throughout the virtual quenching cycle accurately reflect the trends and magnitudes of the experimental distortions. A large amount of data was collected allowing for accurate tuning of the mathematical model to fully replicate the experimental findings. Both hardening and carburising materials were experimentally investigated to highlight differences in terms of their behaviour and, specifically, their dimensional variations. The dissimilarities that originated not only

from their chemical compositions but also the technological phases they underwent were evidenced. A comparison between traditional and die assisted oil quenching processes was also carried out, assessing the extent of dimensional and shape variations induced by the mould-aided process. Results were positive and indicated that the combined effect of modelling and experimentation can accurately define machining allowances, leading to a reduction or even an avoidance of post-quenching machining operations such as grinding. The vegetable quenching medium also performed better in comparison with petroleum-based oil: lowering environmental impact without compromising mechanical and dimensional results.

All research and activity was conceptualised and developed closely linked to the 6R concepts, focussing on the Reduce element and highlighting the technological restrictions of the traditional quenching process and the need to move towards replicable and reliable hardening stages such as the die-assisted oil technique. This research project aims at the virtualisation of quenching processes in order to precisely design mechanical parts, concentrating particularly on the accurate defining of dimensional variations. These emulations can assist in the accurate planning and reducing of machining allowances, decreasing energy consumption as well as the amount of raw materials used. This possible course of evolution, both in process and virtualization, has the potential to effectively improve the sustainability of industry – and hence the planet’s sustainability - due to the multiplicity and generic quality of component manufacture around the world.

In chapter one, an industrial comparison in terms of sustainable pillars is presented and the final section investigates liquid mediums and multi-physical modelling. This is expanded upon in the second chapter and a complete overview is given of the thermal, microstructural and stress-strain physical fields required in order to replicate quenching outcomes. The capabilities of the model are also described in detail. The third chapter investigates the experiments conducted, considering traditional and die assisted oil-quenching processes through analyses of dimensional variations and shape tolerance changes. In addition, vegetable and mineral quenching oils are compared in terms of mechanical, microstructural, dimensional and environmental performance. The fourth and final chapter assesses the mathematical model and the experimental findings in order to evaluate the accuracy of the quenching simulations and also introduces an outline of the final tuning phase.

Chapter 1

Introduction to Sustainable Manufacturing and its Application to Quenching Processes

1.1 A Sustainable Approach to Manufacturing

The world's continuously growing population is being faced with ever-increasing needs in order to ensure a high standard of life in developed countries as well as the ongoing advancement of underdeveloped areas of the world. Thus, these rising demands can only be supported by a redefinition of the development pattern in which the whole production phase is re-modelled to better employ natural resources. The ecological balance of our planet was in actual fact surpassed back in 1985 and we would now need two Earths at our disposal in order to contain the actual depletion rate of renewable and non-renewable natural resources [1]. In other words, humankind is rapidly consuming more than the planet has the capability to restore.

35% of total energy consumption as well as over 20% of carbon dioxide emissions (CO₂) derives from manufacturing [2]. Mass production was substituted by Lean manufacturing characterised by a waste minimisation which early on became Green focused on the usage of natural resources and also with particular attention to pollution and emissions and finally, taking the best aspects of Lean and Green into account, evolved into Sustainable manufacturing (SM).

SM puts in place lean and green concepts in order to achieve the Triple Bottom Line (TBL), composed of the following three pillars: Environment; Economy; Society [3] and can be defined as, *“the creation of manufactured products that use processes that minimize negative environmental impacts, conserve energy and natural resources, are safe for employees, communities and consumers and are economically sound”* [5].

“Sustainable manufacturing minimizes adverse environmental impacts, improves energy and resource efficiency, generates a minimum of waste, and provides improved operational safety and personal health while maintaining and/or improving the product and process quality with overall life-cycle cost benefit” [7].

Tab. 1.1 makes a clear distinction between different types of manufacturing paradigms in terms of TBL.

Table 1.1: *Manufacturing categories based on the three pillars of sustainability* [8]

Manufacturing categories	Sustainability aspect covered		
	Environmental	Social	Economic
Green	X	X	
Lean	X		X
Mass		X	X
Sustainable	X	X	X

The 3R concepts (reduce, reuse and recycle) utilised in green technologies, have been expanded to include three other steps in order to theoretically obtain a closed loop circulation where raw material resources can be used more than once [9]. SM has been recently defined through this “6R” concept that leads directly to a circular economy of closed loop resources in which the product and processes are designed to ensure more than a single life-cycle [9]. 6R takes into account the 3Rs deriving from the Green approach and adds recover, redesign and re-manufacture leading to a comprehensive definition of product multiple life-cycles [5]. The 6R approach includes: reduce, reuse, recover, redesign, re-manufacture, recycle.

- *Reduce* is an essential requirement in order to lessen resource involvement across all life-cycle stages: pre-manufacturing, manufacturing and usage, [5].
- *Reuse* relates to making use of materials more than once, not just at the end of the first life-cycle, so decreasing the employment of raw-resources [5].

- *Recycle* turns waste derived from the first life cycle into new materials or products [5].
- *Recover* collates operations like sorting, disassembling and cleaning at the end of the first usage stage in order to bring back useful parts and materials into a new life-cycle [9].
- *Redesign* means to implement the Design for Environment concepts (DfE) in order to ease and facilitate future post-use application [9].
- *Re-manufacture* restores product to as new a state as possible, utilizing already-used parts in order to replace the original functionality [9].

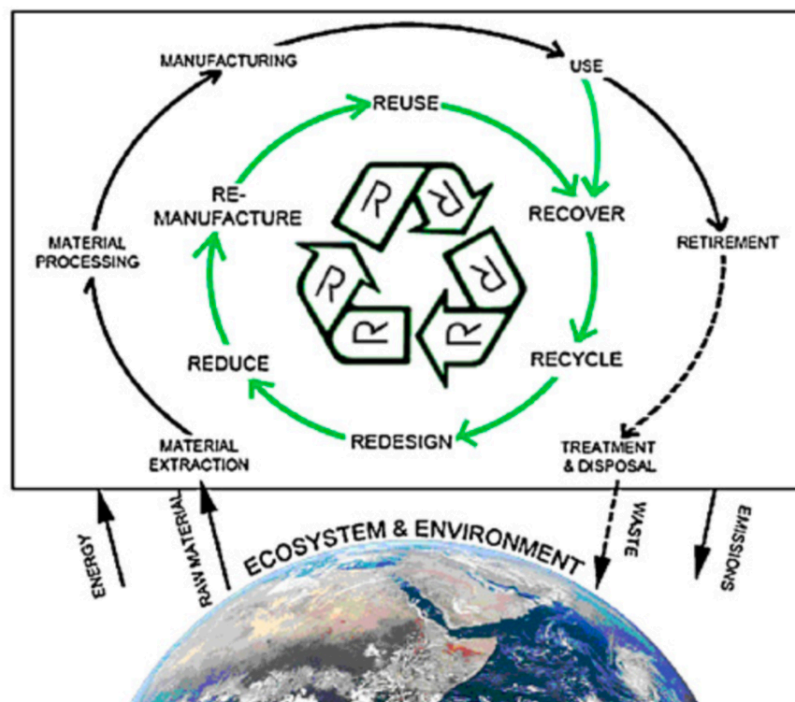


Figure 1.1: *The closed-loop 6R approach for sustainable manufacturing [10]*

This paradigm stresses the need to re-define present products and services to more economically achieve the same quality while employing a smaller amount of raw, and preferably renewable, materials [11]. The societal aspects regard the ensuring of human rights and the enhancing of living standards; whereas environmental attributes address the need to make use of materials more than once [12]. This discussion leads to the

understanding that the sustainable pillars are unequivocally connected and the achievement of one promotes the obtainment of the others.

Technology developments and the wide spreading of education have been identified as Key Enabling Factors (KEF) in the advancement of SM [13]. Sustainability can be achieved by enhancing knowledge through research, education and innovation, a charge to be given to companies, researchers and students in order to promote SM [14]. New development technologies can address the reduction of the assessed main impacts, targeting the realization of eco-factories in which near-to-zero emissions can be achieved [13], while research focuses on the development of innovative strategies regarding the implementation of equipment for energy reduction, modelling simulation systems for a knowledge-based approach to the design and production phases [3].

A structured approach to these steps could eventually result in zero defects as well as zero waste, providing notable individual savings on cost and more importantly, considering the enormous amount of daily manufacture around the world, substantially reduce the environmental impact caused by industry [15]. To achieve this aim, the main objective of production engineering must be to find solutions to reduce the environmental impact of manufacturing processes and to enhance working conditions without affecting the quality of the final product. Particular attention should be paid to those steps of production that consume high amounts of energy and produce polluting emissions; an example is the heat treatment of steel, which is a fundamental phase in the production cycle of many mechanical parts. Along the technological chain of component production, Quenching is an essential operational step in order to obtain mechanical performances by modifying the microstructure of materials. To satisfy sustainable manufacturing issues in heat treatments requires optimisation of the thermal cycles, adoption of adequate equipment and the selection of the most suitable cooling fluids to reduce distortions [5]. The design of quenched parts has to accurately calculate machining allowances in order to maintain components within dimensional tolerances following machining operations (typically grinding). Processes that increase the time and cost of the production cycle. The adoption of a more controllable and replicable quenching treatment is a way to considerably improve process sustainability as it not only reduces machining allowances but also eliminates the need for subsequent post-quenching operations.

1.2 Quenching Deformations

The quenching process of steel is a fundamental heat treatment operation that produces the best mechanical properties as the treated part undergoes a martensitic transformation during the cooling phase. The process is able to increase wear characteristics in order to withstand the higher contact stresses typical in gears or bearing rings [16]. Quenching improves material properties but it induces unavoidable changes in the shape and dimensions of the treated parts. Distortions can be classified as positive or negative variations in dimensions as well as modifications of shape tolerances such as planarity or out-of-round errors. These distortions mainly depend on thermal gradients encountered throughout the thermal cycle as well as volume variations associated with material phase transformations [19]. Deformations are caused by crystal lattice adjustments from initial to martensite microstructures, leading to volume enhancements [17], [18].

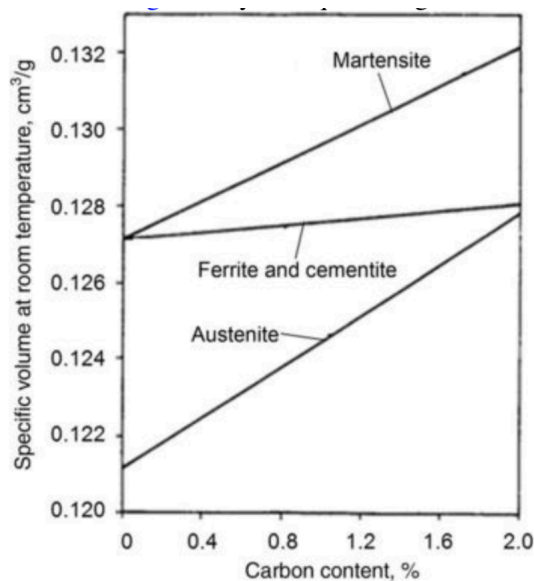


Figure 1.2: *Volume variations based on several material microstructures [19]*

Fig. 1.2 portrays the volume variations, taking into account each microstructural phase for 20MnCr5 at room temperature [19]. The martensite induces the highest volume variations, which, depending on the carbon percentage, results in overall dimensional increases. Deformations are related not only to each step of the production chain - from steelworks to final manufacturing operations - but also to the design phase [20]. There are many factors that influence the occurrence and amount of deformation such as part

geometry, material quality, the technological and thermal history of the component, residual stresses and quenching process conditions. This is illustrated in Fig. 1.3.

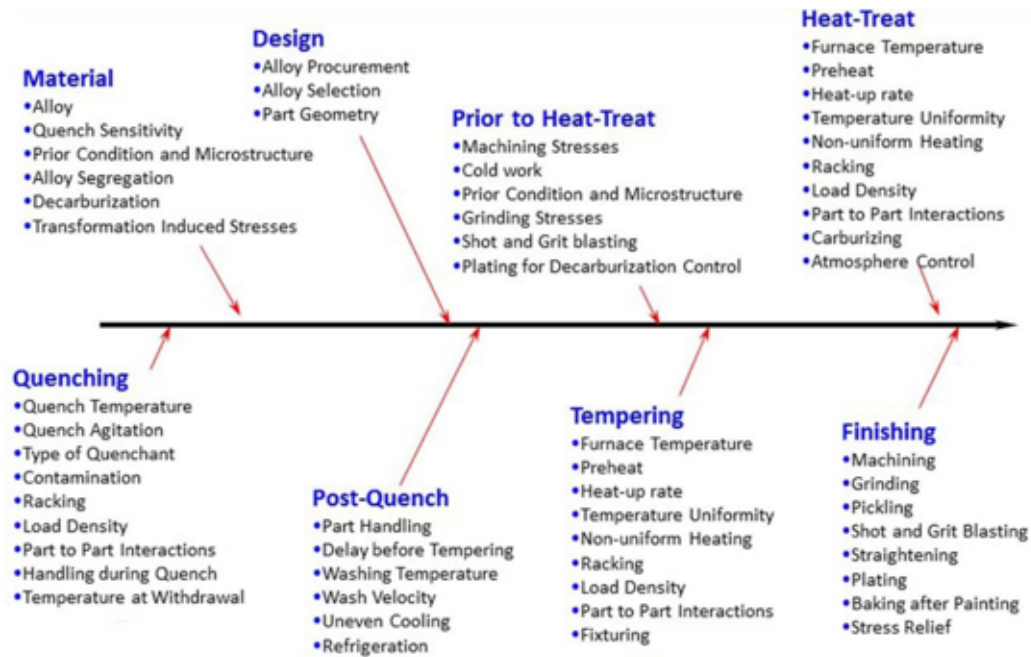


Figure 1.3: Fish-bone diagram regarding the causes of quenching distortions [20]

The quenching thermal cycle is characterized by steady heating and severe cooling respectively performed in a furnace and in a tank full of liquid medium. This process is named Open Tank Oil Quenching (OTOQ). It involves a batch of products in which mechanical parts are concurrently treated in unequal cooling conditions due to inhomogeneous oil circulation inside the container and resulting in non-identical manufacturing outcomes across the batch; components can either be well processed or fail to fulfil design requirements [21]. This is illustrated in Fig. 1.4.

In addition, shortcomings in the design phase could result in higher distortion magnitudes due to asymmetrical heat extractions caused by unbalanced shape, holes, groove and key-ways. An appropriate design has to be put in place in order to reduce quenching distortions and realise the treated parts in as precise a shape as possible after quenching processes.

Deformations directly imply the addition of more raw material through allowances in order to control the side effects of the quenching process. The addition of this material compensates, in the magnitude of a tenth of a millimetre, in order to obtain the desired final shape of the part by means of post-quenching machining operations. High-levels of

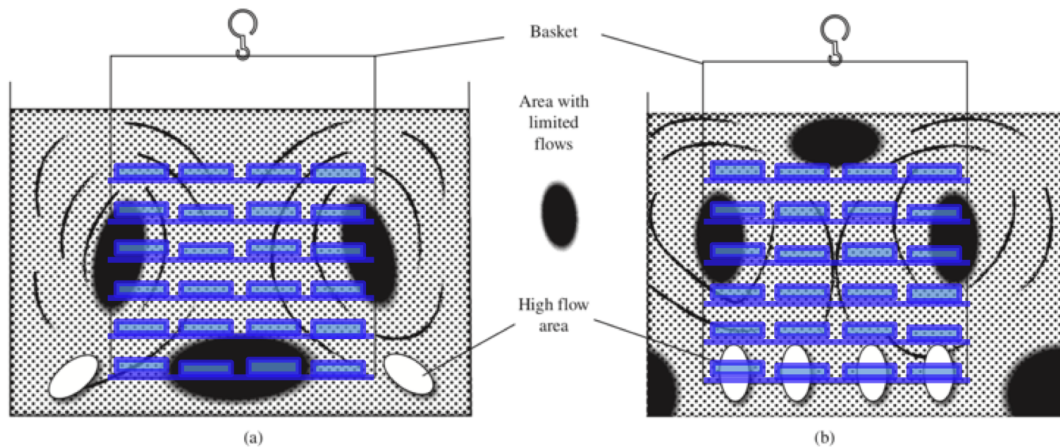


Figure 1.4: Oil circulation inside the quenching tank: (a) eductors located at opposite bottom edges; (b) eductors located under the load [21]

distortions implicate even higher-amount of allowances and thus, the material reductions cannot fulfil the 6R aims [5]. Reducing distortions lowers the consumption of raw material and also shortens the technological cycle by giving the possibility to decrease or even avoid standard post-quenching operations such as grinding or cold-straightening. The whole discussion highlights the necessity to advance the industry state of the art and create replicable and reliable quenching processes of steel that target distortion reduction. The following section looks at an alternative to OTOQ: the process of Die-Assisted Oil Quenching (DAOQ).

1.3 Die-Assisted Oil Quenching process

OTOQ is at present the most common quenching process and can achieve the highest material performances by means of martensitic transformation. However, it induces uncontrolled distortions on the treated parts due to thermal gradients and microstructural transformations. These geometric variations must be corrected by means of cold straightening or grinding processes to maintain the required dimensions and shape tolerances, processes which add cost and time to the production phase [19].

Aiming at reducing these wasteful distortions, DAOQ has been in development since the beginning of 20th century. It is a highly customizable quenching technique in which the above-mentioned post-quenching operations can be reduced or even avoided with a minimisation of machining allowances [22]. DAOQ is defined as: "Heating a part to the

austenitic condition and then immersing the same into a liquid to achieve metallurgical transformation, while at the same time forcing the part to hold size and shape” [23]. DAOQ is suitable for axisymmetric components such as bearing rings or gears, which have a high sensitivity to quenching distortions. These components are typically characterised by a high transversal section in comparison with their thickness [24]. The process is performed by a hydraulic press and a mould working on one single piece at the time. The pressure exerted by the machine through the mould on the treated parts

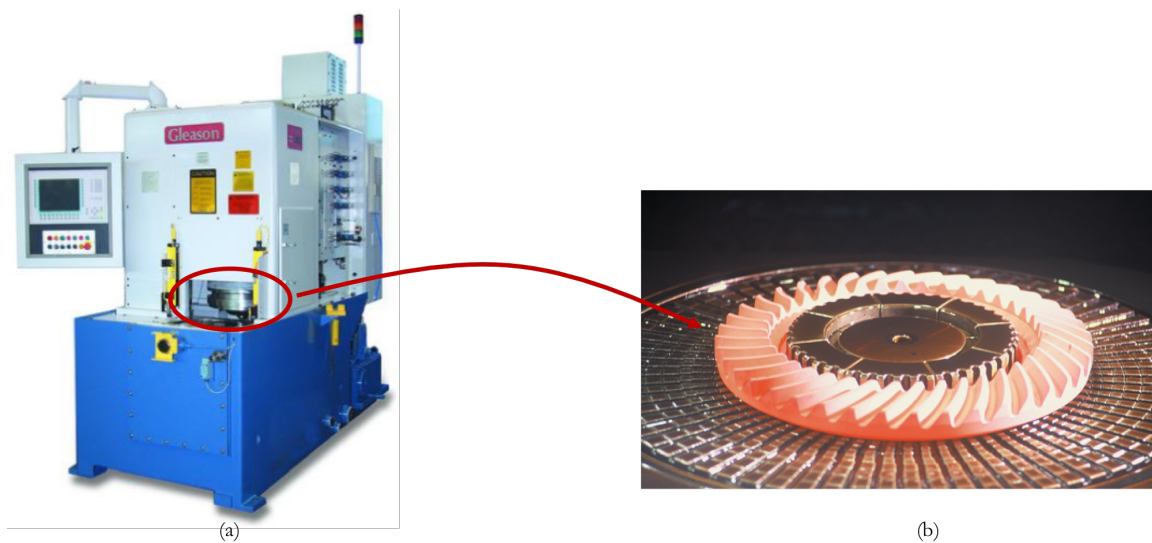


Figure 1.5: (a) Die Assisted Oil Quenching Machine; (b) typical gear treated on DAOQ machine

constrains the in-process part. At the same time, the component is completely surrounded by the quenching medium, cooling it down and ensuring the final martensite microstructure, Fig. 1.5. The mould has been constituted by:

- a centre expander cone that controls the inner hole and locates components during the initial stages of the quenching cycle, Fig. 1.6 (a), (b);
- an inner upper die that reduces the flatness of the part, Fig. 1.6 (c);
- an outer upper die that controls the external diameter of the components and can act on the planarity with a different pressure of inner die, Fig. 1.6 (d).

Three hydraulic circuits independently control the three sections of the mould and each part can be set with a different pressure. In addition, other process parameters such as flow rates and the temperatures of the quenchant can be minutely tuned to target the product needs, resulting in a customisable quenching process.

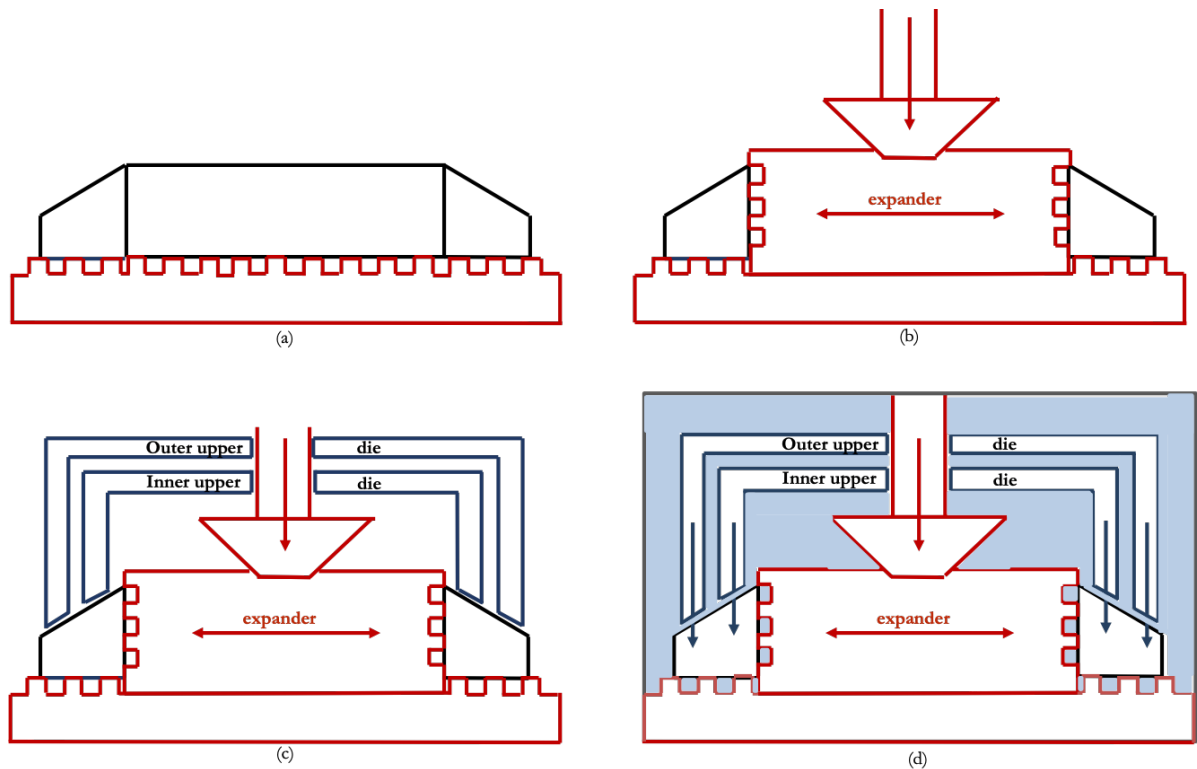


Figure 1.6: *In process steps concerning the DAOQ process: (a), (b) placement and centring by means of the expander, (c) the action of the inner and outer upper dies, (d) a complete visualisation of the DAOQ process conditions*

The most efficient cooling path is determined by the correlation between the decreasing of temperature, to limit thermal gradients inside the part, and the martensitic transformation. This relation results in a trade-off between the rate of cooling and the initial point of martensitic transformation in order to select the most appropriate liquid medium. The highest cooling rate should be set between A_{c3} and M_s due to the absence of material transformations. Following this, a gentle cooling rate should be ensured to decrease the thermal gradients across the section of the part without compromising the material transformation from M_s to M_f . After the martensite transformation has been achieved, a precise cooling rate is no longer required.

The DAOQ process, while having many advantages over OTOQ, is also not without its own negative side effects such as increased complexity in management of the process control and the need for the mould design to be extremely precise. Table 1.2 compares OTOQ with DAOQ, displaying the differences among them in terms of sustainable pillars. A conical bevel gear was processed and the positives and negatives analysed in

an industrial case study [22].

Table 1.2: Comparison between DAOQ and OTOQ in terms of sustainable pillars[22]

		Open Tank Oil Quenching (OTOQ)	Die Assisted Oil Quenching (DAOQ)
Manufacturing issues	Technological cycle of a conical crown	<ul style="list-style-type: none"> – Machining; – Carburizing; – OTOQ; – Relieving tempering; – Grinding operation; – Run-in stage 	<ul style="list-style-type: none"> – Machining; – Carburizing; – DAOQ; – Relieving tempering; – Grinding operation; – Run-in stage <p>One more cooling and heating. The DAOQ is indirect quenching.</p>
Sustainable pillars	Economic	<ul style="list-style-type: none"> – Cost of the OTOQ furnace: 50 euro/h; – OTOQ cost: 5 euro/pz; – Grinding operation; – Run-in stage: 20 min; – Machining allowance: 0,2–0,4 mm; 	<ul style="list-style-type: none"> – Cost of the DAOQ equipment: 110 euro/h; – DAOQ cost: 6,5 euro/pz; – No grinding operation; – Run-in stage: 10 min; – Machining allowance: 0,08–0,15 mm;
	Environmental	<ul style="list-style-type: none"> – Machining allowance: 0,2–0,4 mm; – Grinding is unavoidable; – High raw material consumption. 	<ul style="list-style-type: none"> – Machining allowance: 0,08–0,15 mm; – No grinding process; – Low raw material consumption.
	Social	<ul style="list-style-type: none"> – The contact area between crown and pinion is not ideal. It means decrease of reliability and increase of early failure. – Low-level manpower; – High manual work content. 	<ul style="list-style-type: none"> – The best contact between crown and pinion is obtained. – Skilled and specialised workers; – Low manual work content (due to automation).

Results show that DAOQ lengthens the manufacturing cycle due to the addition of one more heating and cooling phases, however, it considerably reduces grinding operations through the minimisation of machining allowances that require hundredths of millimetres tolerance and so directly ensures final assembly operation. In addition, it enhances the quality of the part, ensuring a better load transmission between gear and pinion. By lowering machining allowances DAOQ significantly reduces both time spent

on grinding operations as well as raw materials, Table 1.2. DAOQ requires a higher initial investment than the traditional hardening process due to the press, the die and the automation system employed to improve working conditions. This hardening process involves more skilled workers throughout every step: from the die design to the tuning of the increased number of process parameters.

1.4 Introduction to Oily Mediums

Nowadays, sustainability issues should embrace all manufacturing aspects, from materials and equipment to processes in order to realise the 6R configuration [5]. Industrial fluids are an important field where SM must be introduced to noticeably mitigate air and water pollutions derived from petroleum-based mediums [13]. Near-dry or cryogenic machining phases have been recently developed as gear manufacturing processes, lowering the adoption of lubricants [5], [26]. For quenching processes, the

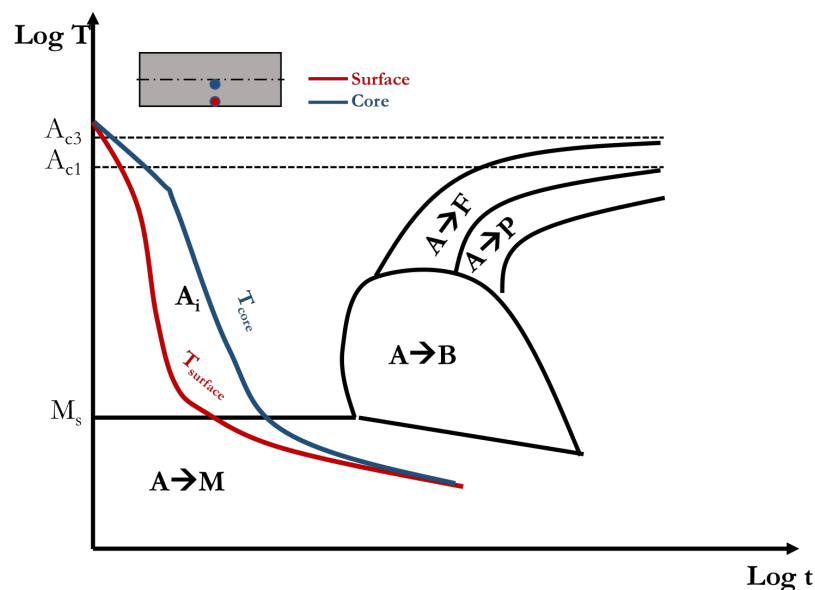


Figure 1.7: Representation of the cooling paths concerning the surface and core of a mechanical part [23]

liquid mediums enable the martensite microstructure during the cooling phase, giving the highest mechanical performances but at the same time creating unavoidable dimensional and shape changes [27].

With the aim to minimise distortions, the most efficient process route is to set the slowest

cooling rate possible in order to maintain a uniform temperature across the part throughout the quenching process without compromising the martensitic transformation. Quick heat extraction and limited thermal gradients are fundamental aspects to be fulfilled to obtain a homogeneous martensite transformation and thus, a reduced level of distortions [19], [23]. Dissimilar cooling paths cannot instantly enable martensitic transformations along the cross section of the part and amplify the final amount of deformations, Fig. 1.7. The cooling conditions strongly depend on the adopted quenchant. Quenching processes can be executed by means of a wide assortment of cooling agents. The choice is determined by a range of factors such as processed materials, part geometries and design requirements. Quenching media traditionally derive from petroleum industries and the base-stocks are standardly composed of either naphthalene or paraffin treated with additives to obtain appropriate performances. The quenching oil should minimise the vapour blanket phase (the first part of the cooling stage) by restricting heat extraction with the vapour film that covers the whole part. When the film collapses, the boiling stage begins and leads to the fastest cooling section, which continues until the oil boiling temperature is reached.

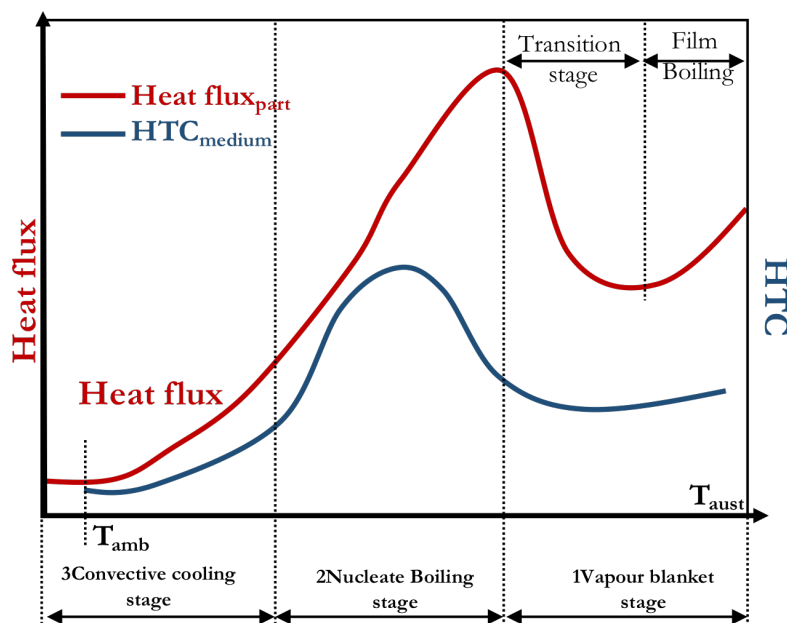


Figure 1.8: *Qualitative trend of heat transfer coefficient and heat flux across the part throughout the quenching thermal cycle [19]*

This phenomenon dramatically reduces the heat transfer coefficient (HTC) at higher

temperatures (Fig. 1.8) and could result at the end of the cooling in untreated areas or soft spots, causing possible early failures [16]. The negative effects of this stage can be mitigated by enhancing the oily agitation to collapse the film while boiling, as well as manipulating the physical properties of the medium such as its viscosity and wettability [21]. A trade-off has to be identified to match contrasting process requirements and obtain a performable quenchant.

Fig. 1.9 illustrates a generic cooling curve derived from a cooling test that evaluates the capability of the medium to cool down a testing sample [33]. It portrays the main steps encountered by the quenchant (blue line), estimating the in-process characteristics. Initially, the vapour blanket stage occurs at the beginning of the temperature decrease. The first inflexion corresponds to the breaking of the film boiling leading to the increase of the cooling rate until the achievement of the highest value (2-nucleate boiling stage). The cooling rate then decreases and the third inflexion marks the beginning of the convective stage. A sustainable approach to manufacturing has to include not only technical aspects but also the optimisation of the production phase to improve the life cycle of the product. Towards this aim, innovative quenching mediums have been developed using vegetable oils. The use of a quenchant derived from organic renewable sources can greatly reduce the environmental impact of the process [28], [29], [30].

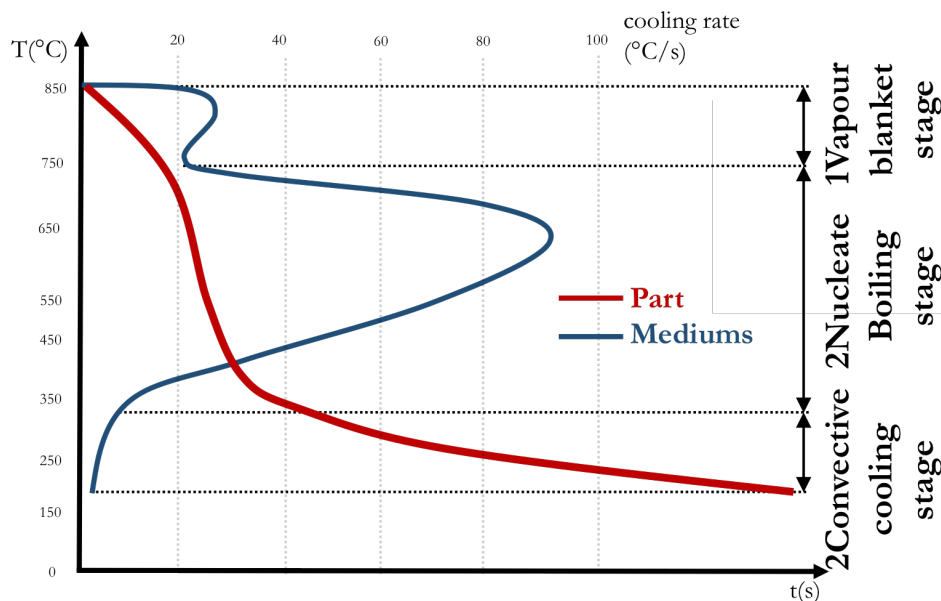


Figure 1.9: Example of a cooling curve test [19]

1.5 Multi-physical quenching modelling

A successful implementation of digital manufacturing is a key factor of modern production systems [35]. Product design and process modelling are strictly linked and process virtualisation plays a crucial role in the obtainment of acceptable standards. Computer Aided Engineering (CAE) platforms are extremely powerful tools to predict the behaviour of industrial processes [36] and Finite Element Methods (FEMs) specifically permit the feasible modelling of chemical-physical phenomena.

The quenching simulation is a necessary step to forecast deformations throughout the technological chain of mechanical components during the design phase in order to save machining allowances and produce parts with a reduced amount of raw material. The simulation can be achieved with the implementation of thermal, mechanical and material science, applying physical, chemical and metallurgical laws to virtually reproduce the entire hardening process. The OTOQ process deeply modifies physical and mechanical properties of finished parts throughout the technological cycle due to the martensitic transformation [37]; so a large number of multi-physical effects have to be taken into account to accurately model quenching processes, a virtualisation that requires powerful computation. FEMs have been successfully applied to generate models that include thermal evolution, material phase transformations, distortions and residual stresses estimations [38], [39], [40], [41]. Building a new FEM model means employing several partial differential equations that describe the quenching process combined with an experimental activity addressed to validate the mathematical model through the matching of tangible and intangible (predicted) distortions.

Fig. 1.10 shows the equations and interconnections involved to describe a quenching cycle. The combining of all the results can accurately estimate the hardening outcomes. The effect of pressure is fundamental when modelling DAOQ as it is the distinguishable parameter that changes the virtual manufacturing conditions from OTOQ to DAOQ. A multi-physics approach of virtualization of the quenching process can be realized by a layering of the physics involved in the process and in the present version of the model the effect of the upper part of the mould was not included. Currently available commercial software that provides heat treatment simulations is not able to take into consideration the entire range of effect parameters, particularly the complex issue of the

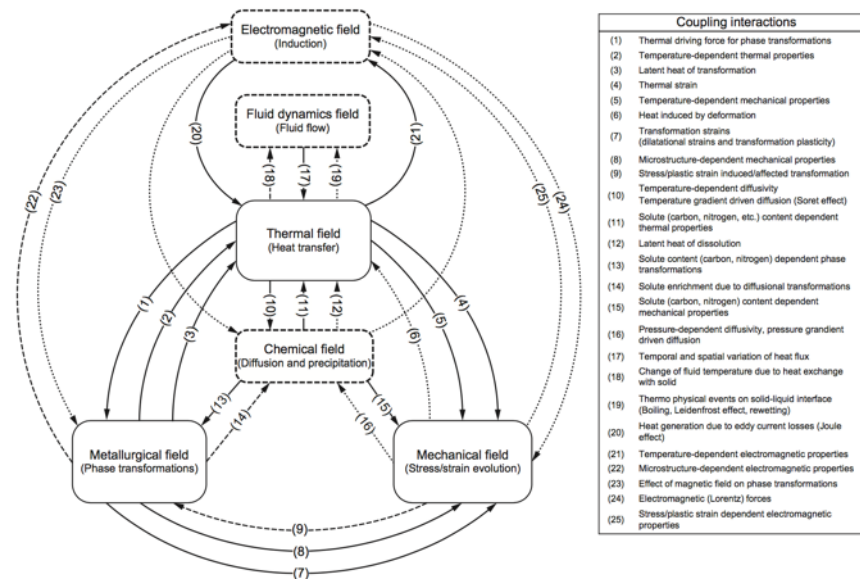


Figure 1.10: *Couplings between the different physical-fields involved in heat treatment simulations* [42]

pressure that is exerted by the die on the treated component. Experimentation has shown DAOQ to be an advanced heat treatment process providing a range of benefits. The hot part is located on the expander and during the process the medium constantly wets the component and equipment. An oily closed-loop circulation is further ensured, accomplishing a steady temperature of the mould and equipment throughout the quenching process. The heat exchange was formulated through the convection conditions (see eq. 2.2 in Chap. 2) and constant HTCs were assessed between the following interfaces piece-mould and piece-oil. Dissimilar materials were employed for the mould and part. Microstructural transformation and thermal gradients were coupled to simulate the quenching deformations, and a model discretization was realized from minute QL1 elements to well-approximated deformations. A high-carbon alloyed steel component (100Cr6) was analysed. The material properties were based on mixture rules linked to temperature evolution and material phase changes [38], [43], [44], [45]. These principal material properties are illustrated in Tab. 1.4.

Table 1.3: Microstructural deformations related to austenitic, pearlitic, bainitic and martensitic transformations [18]

Reactions	Volume Change %	Dimensional Change%
Spheroidite → austenite	-4.64 + 2.21 (% C)	0-0.155 + 0.0074 (% C)
Austenite → martensite	4.64 - 0.53 (% C)	0.0155 - 0.00118 (% C)
Spheroidite → martensite	1.68 (% C)	0.0056 (% C)
Austenite → lower bainite ^(a)	4.64 - 1.43 (% C)	0.0156 - 0.0048 (% C)
Spheroidite → lower bainite ^(a)	0.78 (% C)	0.0026 (% C)
Austenite → aggregate of ferrite and cementite ^(b)	4.64 - 2.21 (% C)	0.0155 - 0.0074 (% C)
Spheroidite → aggregate of ferrite and cementite ^(b)	0	0

(a) Lower bainite is assumed to be a mixture of ferrite and epsilon carbide.

(b) Upper bainite and pearlite are assumed to be mixtures of ferrite and cementite.

Table 1.4: Material properties implemented in the OTOQ quenching model [38]

	Phases	0°C	200°C	400°C	600°C	800°C	1000°C
Elasticity Modulus [GPa]	A,P,M	212	202	186	166	141	112
Poisson's Ratio [-]	A,P,M	0.283	0.291	0.299	0.307	0.315	0.323
Yield Strength [MPa]	A	300	270	240	210	180	150
	P	479	472	400	277	118	-
	M	1116	914	712	510	-	-
Hardening Modulus [GPa]	A	12.0	10.4	8.8	7.2	5.6	4.0
	P	21.0	26.0	22.0	19.0	11.0	-
	M	63.0	40.0	17.0	-	-	-
Density [kg/m ³]	A	7980	7900	7820	7720	7620	7530
	P,M	7820	7740	7770	7620	7530	7460
Heat Conductivity [W/m/K]	A	14.5	17.2	19.9	22.6	25.3	28.0
	P,M	40.0	39.0	35.5	29.0	20.0	8.5
Heat Capacity [J/kg/K]	A	450	510	570	600	630	650
	P,M	410	550	620	790	1160	1850

A: austenite, P: pearlite, M: martensite

1.6 Chapter 1 Summary

- The 6R theory has been discussed and the study of this thesis placed in its context with focus on the Reduce factor, regarding both reductions in manufacturing time and cost as well as in the use of raw materials. Throughout the technological chain of steel mechanical parts, quenching operations have to be finely tuned to minimize the level of distortions. This will allow a saving on machining allowances and reduce or eliminate post-quenching machining operations.
- Distortions mainly depend on thermal gradients developed through the thermal cycle and volume variations connected to the changing of material microstructures. The current standard process of OTOQ performs the hardening through unequal cooling conditions that require high machining allowances in order to compensate for distortions. DAOQ is a more replicable quenching process due to both the press and mould. It is particularly suitable for mechanical parts characterised by a high-value content in which post-quenching operations, such as grinding, are demanding tasks, the absence of which would truly simplify the manufacturing cycle. The liquid medium utilized has to ensure a reduced level of thermal gradients without compromising the martensitic transformation. The most commonly used quenchants are petroleum based but liquid mediums that are vegetable based have and are being developed, providing a more sustainable alternative.
- In parallel to the ongoing progress of materials sourcing and production, is the advancing field of virtualization. The accurate emulating of quenching processes can improve and streamline the design phase. The modelling is complex and a multi-physical approach is required to virtualise OTOQ and DAOQ. The main difference between the two processes is in the pressure effect exerted on the treated parts and this dissimilarity must be calculated for by modifications of the HTC's. The modelling activities discussed herein were coupled with physical experimentation in order to describe the modality of deformations of mechanical parts and accurately compare OTOQ with DAOQ.

Chapter 2

Construction of a Multi-Physical Quenching Model

2.1 Introduction

This chapter investigates the modelling of the quenching process by means of a multi-physical approach using open-handed FEM software. This kind of open customisable software was employed for the modelling to facilitate the precise definition and tailoring of equations and parameters, presenting a unique software environment which avoids cascade connections amongst programs.

Firstly, OTOQ was completely modelled. The temperatures as well as microstructural and deformation behaviours were introduced evaluating the main physical fields that affect steel quenching processes. The modelling activity was run in parallel to an experimental activity (presented in Chap. 3) in order to correctly design the mechanical parts, aiming at a precise prediction of quenching distortions and machining allowances. This chapter focuses on the estimation of quenching distortions caused by the OTOQ process, utilizing a FEM-based multi-physical approach.

2.2 Focus and Specifications of the Quenching Model

The model evaluates the main OTOQ outcomes, taking into account temperature evolution, metallurgical and stress-strain developments (at this stage, the pressure effect exerted by the press through the mould on the treated part in the DAOQ process is not

yet considered).

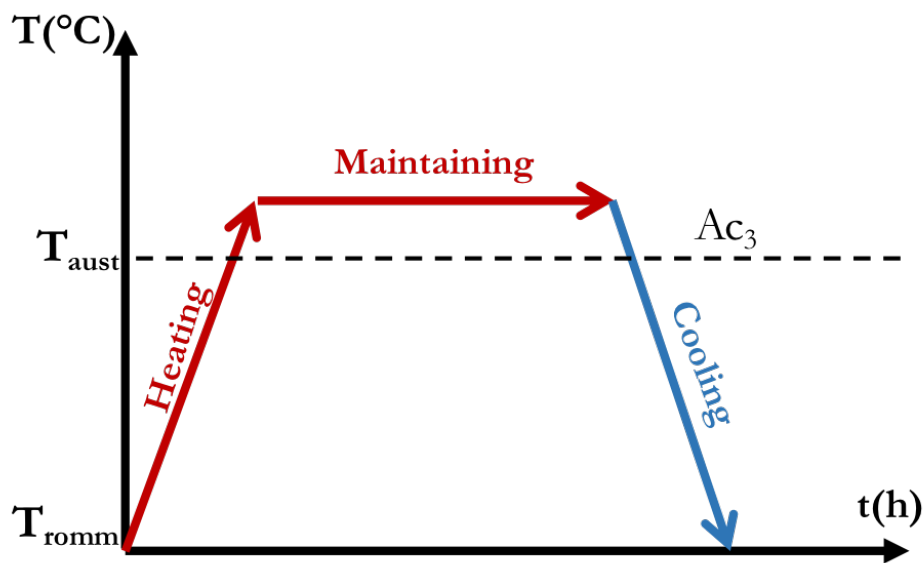


Figure 2.1: *Typical structure of a quenching thermal cycle*

The OTOQ process hardens a batch production, treating the whole component by means of a thermal cycle typically composed of: a heating phase above the austenitising temperature, a maintaining phase that uniformises the temperatures across the parts and a final cooling phase realised through a liquid medium, Fig. 2.1. A mechanical part was considered for the realization of the mathematical model due to the higher computational cost of simulating the entire batch. The virtualization looks at the entire thermal cycle (Fig. 2.1) and the effects of the quenching fluid and the furnace were simulated by means of time-dependent interfaces that replicate their effect on the treated part, Fig. 2.5 and Fig. 2.4. Temperatures and HTC were managed through functions that firstly replicate the heating and the maintenance phases in the furnace and subsequently the cooling in the tank. Thus, the entire quenching thermal cycle was embedded into the virtualization. The model can be perfectly adapted to a range of different process conditions through the setting of the temperatures as well as HTC time-dependent interfaces. The estimation of the quenching outcomes was carried out by means of the implementation of a combination of mathematical laws in order to replicate the phenomenon throughout the quenching process, Fig. 2.2. The quenching virtualisation was realized by means of a tailored mathematical model in which each equation was self-implemented in an open software environment. It is notable that the temperature evolution of the treated part is

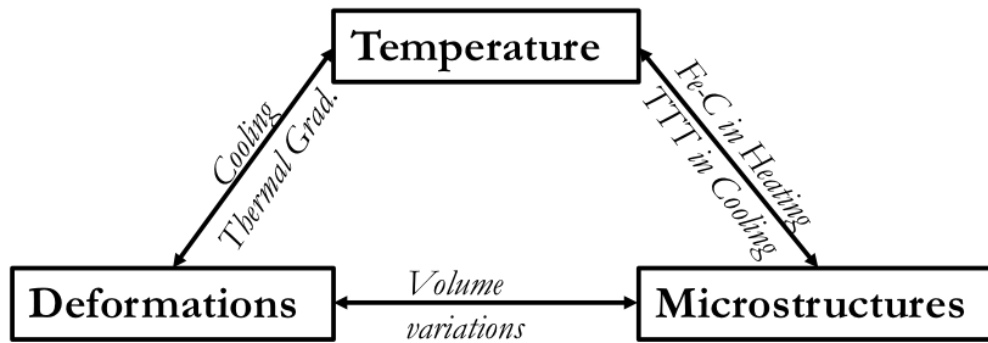


Figure 2.2: Structure of the quenching multi-physical model expressed in terms of temperature, microstructural and deformations couplings

linked not only to the material phase changes but also to the deformations. Fig. 2.2 shows the predicted OTOQ distortions.

The model geometry was outlined, taking into account the geometries derived from the experimental activity presented in Chap. 3. 2-D representations of the axisymmetric conditions were realised with 100Cr6 selected for the investigation, Fig. 2.3.

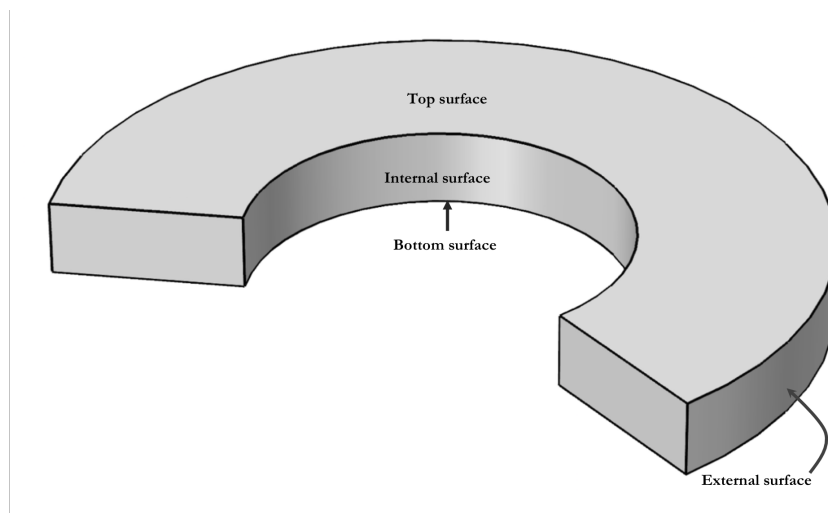


Figure 2.3: Axisymmetric component utilises for the modelling activity

The presented model was based on time-dependent simulation linking the temperature with the entire set of partial differential equations, describing the quenching process from a mathematical perspective. The outcomes were portrayed by the OTOQ model in terms of temperatures, microstructural phase changes and dimensional variations of the part deriving from the combination of distortions associated with both thermal gradients as well as material phase transformations.

2.3 Temperature Determination

The quenching process is classified as a thermal operation in which martensitic transformation is enabled by rapid cooling, which enhances the hardness and the resistance of mechanical parts. An accurate quenching simulation starts from a rigorous thermal description of the processed part throughout the entire quenching thermal cycle. The whole quenching process was virtualised through the replication of the heating in a furnace as well as the cooling in an oil tank to accurately forecast the outcomes, Fig. 2.1. The temperature evolution was governed by the Fourier law, eq. 2.1, considering both the heating phase from T_{room} to T_{furnace} and the cooling stage from T_{furnace} to T_{oil} , by specific time-dependent interfaces, Fig. 2.4, and Fig. 2.5.

$$\rho C_p \frac{\partial T}{\partial x} + \rho C_p \nabla T + \nabla \mathbf{q} = Q \quad (2.1)$$

$$\mathbf{q} = -k \nabla T$$

Temperatures and heat transfer coefficients (HTCs) were addressed as the variables in order to replicate the effects of the furnace (red arrows in Fig. 2.4, and Fig. 2.5) and the oil tank (blue arrows in Fig. 2.4, and Fig. 2.5). The switching from heating to cooling phases was managed by a linear condition to avoid a step function and ensure that there were no mathematical errors throughout the calculation - represented by the dotted lines Fig.2.4, and Fig. 2.5.

Heating and cooling stages were set through constant values of temperatures for both quenching facilities, mirroring the real-process conditions, see. Chap 3. The furnace and oil temperatures were set at 850°C and 50°C, defining the initial conditions and replicating the experiments, Fig. 2.4 and Fig. 2.5. Air and oil HTCs were respectively assigned to the heating and to the cooling phases. At the beginning of the quenching process, the part was virtually placed in the furnace (T_{furnace}) for the austenitising time (t_{heating}), to simulate the heating and maintaining phase and also the HTC of the air. Thus, the furnace effect was replicated in full and represented as the red arrows of Fig.2.4, and Fig. 2.5.

In the oil tank, time-dependent interfaces were designed to replicate the quenching bath and define the typical process values in terms of temperatures ($T=50$ °C as

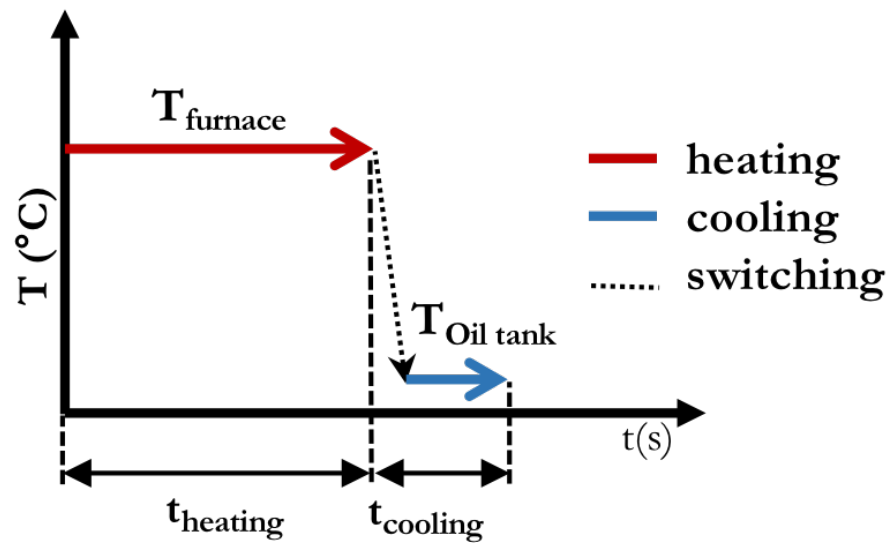


Figure 2.4: *The temperature time-dependent interface for the OTOQ modelling*

above-mentioned), HTC and the type of oil used as the cooling agent - blue arrows in Fig. 2.4, and Fig. 2.5. The quenching model was based on time-dependent simulation,

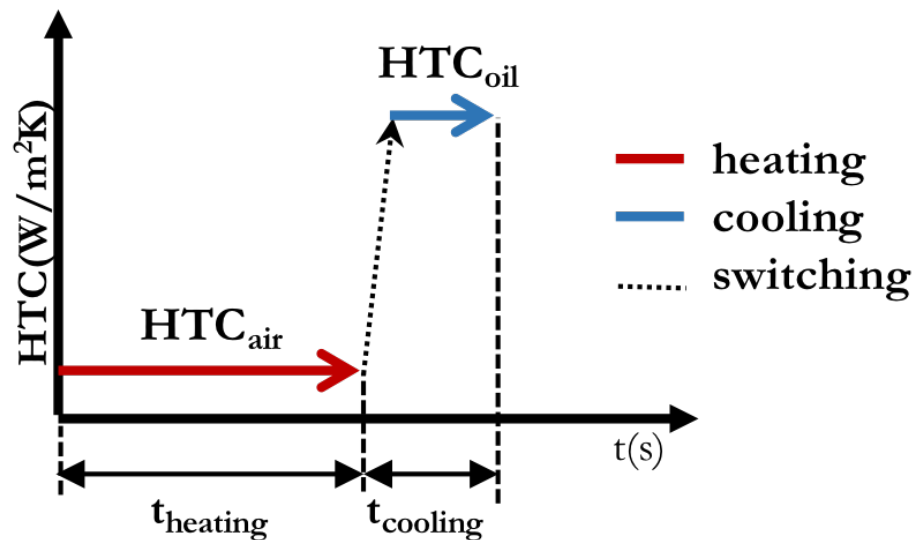


Figure 2.5: *The HTC time-dependent interface for the OTOQ modelling*

allowing every possible thermal cycle to be investigated. The cooling phase was identified not only by lower temperature and higher HTCs but also by less time in comparison with the other thermal sections, Fig. 2.4, and Fig. 2.5. Furthermore, the position of the treated part was mapped in the furnace and the oil tank by means of the displayed time-dependent interfaces, providing the boundary conditions of the model.

The cooling phase was identified by not only lower temperature and higher HTC's but also less simulation time in comparison with the other thermal sections, Fig. 2.4, and Fig. 2.5.

The inward and outward heat fluxes were estimated through convective conditions (Eq. 2.2) across the surfaces of the part, taking into account the temperatures and the HTC's, Fig. 2.4 and Fig. 2.5.

$$q_0 = HTC_{\text{furnace-bath}}(T_{\text{furnace-bath}} - T_{\text{Fourier}}) \quad (2.2)$$

The time-dependent functions were respectively assigned to $T_{\text{furnace-bath}}$ and $HTC_{\text{furnace-bath}}$, while the temperature of the part was managed by Eq. 2.1. Combining the time-dependent interfaces with Eq. 2.2 and Eq. 2.1, the quenching model was able to forecast the temperature evolution throughout the thermal cycle.

The heat flux across the boundaries was linked to the selection of the most suitable value of HTC's in order to replicate the experimental conditions. No variations were encountered throughout the heating with the same process conditions maintained, giving fixed values of furnace HTC's for all the surfaces. As a counterpart, different cooling steps were developed using liquid mediums throughout the cooling stage and modifying HTC magnitudes from austenitising to room temperature, black line in Fig. 2.6, [19]. The actual HTC trend was not recorded due to lack of real-data acquired through the experiments. An enhancement of the model complexity as well as the calculation time is necessary to ensure more accurate predictions.

An average value of HTC is compared with a real trend along the quenching cooling phase, highlighting the differences Fig. 2.6.

Overestimations for vapour blanket and the convective stages can be shown compared to an average value (red dotted arrows in Fig.2.6), whereas an HTC underestimation is shown for the nucleate boiling phase, grey dotted arrows in Fig. 2.6. In conclusion, the average values of HTC's were tested in order to replicate real quenching cooling conditions.

The quenching model was focused on distortion previsions not considering the quenchant fluid-dynamics. The first release was characterized by average values of HTC's throughout the whole thermal cycle. The same value of HTC was set for each

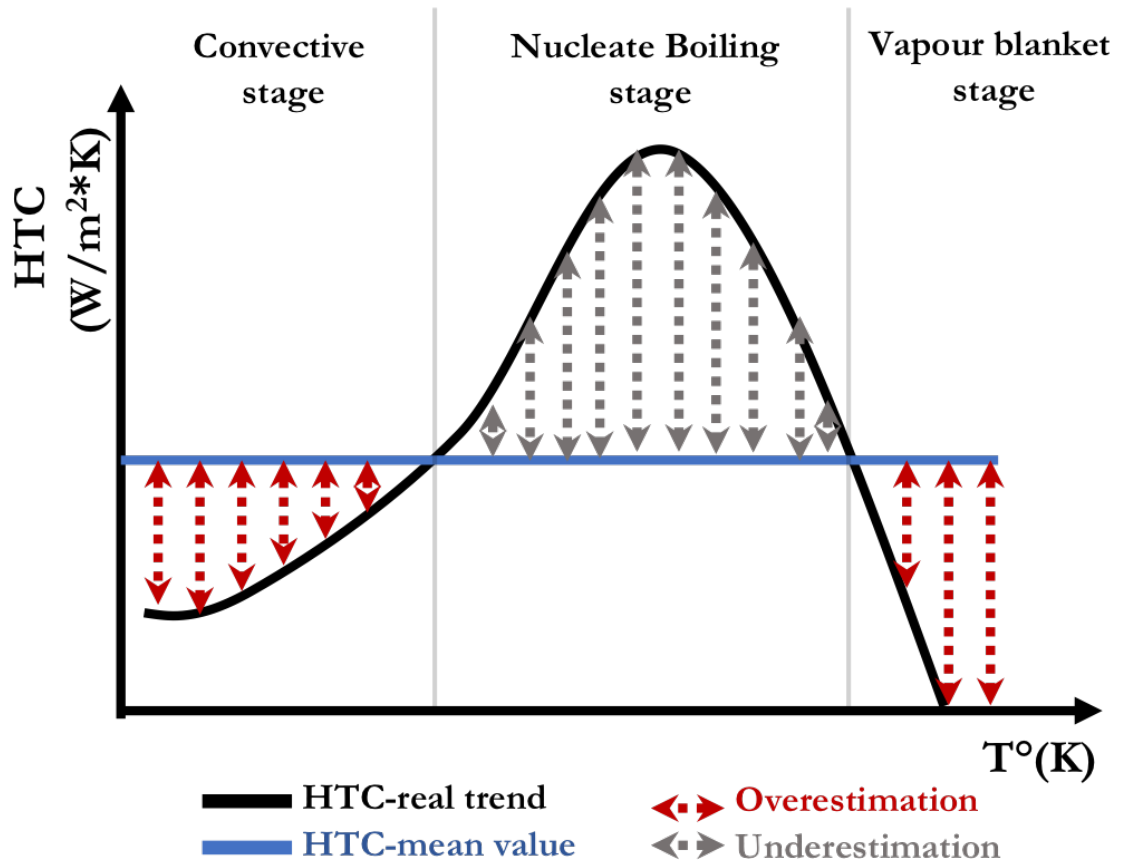


Figure 2.6: Comparison between real and implemented HTC trends throughout a quenching cooling phase

surface during the heating stage. In contrast, a virtualisation based on unequal cooling conditions specially developed along the OTOQ process that shows the effect of HTCs throughout the cooling process will be discussed in depth in Chap. 4.

Microstructural evolutions and deformation assessments have been linked to the temperature evolution of the process and this understanding represents a milestone in quenching simulation. In the following section, the microstructural field will be introduced, illustrating the implementation of material phase changes for the 100Cr6.

2.4 Implementation of the microstructural evolution

2.4.1 Determination of the starting conditions

A high carbon material content 100Cr6 was utilised to simulate the OTOQ process. 100Cr6 is a hyper-eutectoid steel typically composed of pearlite and carbides constituted

of cementite (Fe_3C) and Chromium carbides that were considered into the Fe_3C to simplify the model. A TTT diagram was used to model the diffusive microstructural transformations along the quenching cooling phase. The heating process was implemented through the Fe-C diagram, gauging the initial material composition by means of the lever rule, Fig.2.7.

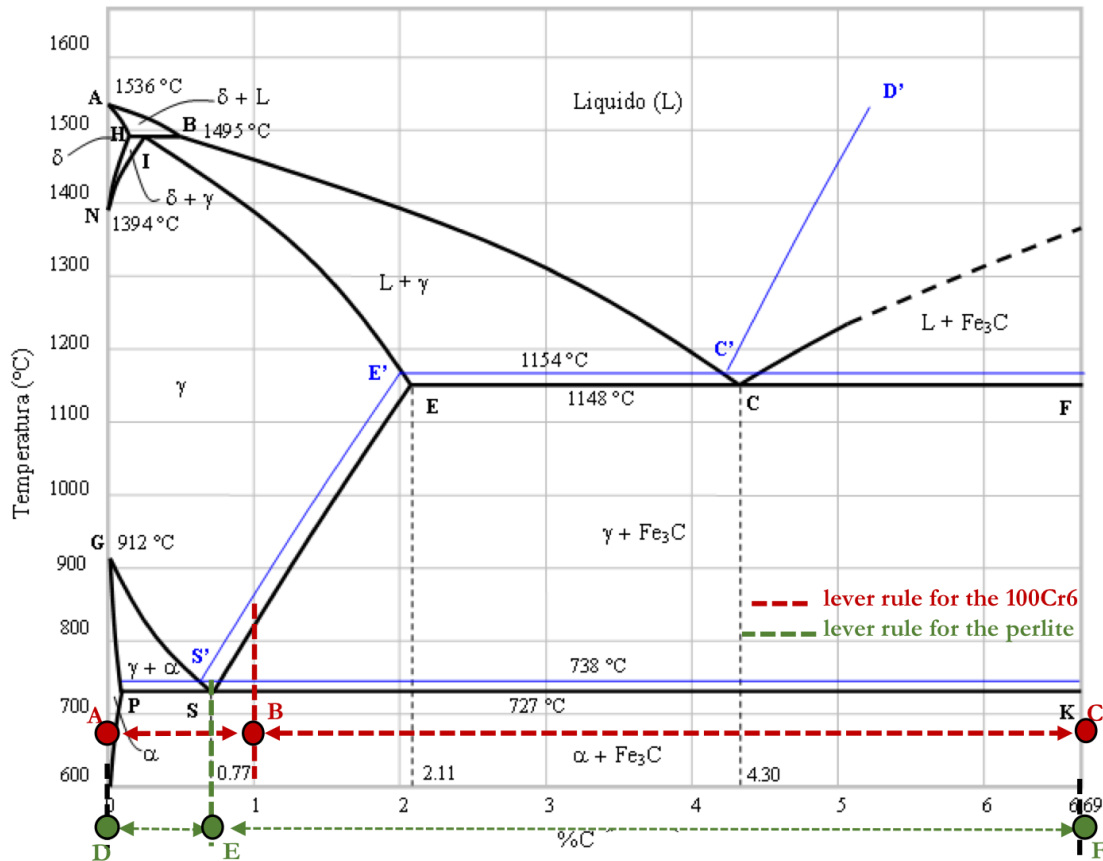


Figure 2.7: The Fe-C state diagram utilised for the evaluation of the starting material microstructure

Thus, the initial microstructure was completely reconstructed in terms of ferrite ($\text{Fe-}\alpha$) and Fe_3C , starting from a carbon percentage equal to 1% and reproducing the 100Cr6, Fig. 2.7. The following ratios were used to determine the percentages of pearlitic and carbides phases through the lever rule, red dotted line in Fig. 2.7.

$$\%Perlite = \frac{\overline{BC}}{\overline{EC}} \quad (2.3)$$

$$\%\text{Fe}_3\text{C} = \frac{\overline{EB}}{\overline{EC}} \quad (2.4)$$

The material microstructure was initially composed of 96,3% pearlite and 3,7% Fe_3C , Eq. 2.3 and Eq. 2.4. The pearlite was characterized by a lamellar microstructure of $Fe-\alpha$ and Fe_3C ; dividing the pearlitic percentage (96,3 %) into both phases by means of the lever rule, green dotted line in Fig. 2.7.

$$\%Ferrite = \frac{\overline{EF}}{\overline{BF}} \quad (2.5)$$

$$\%Fe_3C = \frac{\overline{DE}}{\overline{BF}} \quad (2.6)$$

As a result, the 100Cr6 microstructure was composed of 86% $Fe-\alpha$ and 14% Fe_3C derived from two factors. Fig. 2.8 portrays the whole conducted process, resulting in the final microstructural percentages.

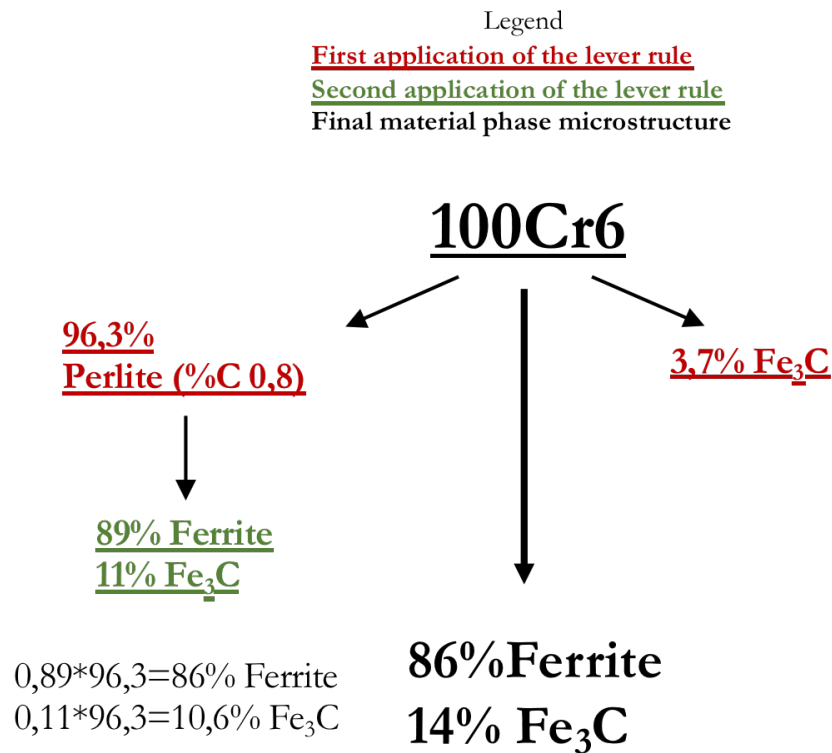


Figure 2.8: The 100Cr6 starting microstructure for the OTOQ modelling

2.4.2 Microstructural development in the heating stage

The whole microstructural evolution was simulated throughout the quenching thermal cycle, taking into account both the cooling and the heating in order to accurately assess deformations that stem from the thermal gradients encountered in the process as well as volume variations induced by microstructural changes.

The Fe-C diagram determines the initial material microstructure (par. 2.4.1) and the critical temperatures A_{c1} and A_{cm} that enable the material phase changes. Fig. 2.9 magnifies the Fe-C diagram to show the considered transition temperatures for a steel composed of 1% carbon and without alloy-elements. The material data sheet lists the evaluation of A_{c1} and A_{cm} based on the relevant chromium percentage included in the steel matrix, 1,4-1,6 %Cr. Thus, the critical temperatures were imposed equal to:

$$A_{c1}=755\text{ }^{\circ}\text{C}$$

$$A_{cm}=785\text{ }^{\circ}\text{C}.$$

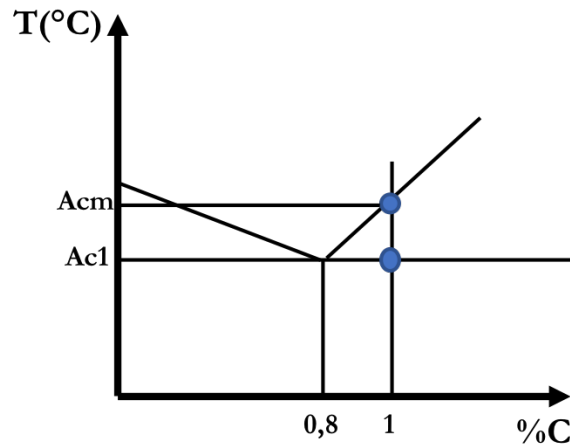


Figure 2.9: *The 100Cr6 critical temperatures based on the Fe-C diagram*

The microstructural evolution was connected to temperature variations induced by either the furnace or the oil in the tank (see. par. 2.3) hence, it was correlated not only to temperatures but also to the duration of the thermal cycle.

Ferritic, austenitic and carbide phases were mapped throughout the heating, considering critical temperatures and the starting 100Cr6 microstructure previously determined in par. 2.4.1, 86%Fe- α and 14% of Fe_3C . Each phase evolution was analysed coming

through fixed time steps along the thermal cycle that correspond to the transition temperatures achieved by the part through temperature assessments, as detailed in par. 2.3. The microstructural evolutions were described by linear interpolations, calculating the phase fraction variations but not the density changes between material phase modifications, [43]. The critical temperatures were turned into ranges in order to consider the transformation delays (hysteresis of the transformations) and to avoid step functions.

For the heating stage

$$A_{c1} = 750^{\circ}\text{C} \rightarrow A_{c1} = (745 - 755)^{\circ}\text{C}$$

$$A_{cm} = 785^{\circ}\text{C} \rightarrow A_{cm} = (770 - 800)^{\circ}\text{C}$$

Fig.2.10 displays ferritic (red line), austenitic (orange line) and carbide (blue line) evolutions coming through the heating. Microstructural alterations were observed until

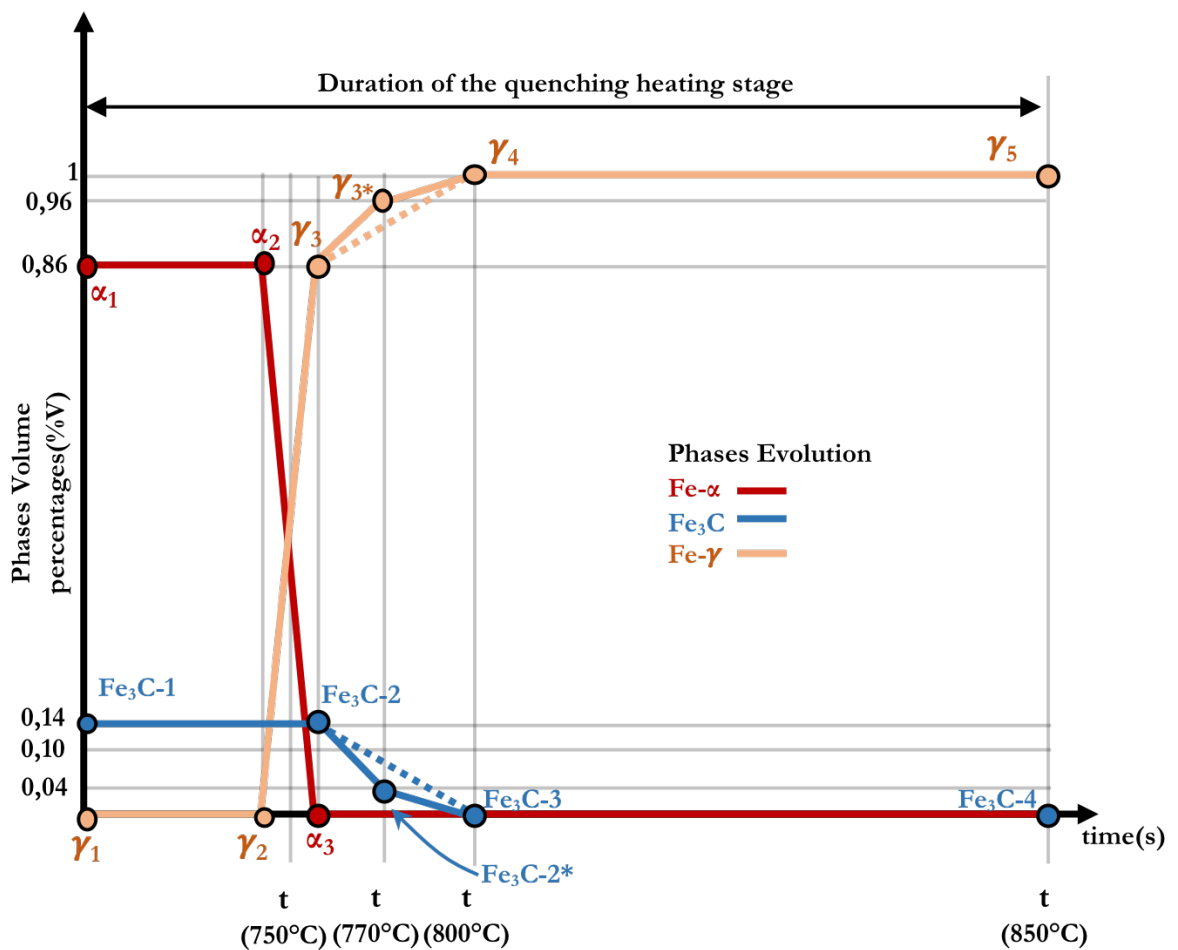


Figure 2.10: Material implementation according to critical temperature

A_{c1} resulting in the same initial composition: 0.86% and 0.14% Fe_3C , respectively portrayed by the segment lines $\overline{\alpha_1\alpha_2}$ $\overline{Fe_3C - 1Fe_3C - 2}$. The Fe- α was then transformed into austenite (Fe- γ) by means of the temperature enhancement induced by the furnace, $\overline{\alpha_2\alpha_3}$ and $\overline{\gamma_2\gamma_3}$. The Ferritic and austenitic phase variations were accomplished by the linear interpolations. Each function was expressed in the Kelvin rather than the Celsius scale.

Ferritic transformation between 745°C-755°C

$$-\alpha_2: T_2=(745 + 273)^\circ C=1018K \text{ and } \%Fe-\alpha_2=0,86$$

$$-\alpha_3: T_3=(755 + 273)^\circ C=1028K \text{ and } \%Fe-\alpha_3=0$$

$$\overline{\alpha_2\alpha_3} = 0.86 - \frac{T_{part} - 1018}{10} * 0,86 \quad (2.7)$$

Austenitic transformation between 745°C-755°C

$$-\gamma_2: T_2=(745 + 273)^\circ C=1018K \text{ and } \%Fe-\gamma_2=0$$

$$-\gamma_3: T_3=(755 + 273)^\circ C=1028K \text{ and } \%Fe-\gamma_3=0,86$$

$$\overline{\gamma_2\gamma_3} = \frac{T_{part} - 1018}{10} * 0,86 \quad (2.8)$$

Afterwards, the Fe_3C was gone into the solid solution enhancing as a result Fe- γ and completely transforming the initial pearlite into austenite for a total amount of 96% at 770 °C.

Fe_3C transformation between 755°C-770°C

$$-Fe_3C-2: T_2=(750 + 273)^\circ C=1023K \text{ and } \%Fe_3C-2=0,14$$

$$-Fe_3C-2*: T_2*=(770 + 273)^\circ C=1043K \text{ and } \%Fe_3C-2*=0,04$$

$$\overline{Fe_3C - 2Fe_3C - 2*} = \frac{T_{part} - 1023}{20} * (-0.1) \quad (2.9)$$

Fe- γ transformation between 755°C-770°C

$$-\gamma_3: T_3=(755 + 273)^\circ C=1028K \text{ and } \%Fe-\gamma_3=0,86$$

$$-\gamma_3*: T_3*=(770 + 273)^\circ C=1043K \text{ and } \%Fe-\gamma_3*=0,96$$

$$\overline{\gamma_3\gamma_{3^*}} = 0.86 + \frac{T_{\text{part}} - 1028}{15} * (0.1) \quad (2.10)$$

Finally, when the A_{cm} critical temperature was reached by the heating, 100% of austenite microstructure was obtained, including the remaining 4% of Fe_3C . The following relationships describe the last microstructural changes:

$$-\gamma_{3^*}: T_{3^*} = (770 + 273)^\circ\text{C} = 1043\text{K} \quad -\% \text{Fe} - \gamma_{3^*} = 0,96$$

$$-\gamma_4: T_4 = (800 + 273)^\circ\text{C} = 1073\text{K} \quad -\% \text{Fe} - \gamma_4 = 1,00$$

$$\overline{\gamma_{3^*}\gamma_4} = 0.96 + \frac{T_{\text{part}} - 1043}{30} * (0.04) \quad (2.11)$$

$$-\text{Fe}_3\text{C}-2^*: T_{2^*} = (770 + 273)^\circ\text{C} = 1043\text{K} \quad -\% \text{Fe}_3\text{C}-2^* = 0,04$$

$$-\text{Fe}_3\text{C}-3: T_3 = (800 + 273)^\circ\text{C} = 1073\text{K} \quad -\% \text{Fe}_3\text{C}-3 = 0$$

$$\overline{\text{Fe}_3\text{C}-2 * \text{Fe}_3\text{C}-3} = 0.04 + \frac{T_{\text{part}} - 1043}{30} * (-0.04) \quad (2.12)$$

The last section of the heating $\overline{\gamma_4\gamma_5}$ was characterized by a complete austenite microstructure, taking into account the temperature evolution from $T = 800^\circ\text{C}$ (the highest critical temperature) to $T = 847^\circ\text{C}$ (the real-furnace condition) and replicating the maintaining step of the thermal cycle. The sections $\overline{\gamma_3\gamma_{3^*}}$ and $\overline{\gamma_{3^*}\gamma_4}$ could be joined in $\overline{\gamma_3\gamma_4}$ (orange dotted line in Fig. 2.10). In the same manner, the carbide dissolution could be noted, coming through $\overline{\text{Fe}_3\text{C}-2 * \text{Fe}_3\text{C}-3}$ plus $\overline{\text{Fe}_3\text{C}-2 * \text{Fe}_3\text{C}-3}$ to $\overline{\text{Fe}_3\text{C}-2 * \text{Fe}_3\text{C}-3}$, (blue dotted line in Fig. 2.10). The carbide dissolutions were separately evaluated, as reported by Fig. 2.8.

In conclusion, each material phase modification was implemented through nested *if-then-else* conditions, establishing the right-path of microstructural changes based on temperature evolution as well as cycle time.

2.4.3 Microstructural development in the cooling stage

The cooling stage was subsequently activated through the switching of HTCs and temperatures in order to replicate the oil in the tank (dotted and blue lines in Fig. 2.11), and when the heating phase ends (red arrow in Fig. 2.11).

The material phase evolution was achieved considering pearlite ($\text{Fe-}\alpha$ and Fe_3C), that were included in the same percentage without dividing them as was done in the heating, carbides, that were represented through Fe_3C and bainitic and martensitic microstructures.

Starting from a complete austenitic phase γ_5 (Fig. 2.12), the initial 4% of Fe_3C was ejected from the steel matrix when A_{cm} was achieved by the treated part - set equal to 817°C in the Fe-C diagram, Fig. 2.7.

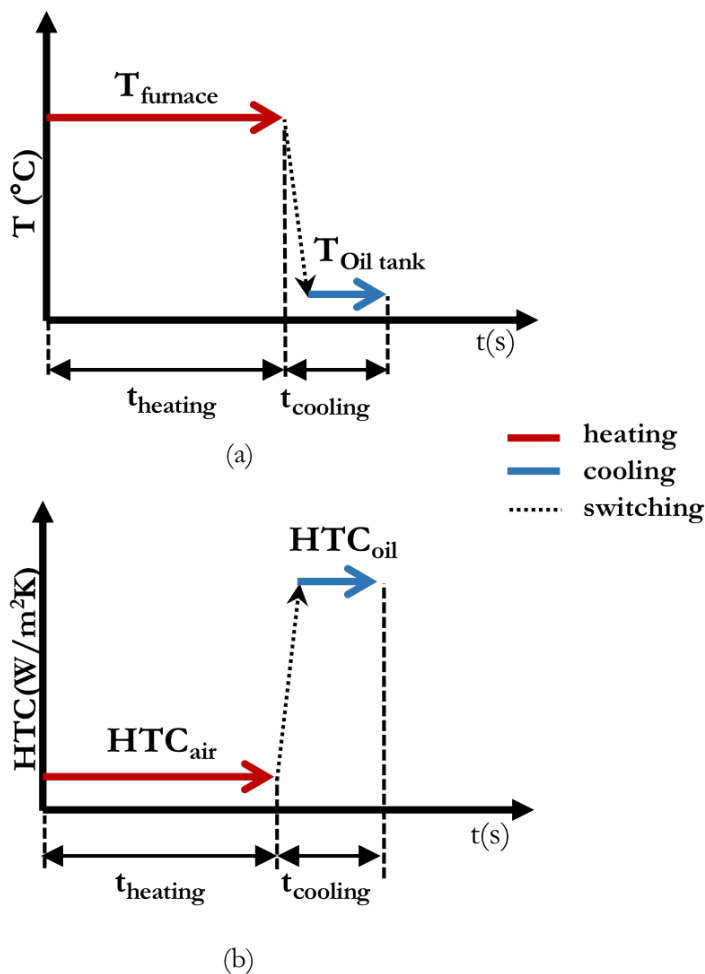


Figure 2.11: The HTC and temperature time-dependent interfaces

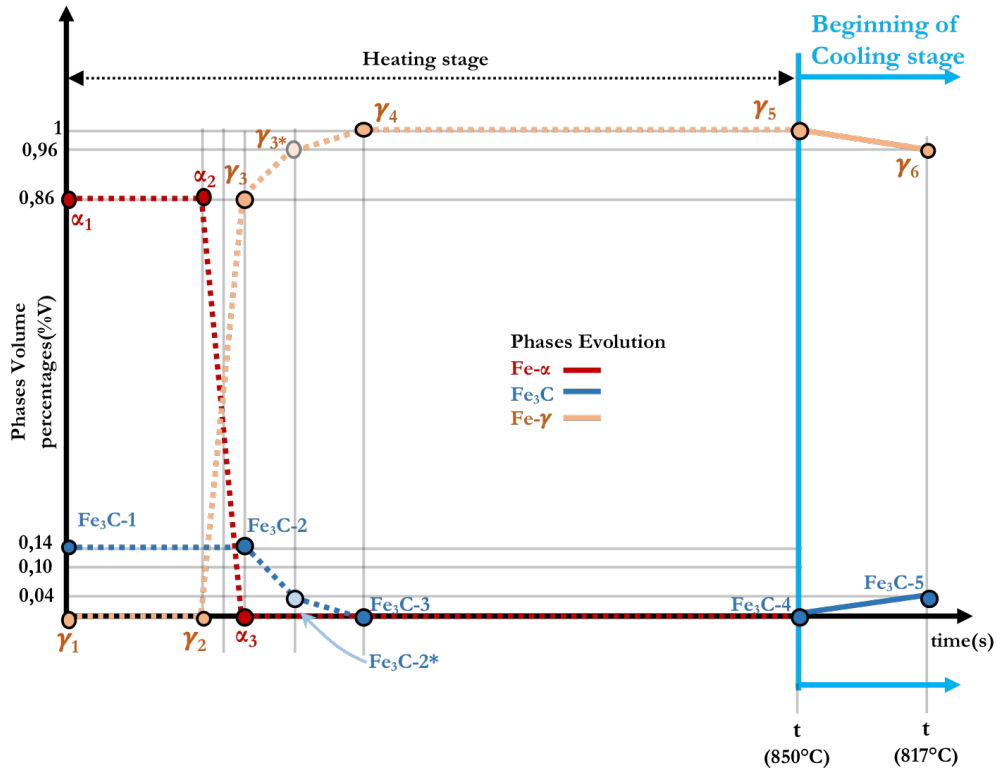


Figure 2.12: The cooling path until A_{cm}

The Fe_3C formation was resolved in a linear interpolation with the corresponding austenitic decrease:

Fe₃C transformation between 847°C – 817°C

- Fe_3C-2 : $T_2=(847 + 273)^\circ C=1070K$ and $\%Fe_3C-4=0$,
- Fe_3C-2^* : $T_2^*=(817 + 273)^\circ C=1090K$ and $\%Fe_3C-5=0,04$

$$\overline{Fe_3C - 4Fe_3C - 5} = (T_{part} - 1120)/30 * (-0.04) \quad (2.13)$$

Fe-γ transformation between 847°C – 817°C Fe₃C transformation between

- $847^\circ C-817^\circ C -\gamma_5$: $T_5=(847 + 273)^\circ C=1070K$ - $\%Fe-\gamma_5=1$
- γ_6 : $T_5=(817 + 273)=1090K$ - $\%Fe-\gamma_6=0,96$

$$\overline{\gamma_5\gamma_6} = 1 + \frac{T_{part} - 1120}{30} * 0.04 \quad (2.14)$$

The Fe-C diagram was employed until γ_6 to determine the microstructural evolution.

The austenite transformation was then based on diffusive as well as non-diffusive transformations, using the TTT diagram and JMAK equation [43]. A material phase evolution was presented in [43], looking at the quenching cooling phase and implementing a carburising material as well as pearlitic and martensitic transformations. A hardening steel and bainitic transformation were added, tuned and modified [43]. Firstly, the 100Cr6 TTT diagram was divided into two parts, corresponding to the pearlitic nose, identifying the transition temperature between pearlitic and bainitic microstructures, Fig. 2.13; while the martensitic transformation was only activated below M_s . The material evolution was added to the incubation time (t_s) ([38]), turning the TTT into the Continuous Cooling Transformation (CCT) diagram to consider the rapid cooling.

Fig. 2.13 portrays the tailored 100Cr6 TTT diagram, showing the evaluation points for the initial (blue point) as well as the final (orange and green points) material transformation curves by measuring isothermal cooling steps every 20°C below A_c1 .

Each temperature was related to initial and final transformation times (t_s , t_f) as well as the starting and ultimate microstructural phase percentages, 1% and 99% respectively, connected to t_s , t_f , [43]. The activation function was described in [43]. Pearlitic and bainitic functions were extrapolated from the TTT diagram, evaluating the material changes throughout the quenching cooling.

$$(t_f - t_s)f(T, \%C) = \int_{t_s}^{t_f} f(T, \%C)dt = \int_{0,01}^{0,99} \frac{dm}{1-m} = -\log \frac{0,01}{0,99} \quad (2.15)$$

$$f(T, \%C) = -\frac{1}{t_f - t_s} \log \frac{0,01}{0,99} \quad (2.16)$$

Thus, a specific activation function was determined for both pearlitic as well as bainitic microstructures through Eq. 2.16, imposing 1% as the carbon percentage. The pearlitic transformation was activated until 600°C, while the bainitic went from the pearlitic nose to 220°C, the last green point in Fig. 2.13 and just above M_s . The incubation time was implemented as described by means of the Scheil's Sum, eq. 2.17:

$$\int_{t_s}^{t_f} \frac{1}{t_s(T(t))} dt = 1 \quad (2.17)$$

The pearlitic and bainitic microstructural transformations were calculated using the

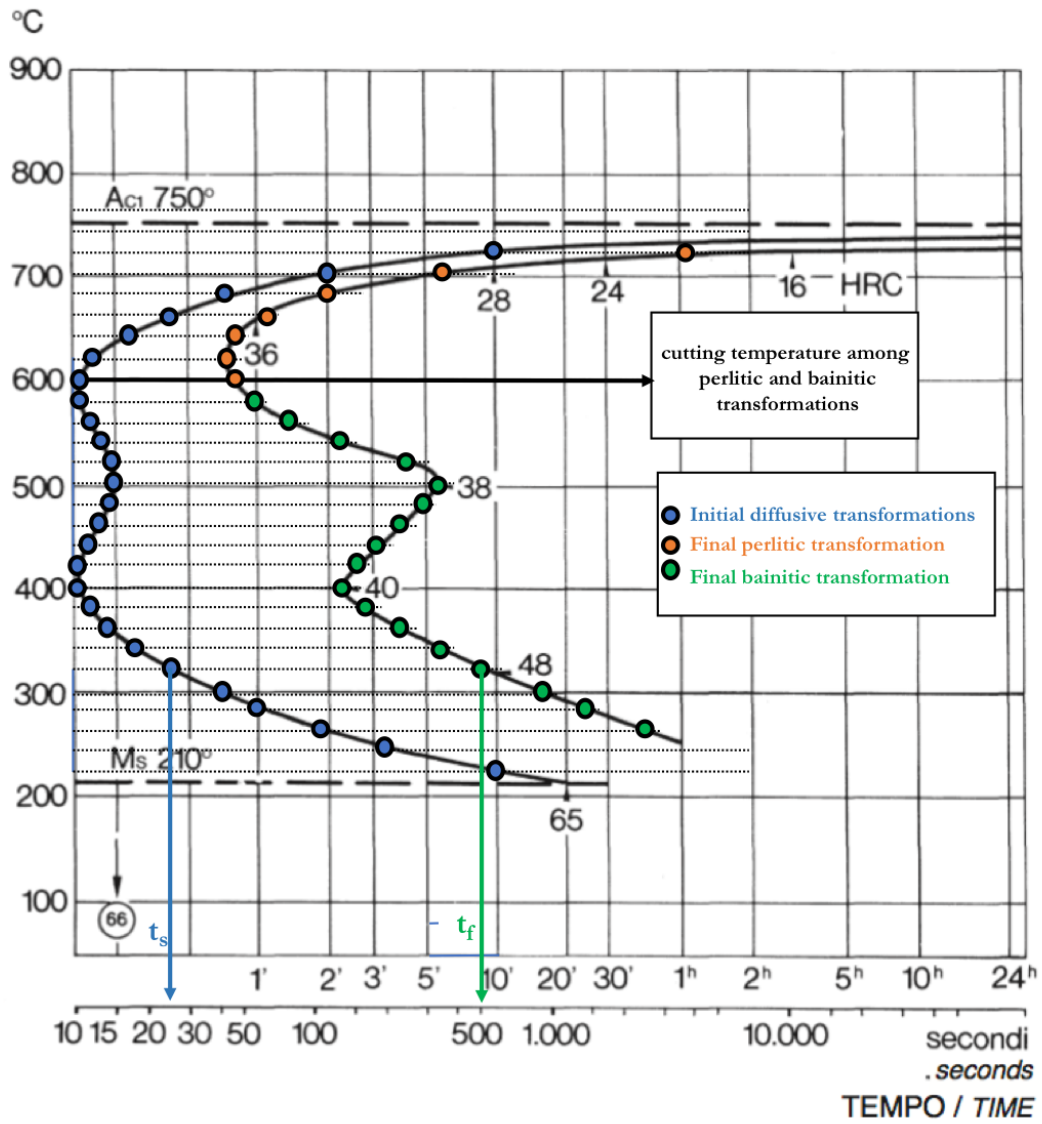


Figure 2.13: The pearlitic and bainitic activation points concerning the diffusive transformations

following partial differential equations:

1-Perlitic transformation

$$\frac{\partial p}{\partial t} = (1 - p - b - m)f_{\text{perlite}}(T, 1) \quad (2.18)$$

$$p(0) = 0 \text{ as the initial condition}$$

2-Bainitic transformation

$$\frac{\partial b}{\partial t} = (1 - p - b - m)f_{\text{bainite}}(T, 1) \quad (2.19)$$

$$b(0) = 0 \text{ as the initial condition}$$

The martensitic transformation was introduced into the model by means of the Koistinen-Marburger formula [43] that assesses:

3-Martensitic transformation

$$m_{\text{KM}}(T; \%C) = (1 - \exp^{-c_{\text{km}}(\%C)(M_s(\%C) - T_{\text{part}})})H(M_s(\%C) - TT_{\text{part}}) \quad (2.20)$$

In this case, the martensitic fraction m_{KM} was solely related to the variable T and the diffusive transformations. A step function was represented by the H that specifically activated the a-thermal transformation underneath the M_s , while the martensitic transformation rate was described by the coefficient c_{km} . The martensitic evolution was installed into the model by means of [43]:

$$\begin{aligned} \overline{m(T)} &= \min[m_{\text{KM}}(T; \%C), 1 - p - b - m]; \\ \frac{\partial m}{\partial t} &= [\overline{m(T)} - m] + g_m(T(t), \%C) \end{aligned} \quad (2.21)$$

$$m(0) = 0 \text{ as the } \textit{initial condition}$$

The activation function g_m was set $\frac{1}{50} \text{ s}^{-1}$, [43]. The par. 2.4.1, par. 2.4.2 and par. 2.4.3 show how the material phase evolution was handled throughout the whole quenching process. However, the links among each thermal section have not yet been defined; the next section looks at these connections and how the microstructural evolution can be replicated.

2.4.4 Nested Conditions between the Heating and the Cooling phases

The mathematical model must be able to recognize the position of the treated part throughout the thermal cycle in order to accurately replicate both the heating and cooling phases. To achieve this calculation, a series of if-then-else conditions were applied to the presented material phase evolution and combined with the heating and cooling phases. (par. 2.4.2 and par. 2.4.3)

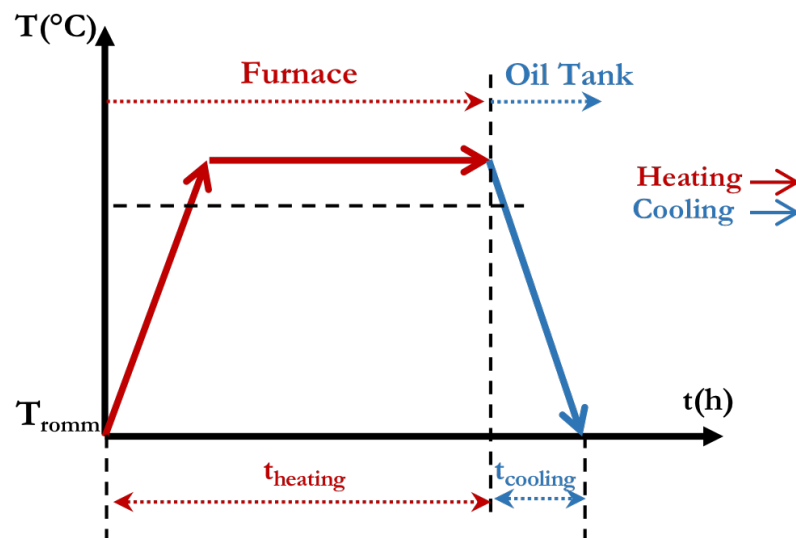


Figure 2.14: A quenching thermal cycle addressed to the evaluation of heating and cooling times

The conditions were based on time as well as temperature evolution to precisely activate the material phase changes along the computation. Setting the heating and cooling times as " t_{heating} " and " t_{cooling} " considering both the starting point and the ferritic dissolution ($\text{Fe-}\alpha$), the first nested condition was set as follows:

$$\begin{aligned} & \text{if}(\text{condition, then, else}) \\ & \text{if}(t < t_{\text{heating}}, (1), 0) \text{ (time condition)} \\ & (1) \rightarrow \text{if}(T_{\text{part}} \geq 1028\text{K}, 0, (2)) \text{ (} T_{\text{part}} \geq 755^\circ\text{C)} \\ & (2) \rightarrow \text{if}(T_{\text{part}} > 1018\text{K}, \overline{\alpha_2\alpha_3}, \overline{\alpha_1\alpha_2}) \text{ (} T_{\text{part}} > 745^\circ\text{C)} \end{aligned}$$

The part was traced throughout the thermal cycle and *time condition* recognised whether it was in either the heating or the cooling phases. The $\text{Fe-}\alpha$ transformation was activated by the nesting temperature conditions $T_{\text{part}} \geq 755^\circ\text{C}$ that were already connected to the *time condition* by Eq. 2.1. As a result, the ferritic evolution was achieved and is pictured

by the red line in Fig. 2.10. The Fe_3C dissolution was fulfilled replicating the $Fe-\alpha$ evolution even when changing the temperature conditions. The following rules were applied:

Nested conditions for Fe_3C evolution

if($t < t_{heating}$, **(1-heating), (2-cooling)**) (*time condition*)

Nested conditions for the heating stage

(1-heating) \rightarrow if($T_{part} \geq 1073K$, $\overline{Fe_3C - 3Fe_3C - 4}$, (2)) ($T_{part} \geq 800^\circ C$)

(2) \rightarrow if($T_{part} \geq 1043K$, $\overline{Fe_3C - 2 * Fe_3C - 3}$, (3)) ($T_{part} \geq 770^\circ C$)

(3) \rightarrow if($T_{part} \geq 1023K$, $\overline{Fe_3C - 2Fe_3C - 2*}$, $\overline{Fe_3C - 1Fe_3C - 2}$) ($T_{part} \geq 750^\circ C$)

Nested conditions for the cooling

(2-cooling) \rightarrow if($T_{part} \geq 1090K$, $\overline{Fe_3C - 4Fe_3C - 5}$, $\overline{Fe_3C - 5}$) ($T_{part} \geq 817^\circ C$)

Fe_3C evolution was completely resolved by the nested conditions described above. The trend is depicted by the blue line in Fig. 2.10.

Finally, the austenite development was totally implemented merging heating cooling stages, orange line in Fig. 2.10:

Nested conditions for $Fe\gamma$ evolution

if($t \geq t_{heating}$, **(1-cooling), (2-heating)**) (*timely condition*)

Nested conditions for the cooling

(1-cooling) \rightarrow if($T_{part} \geq 1090K$, $\overline{\gamma_5}$, (1)) ($T_{part} \geq 847^\circ C$)

(2) \rightarrow if($T_{part} < 1090K$, $\overline{\gamma_6 - \%m - \%p - \%b}$, $\overline{\gamma_6}$) ($T_{part} < 817^\circ C$)

Nested conditions for the heating stage

(1-heating) \rightarrow if($T_{part} \geq 1073K$, $\overline{\gamma_4\gamma_5}$, (3)) ($T_{part} \geq 800^\circ C$)

(3) \rightarrow if($T_{part} \geq 1043K$, $\overline{\gamma_3*\gamma_4}$, (4)) ($T_{part} \geq 770^\circ C$)

(4) \rightarrow if($T_{part} \geq 1028K$, $\overline{\gamma_3\gamma_3*}$, (5)) ($T_{part} \geq 755^\circ C$)

(5) \rightarrow if($T_{part} \geq 1018K$, $\overline{\gamma_2\gamma_3}$, $\overline{\gamma_1\gamma_2}$) ($T_{part} \geq 745^\circ C$)

Eq. 2.18, Eq. 2.19, Eq. 2.20 were all enabled by condition (2), resulting in an evaluation of the final microstructures induced by the OTOQ process.

2.5 Evaluation of Quenching Distortions

The dimensional variations, induced by quenching processes, typically depend on thermal gradients as well as material phase transformations developed throughout the quenching process. Temperatures and microstructural evolutions have been analysed in the previous paragraphs (par.2.3 and par.2.4), leading to the determination of temperature differences (ΔT) and material modifications across the part as well as the gauging of thermal and microstructural deformations related to the quenching process by eq. 2.22 and eq. 2.23. Thermal deformations were estimated by:

$$\epsilon_{\text{thermal}} = \alpha(T(t), \text{phase}(T))(T_{\text{part}} - T_{\text{furnace-oil}}) \quad (2.22)$$

The coefficient of thermal expansion ($\epsilon_{\text{thermal}}$) was linked not only to temperatures and material phase evolutions but also to the time, considering the corresponding microstructural development throughout the thermal cycle. The T_{part} was determined by eq. 2.1 while $T_{\text{furnace-oil}}$ was connected to the temperatures defined by the time-dependent interfaces, Fig. 2.11.

Microstructural deformations were based on dimensional changes connected to the obtained microstructures and carbon percentages [17], Tab. 1.3. The microstructural deformations can be explained by:

$$\epsilon_{\text{microstructural}} = \sum_{i_{\text{phase}}=1}^n \text{fraction}_{i_{\text{phase}}} * \text{displacement}_{i_{\text{phase}}}(\%C) \quad (2.23)$$

All microstructural phases were considered by eq. 2.23 with thermal and microstructural deformations combined to evaluate the quenching distortions.

The volume variations were resolved for both Cartesian and Polar models, defining how the deformations were set across the part. Infinitesimal elements were taken into account for both mathematical representations, highlighting differences in terms of deformations. In the case of minute deformations Fig. 2.15 (a), volume variations for the case of Cartesian model were described by:

$$V_0 = x * y * z \text{ initial volume of the part}$$

$$V_f = (x + dx) * (y + dy) * (z + dz) \text{ final volume of the part}$$

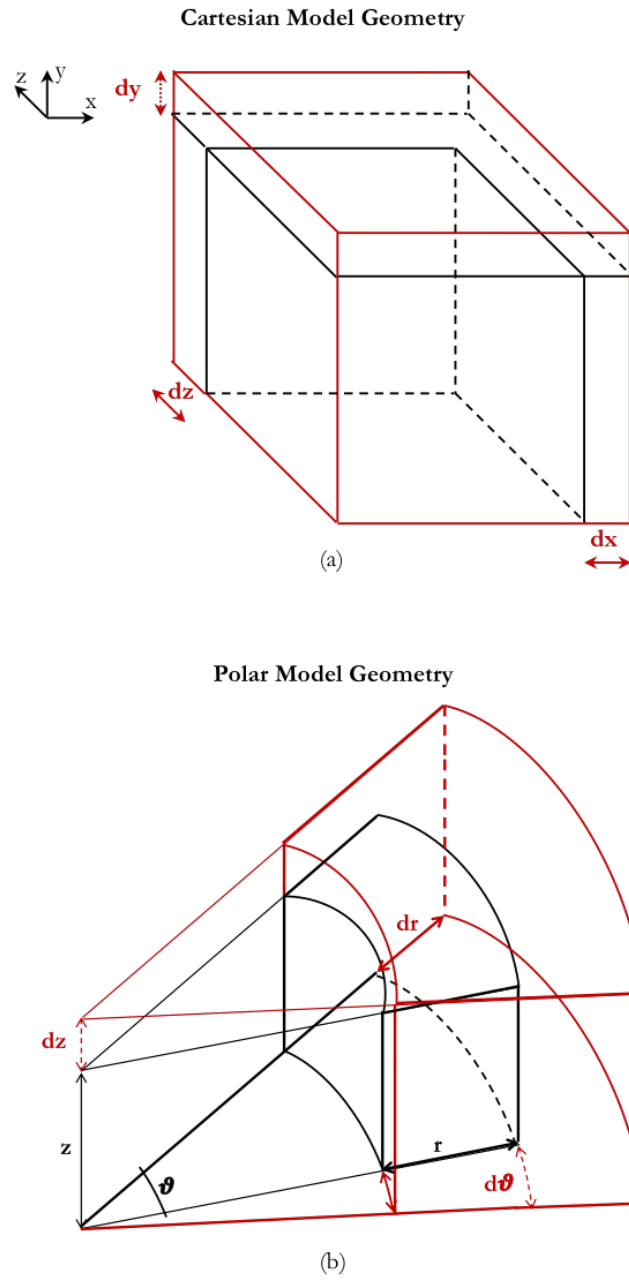


Figure 2.15: Volume variations connected to (a) Cartesian and (b) polar model geometries

$$\Delta V = \frac{V_f - V_0}{V_0} = \frac{dx}{x} + \frac{dy}{y} + \frac{dz}{z} \quad (2.24)$$

Volume variations were based on deformations along each main direction. Assigning to $dx = dy = dz = \Delta L$, volume variations can be rewritten through:

$$\frac{\Delta V}{V} = 3 * \frac{\Delta L}{L} \quad (2.25)$$

Looking at the polar model geometry, the volume modifications were resolved by:

$$V_0 = \pi * r^2 * z * \frac{\theta}{2\pi} = \frac{(r^2 * z * \theta)}{2}, \text{ initial volume of the part}$$

$$V_f = (r + dr)^2(\theta + d\theta) * (z + dz), \text{ final volume of the part}$$

$$\Delta V = \frac{V_f - V_0}{V_0} = \frac{d\theta}{\theta} + 2\frac{dr}{r} + \frac{dz}{z} \quad (2.26)$$

The volume variations were investigated for Cartesian and Polar models geometries by eq. 2.24 and eq. 2.26. A double radial displacement was determined in comparison with equal axial and circumferential deformations for the polar model, while the same x, y and z deformations were resolved for the whole Cartesian coordinates. Eq. 2.26 was employed to tune the thermal and microstructural deformations into the presented quenching model and correctly simulate the axisymmetric components, Fig. 2.3.

Finally, thermal and microstructural distortions were re-constructed to assess the deformations induced by quenching process.

2.5.1 Implemented Material properties

The material properties were set up through mixture rule equations depending on microstructural percentages, mechanical-thermal properties and temperatures. Eq. 1 shows a general set up of each material property. The properties are shown in Tab. 1.4.

$$\sum_{i_{\text{phase}}=1}^n (\text{fraction}_{i_{\text{phase}}} * \text{prop}_{i_{\text{phase}}}(T(K))) \quad (2.27)$$

2.6 Overview of Modelling Results

The OTOQ model was based on FEM, the discretization was defined by QL1 elements, identifying nodes where partial differential equations were resolved, Fig. 2.16. A 2-D model was calculated from the axisymmetric condition, turning 3-D simulation into 2-D virtualization, simplifying model settings and decreasing computational cost. The simulated outcomes were analysed by graphical visualisations, focussing on Fig. 2.17 (c), 2-D Fig. 2.17 (b) as well as global results.

The boundary conditions were reproduced by the time-dependent interfaces, enabling through Eq. 2.1 and Eq. 2.2 an evaluation of the temperature trends, portrayed in Fig. 2.17. Starting from Fig. 2.17 (a), temperatures were firstly analysed in terms of contour

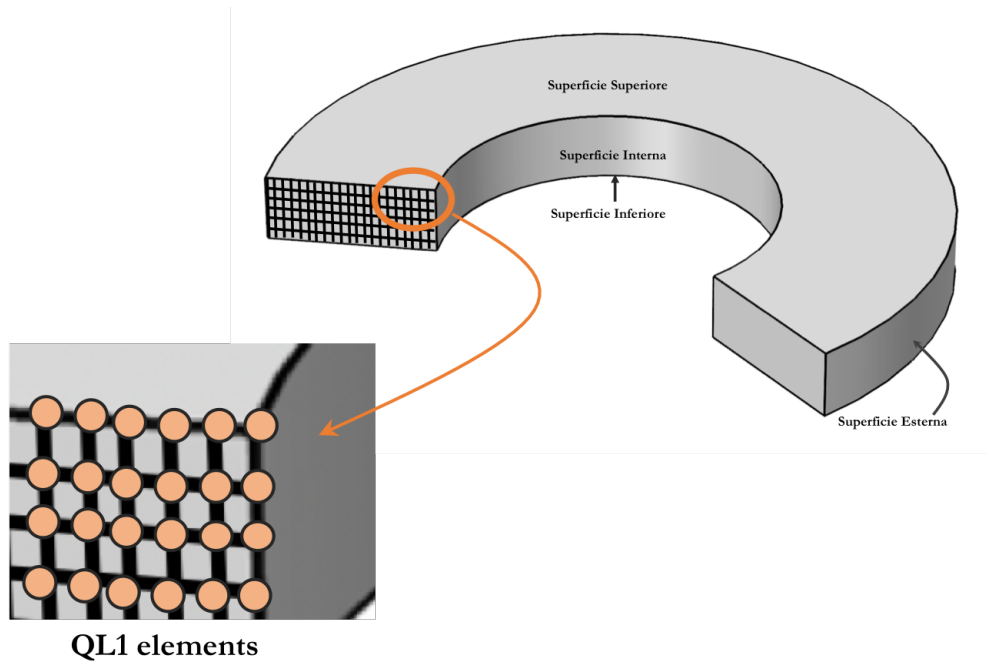


Figure 2.16: *OTOQ model to evaluate temperatures, microstructural evolution and deformations*

plots to underline critical portions of the part at fixed simulation time steps Fig. 2.17 (b). Thermal gradients were then analysed by means of evaluation points. Finally, complete cooling curves were investigated throughout the quenching process, leading to an examination of cooling paths. An overlapping between a singular temperature evolution and a time-dependent interface is illustrated in Fig. 2.17 (c). T_{furnace} is never undertaken by T_{part} during the heating phase whereas the temperature trends are placed just above T_{oil} at the end of the cooling. The switching from heating to cooling phases of the T_{part} corresponds directly to the variations of the time-dependent interface. The quenching simulation was based on well-determined temperature evolution to finely evaluate microstructures and deformations.

The outcomes were simultaneously calculated in each node by the whole set of equations. No post-process computation was realised for the quenching model. Reconstructing 1-D results across the section of the part, 2-D and 3-D outcomes were achieved. The results are strictly linked to HTC and the last chapter of the thesis is dedicated to the effects of this parameter, Chap. 4. An example regarding a complete microstructural evolution is displayed in Fig. 2.18. Final microstructures are linked to a range of cooling conditions dependant on temperature, HTC and positions across the transversal section. An example regarding a complete microstructural evolution is

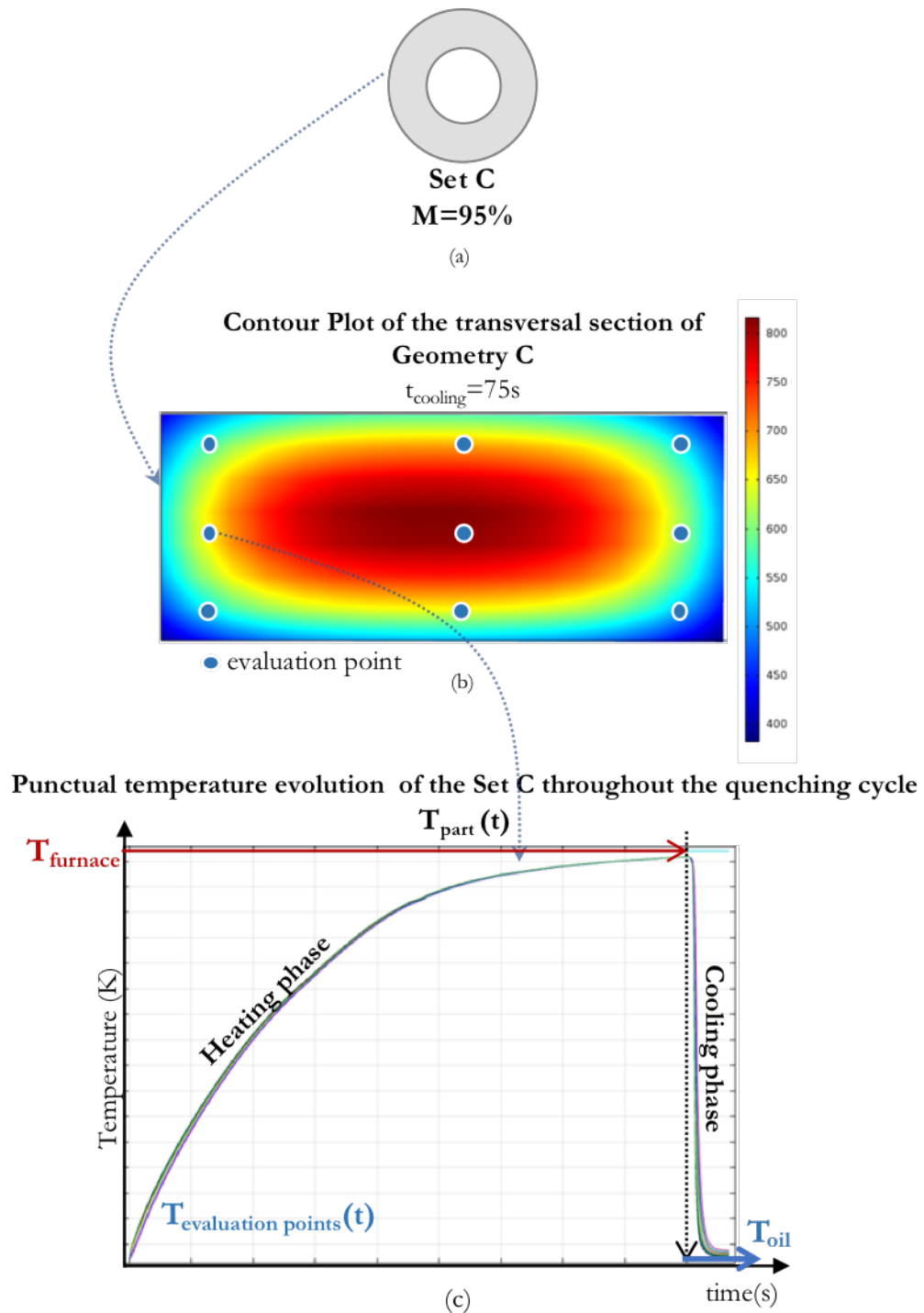


Figure 2.17: Thermal analysis performed by OTOQ model

displayed in Fig. 2.18. Final microstructures were linked to several cooling conditions that depend on temperatures, HTC and positions across the transversal section.

A radial deformation is portrayed in Fig. 2.19, evaluating not only thermal but also microstructural effects. The thermal expansion (1), (3) and austenitic contraction (2)

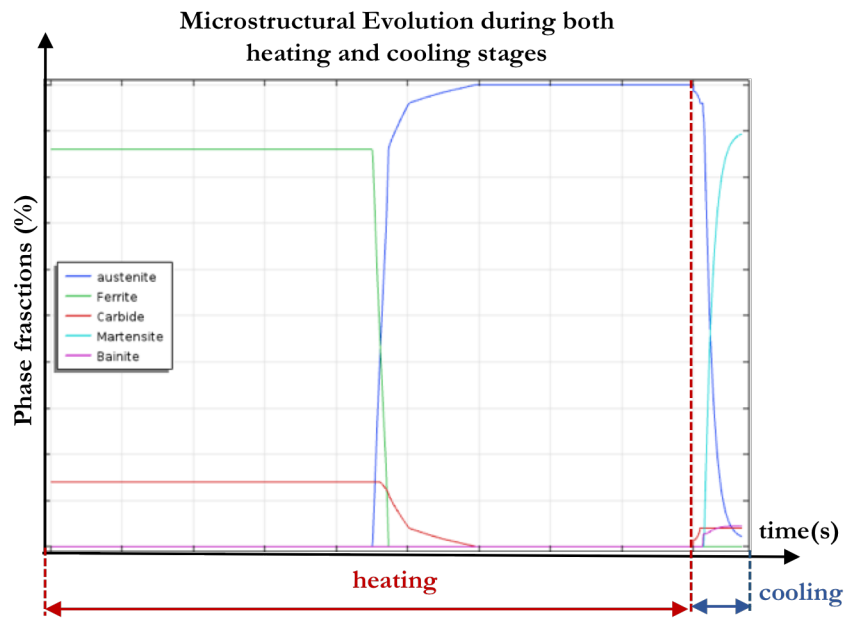


Figure 2.18: Microstructural evolution esteemed by OTOQ model

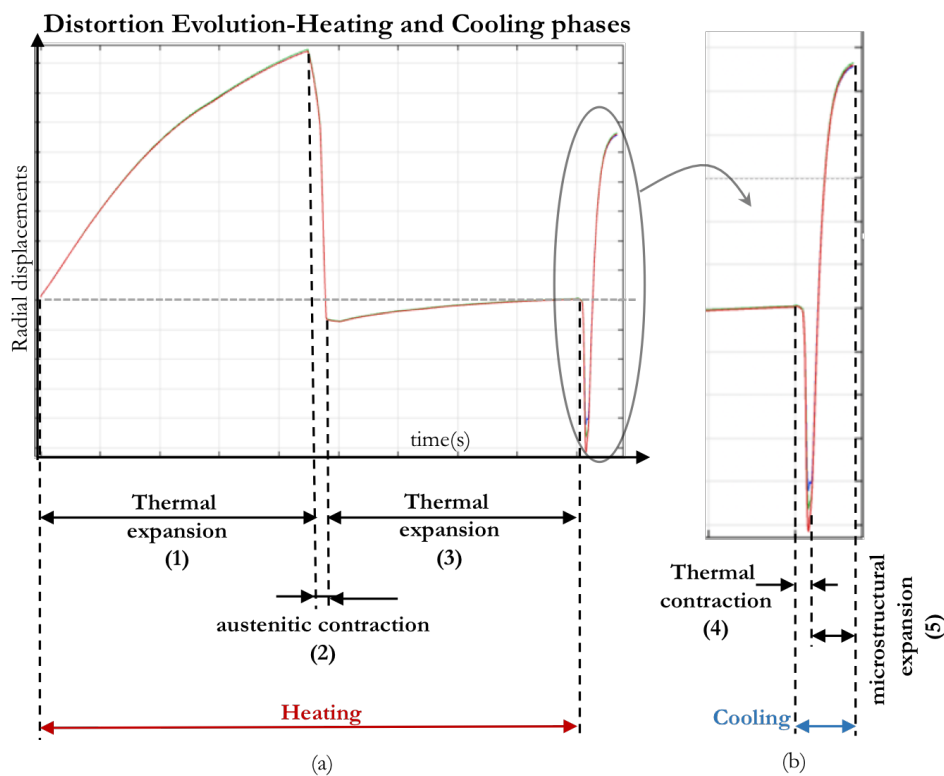


Figure 2.19: The radial displacement assessment derived from OTOQ model

coming from the change from initial to austenite microstructures were simultaneously implemented throughout the heating phase (T_{room} to A_{c3}). The cooling contraction (4) was then induced until the austenite turned into final microstructures such as bainite or

martensite (5). The outcomes were all linked together to accurately emulate and describe the full quenching process.

Investigations concerning the comparison between simulations and experiments are reported in Chap. 4.

2.7 Summary of modelling results

- An effective multi-physical approach based on FEM can be put in place to simulate the quenching process and replicate the entire quenching thermal cycle by means of time-dependent functions. The created model emulated the OTOQ process with the possibility to expand the virtualisation to DAOQ by accounting different values of HTC to replicate the effects of press and mould on the treated parts.
- Microstructural development was calculated and assessed for both the heating and cooling phases. The heating phase was based on the Fe-C diagram, allowing the evaluation of material changes and taking into account temperature as well as time evolutions; while the cooling phase was determined by a combination of the JMAK equation and TTT diagram along with the incubation time. The position of the part was completely defined along the quenching process by nested conditions regarding temperatures and time that enable the corresponding material transformations.
- Deformational models have been presented using Cartesian and Polar coordinates with a description of material properties and mixture rules given in order to explore and understand the setting of the presented mathematical model. A brief analysis was made of the capabilities of the model with particular attention placed on the workflow. Thermal, microstructural and deformational descriptions have been explained in order to show the capability and importance of the multi-physical approach.
- The following chapter looks at the experimental activities conducted in order to precisely define the dimensional and shape variations induced by a manufacturing cycle in both the OTOQ and DAOQ processes, examining a range of sustainability issues such as planarity tolerances.

Chapter 3

Experimental Investigations

3.1 Introduction

Mechanical components are typically deformed by heat treatment operations, changing dimensions and shape tolerances due to thermal gradients encountered throughout the thermal cycle as well as volume variations associated with material phase transformations. In order to compensate for these dimensional variations induced by the technological chain, machining allowances must always be planned during the design phase. This causes an extension of the manufacturing cycle and the addition of more raw materials to account for the final machining operations, such as the grinding process, which are necessary to obtain the precise design requirements in terms of dimension and shape.

Distortions can be accurately controlled by DAOQ through the combined effect of the mould and the press and thus, by modifying the mould design as well as the process parameters, a reduction of deformations can be obtained. Machining allowances can be both reduced overall and only added where they are considered indispensable to compensate the quenching effects. This could reduce or even avoid grinding operations, saving materials and shortening the technological cycle.

The presented experimental activity was designed to look at dimensional and shape evolutions of testing geometries. A standard manufacturing cycle of steel parts was considered, examining both OTOQ and DAOQ.

3.2 Design of the experiment

The experimental activities were engineered by means of the Design of Experiment (DoE) concepts. Three materials were investigated, involving a bearing ring steel 100CrMo7 as well as two carburising materials, 18NiCrMo5 and 20MnCr5. A billet was utilised for each material to realise five sets of axisymmetric geometries, using discs and rings characterized by variable transversal sections, Fig. 3.1. Three replications were manufactured for each set and material to statistically represent the collected data. Rings were obtained by modifying the inner holes while maintaining the same outer diameters and thicknesses throughout the sample geometries, Fig. 3.1. Each series was identified by either the theoretical thermal module ($M\%$) or the ratio between the volume V and the surface area S and expressed in percentage terms from 100% for disc-Set A to 72% for the thinnest ring-Set E. The effect of the transversal sections, typically expressed by the ratios $\frac{d_i}{d_e}$, were included in $M\%$.

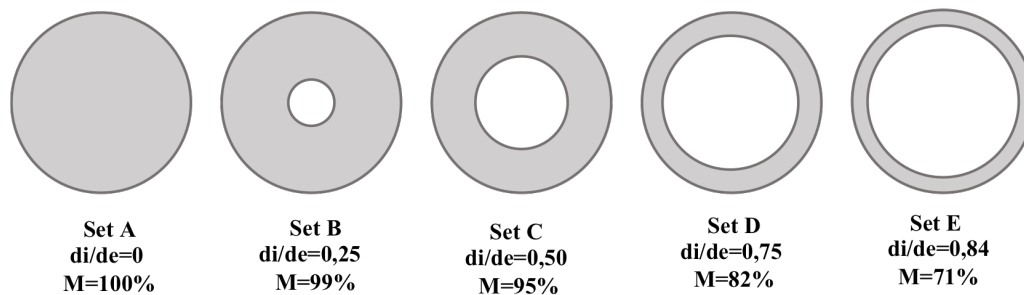


Figure 3.1: *The experimental testing geometries*

A sequence of six technological operations was defined to comprehend both OTOQ and DAOQ. Prior to the machining phase, all the components underwent a spheroidizing annealing, *Ph00*, and uniform starting microstructures were obtained (dependant on chemical compositions). The manufacturing cycle was composed of the following list of operations (Fig. 3.3):

- Spheroidizing annealing, named *Ph00*;
- Machining, named *Ph01*;
- Traditional Open Tank Oil Quenching (OTOQ) Process, named *Ph02*;

- Relieving Tempering, named *Ph03*;
- Spheroidizing annealing for the case of 100CrMo7, named *Ph04 (a)*;
- Carburizing for the case of 18NiCrMo5 and 20MnCr5, named *Ph04(b)*;
- Die Assisted Oil Quenching Process, named *Ph05*;

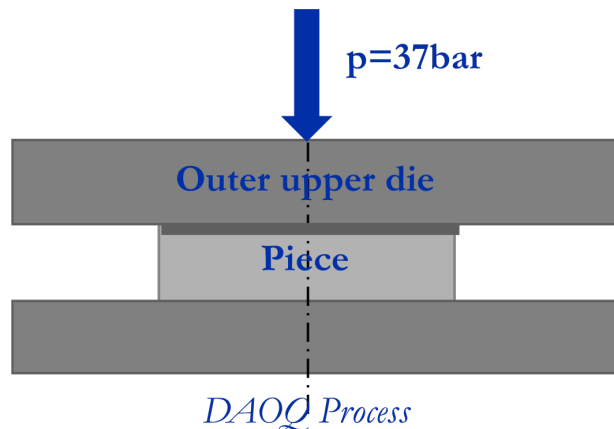


Figure 3.2: The DAOQ process conditions

- Relieving Tempering, named *Ph06*;

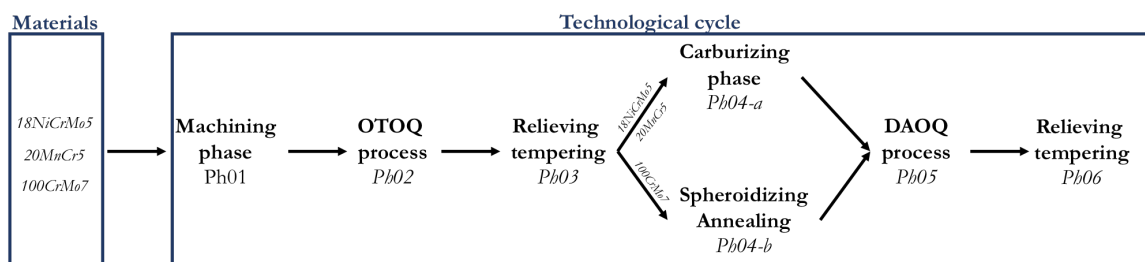


Figure 3.3: The manufacturing stage realised for the experimental activities

3.3 Metrological inspections

A specific methodology was implemented to define unique sample positions throughout the heat treatment operations. Scanning procedures were applied to standardise the experimental activities and limit errors. The components were treated on grates with narrow openings during all thermal operations excepted for the DAOQ process due to

the process equipment, as illustrated in Fig. 3.2. The reference plane of each sample was faced up. The replicable position was realised by a steel engraving that defined Plane 1, as illustrated in Fig. 3.5 (a). A string of information was contained in each signature, identifying the correct in-process placement as well as each sample throughout the experiments.



Figure 3.4: *The CMM machine utilised for the experimental investigations*

A Coordinate Measurement Machine (CMM) was adopted for the dimensional investigations. A unique measurement position was engineered using a tailored clamping system aided by two gauge blocks to turn the un-processed sample zones down, Fig. 3.5 (b). Other possible measurement configurations, such as mandrel fixing, were also tested and consequently rejected as complete measurements required two placements, which greatly reduced experimental accuracy. Each part was placed in the CMM working space as showed in Fig. 3.5. A reference notch realized by a gauge marker was applied to each component, corresponding to the outer diameter on both planes. The replicable position was determined by aligning the external reference marks to the clamping system while maintaining contact with the support structure that controlled the part rotation, Fig. 3.5. The measurement programmes were defined for each geometry, evaluating diameters, thicknesses and planarity tolerances as follows:

- *Inner and Outer Diameters:* five different scans were realised at different thicknesses through 3600 point samplings. Each measurement was expressed by means of an average value, plus/minus standard deviations generating a statistical representation of the collected data. The measurement paths are illustrated in Fig. 3.6.

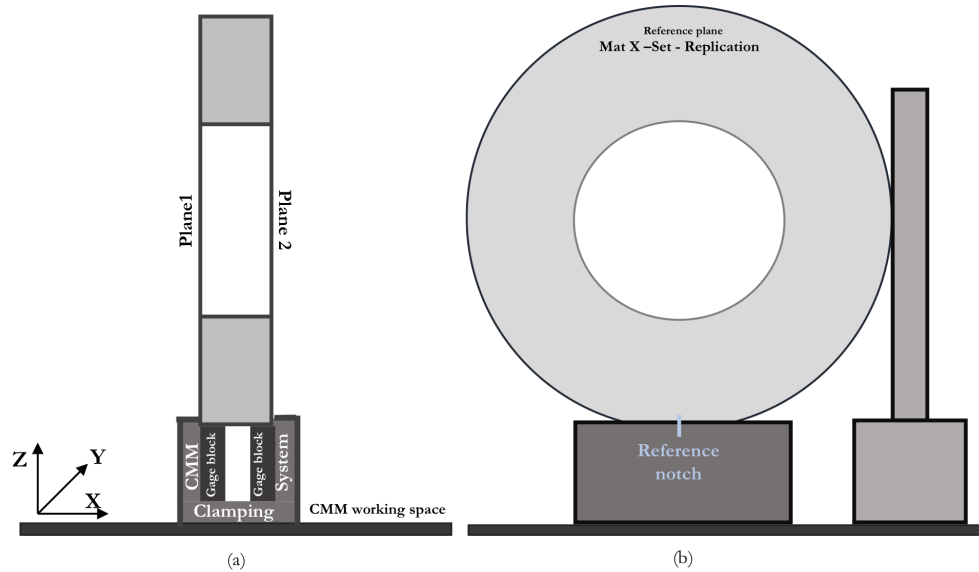


Figure 3.5: The sample measurement position utilised during the experiments

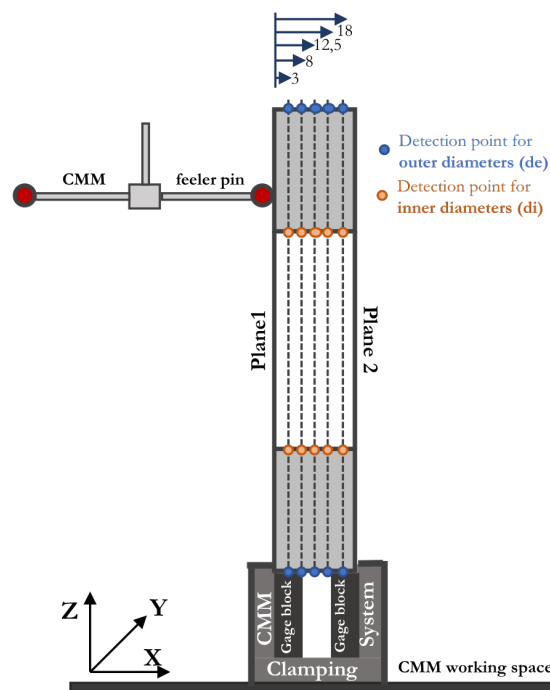


Figure 3.6: The strategy of the inner and outer diameters evaluations during the experimental campaign

- *Thickness*: each component was split into eight sections, cut in concentric circumferences at an angle of 45 degrees, Fig. 3.7(b). Detection points were obtained by the intersections among the angular sectors and the concentric circumferences, allowing for thickness assessments, Fig. 3.7 (b). These

assessments were obtained for each detection point by touching both sample planes at the same Y and Z coordinates, while changing X in order to measure the depth of the part, Fig. 3.7(a).

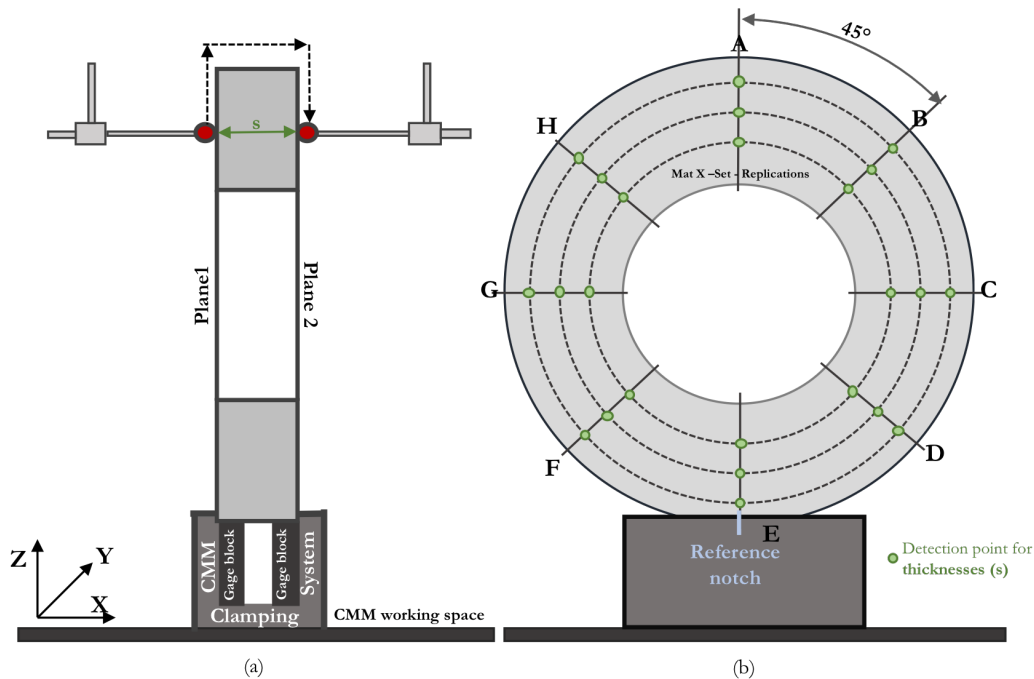


Figure 3.7: *The thickness determination: (a) the feeler pin movement; (b) detection points for the measurements*

- Planarity: the estimation was carried out by means of point samplings, taking an even number of concentric circumferences into account through the sample geometries, Fig. 3.8.

3.4 Analysis of the experimental data: An Overview

The collected data were managed through ANOVA analysis and realised for OTOQ and DAOQ to highlight deformation trends and to understand main effects and interactions of materials as well as geometries on the detected dimensions and tolerances. OTOQ and DAOQ were compared with the machining phase (Ph01) and pointing out the distortions through percentage variations. Materials were identified by five labels whereas the geometries were associate with the theoretical thermal modules M%. 18NiCrMo5 and 20MnCr5 were recognised by indicators "1", "2" after Ph02, while labels "4" "5" were

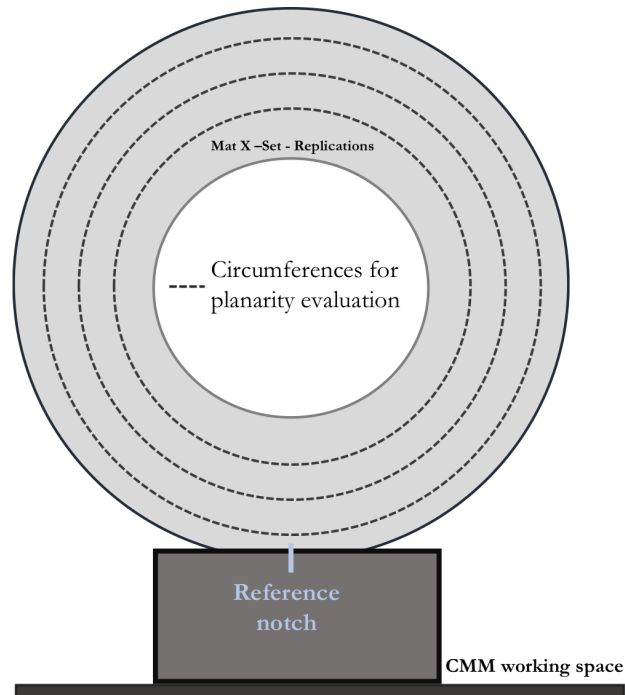


Figure 3.8: *The evaluation of planarity tolerance*

assigned to the same materials for Ph05 due to the changes of chemical compositions induced by Ph04-a. As a counterpart, 100CrMo7 was always referred to number "3". First of all, the volume variations were investigated and overall summarizing the effects of diameters and thicknesses alterations generated by Ph02 and Ph05. Afterwards, each dimension was deeply investigated in the following sections.

$$F\text{-value}_{\text{material}}=3,3$$

$$F\text{-value}_{\text{geometry}}= 2,7$$

$$F\text{-value}_{\text{interaction}}= 2,3$$

3.5 Volume

3.5.1 Determination of Volume Variations

The volume variations were evaluated by reconstructing each geometry through the measurements of the diameters and thicknesses, as described in par. 3.2. The data were compared with Ph01 as the reference point. The diameters and thicknesses of the samples were mainly modified by the technological operations. Each sample was rebuilt according to the detection points of the diameters and thicknesses. Compiling the experimental findings Fig. 3.6, Fig. 3.7, the volume changes were assessed throughout the thermal operations. The entire range of sample dimensions was included in this global indicator and all the dimensional changes induced by OTOQ and DAOQ were estimated.

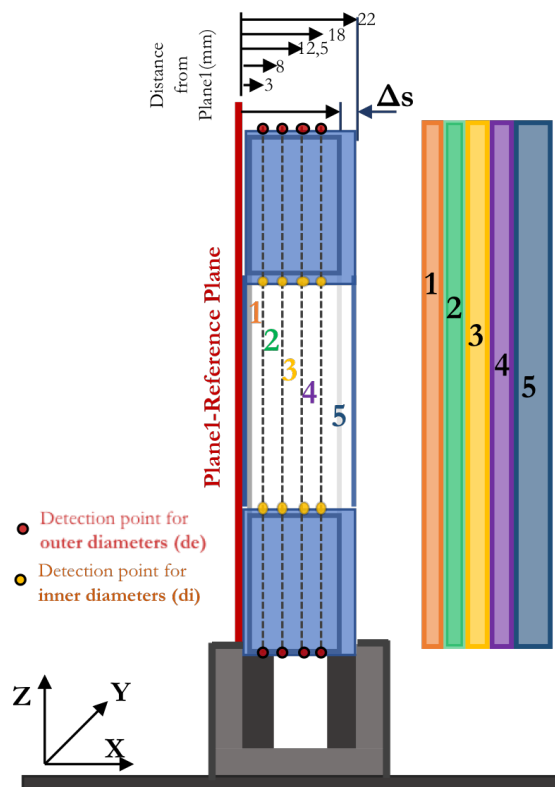


Figure 3.9: The calculated volume variations through the experimental measurements

The calculated volume variations were negligible, providing the same starting microstructures were maintained throughout the technological cycle. The significant volume variations were induced by the martensitic transformation. In fact, close-to-zero

variations were determined from Ph04-b in comparison with Ph01, indirectly validating the implied method for the volume variations evaluation. The same microstructures were detected from Ph04-b and Ph01 for 100CrMo7.

$$V_{\text{ring}} = \pi \frac{(d_e - d_i)^2}{4} s \quad (3.1)$$

Where:

d_i = inner diameter (mm)

d_e = outer diameter (mm)

s =thickness (mm)

The volume estimation regarding Ph01 was calculated by:

$$V_{\text{tot-ring}} = V_{\text{tot-ring1-Ph0x}} + V_{\text{tot-ring2-Ph0x}} + V_{\text{tot-ring3-Ph0x}} + V_{\text{tot-ring4-Ph0x}} + V_{\text{tot-ring5-Ph0x}}$$

$$\mathbf{V}_{\text{tot-ringPh01}} = \frac{\pi}{4} ((d_{e3\text{Ph01}} - d_{i3\text{Ph01}})^2 3 + (d_{e8\text{Ph01}} - d_{i8\text{Ph01}})^2 5 + (d_{e12,5\text{Ph01}} - d_{i12,5\text{Ph01}})^2 4,5 + (d_{e18\text{Ph01}} - d_{i18\text{Ph01}})^2 5,5 + (d_{e22\text{Ph01}} - d_{i22\text{Ph01}})^2 7)$$

Each step of the manufacturing cycle was characterised by the following volume variation estimation:

$$\mathbf{V}_{\text{tot-ringPh0x}} = \frac{\pi}{4} ((d_{e3\text{Ph0x}} - d_{i3\text{Ph0x}})^2 3 + (d_{e8\text{Ph0x}} - d_{i8\text{Ph0x}})^2 5 + (d_{e12,5\text{Ph0x}} - d_{i12,5\text{Ph0x}})^2 4,5 + (d_{e18\text{Ph0x}} - d_{i18\text{Ph0x}})^2 5,5 + (d_{e22\text{Ph0x}} - d_{i22\text{Ph0x}})^2 (7 + \Delta_{s\text{Ph0x}}))$$

Volume variations were derived from the comparison between each sub-volume by performing the consecutive operations:

$$\Delta V_{\text{tot-ringPh0x-Ph01}} = (V_{\text{tot-ring1-Ph0x}} - V_{\text{tot-ring1-Ph01}}) + (V_{\text{tot-ring2-Ph0x}} - V_{\text{tot-ring2-Ph01}}) + (V_{\text{tot-ring3-Ph0x}} - V_{\text{tot-ring3-Ph01}}) + (V_{\text{tot-ring4-Ph0x}} - V_{\text{tot-ring4-Ph01}}) + (V_{\text{tot-ring5-Ph0x}} - V_{\text{tot-ring5-Ph01}})$$

The formulae reported above bring clarity to Fig. 3.9.

3.5.2 OTOQ-Volume variations

Fig. 3.10 displays the experimental findings regarding the volume variations after Ph02 for the whole materials and geometries in terms of means values and standard deviations. The OTOQ technological stage induced an enlargement of each geometrical characteristic leading to positive volume variations. In particular, for high carbon alloyed steel the specimen modifications are bigger than the carburising steels due to carbon percentages equal to 0,18% and 0,20% instead of 1%. Thus, lower volume variations, induced by martensitic transformation, can be expected and resulting in lower distortion magnitudes, F.ig. 3.10

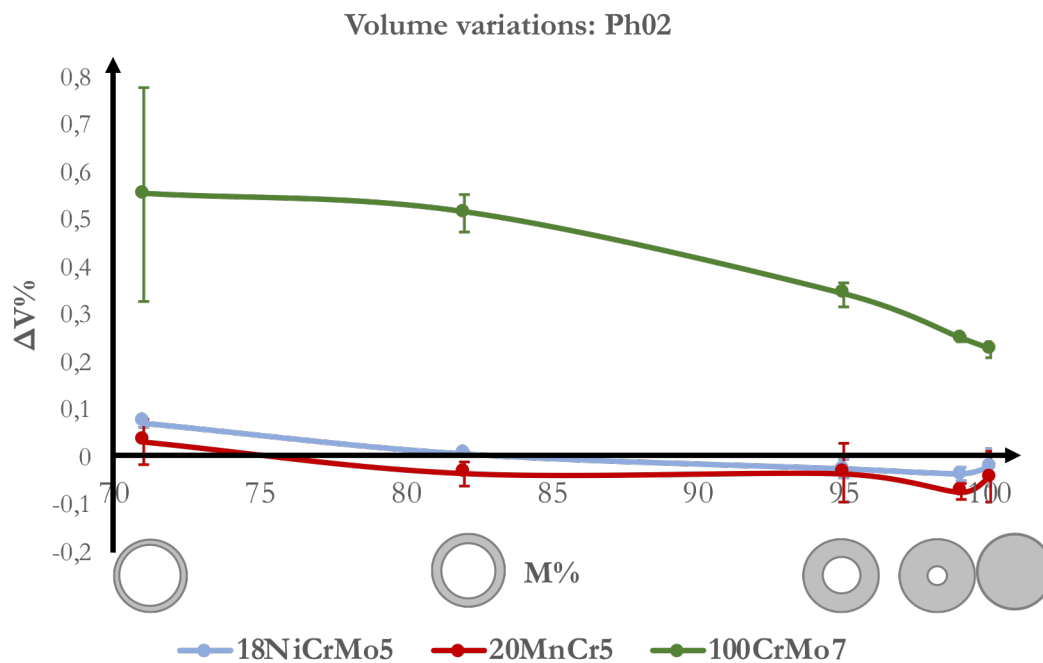


Figure 3.10: Volume variations induced by Ph02

Positive variations were determined for 100CrMo7. A trend can also be visible coming through the geometries and particularly decreasing the thermal module, the green line in Fig. 3.10.

The volume variations are minute for the carburising materials, while the variations are shown an order of magnitude equal to a tenth of volume percentages that increase when the theoretical thermal modules decrease for the case of 100CrMo7, Fig. 3.10.

Considering the standard deviations, an higher variability of volume variations can be visible for Set E linked to the thinnest transversal section.

An investigation regarding the F-values was also conducted by means of the ANOVA technique in order to point out the effect of materials and geometries on the volume variations. Coming through F-Values, materials ($F\text{-value}_{\text{material}}=179$), geometries ($F\text{-value}_{\text{material}}=11,3$) and finally the interaction ($F\text{-value}_{\text{interaction}}=1,41$) were shown decreasing influences on the process outcomes.

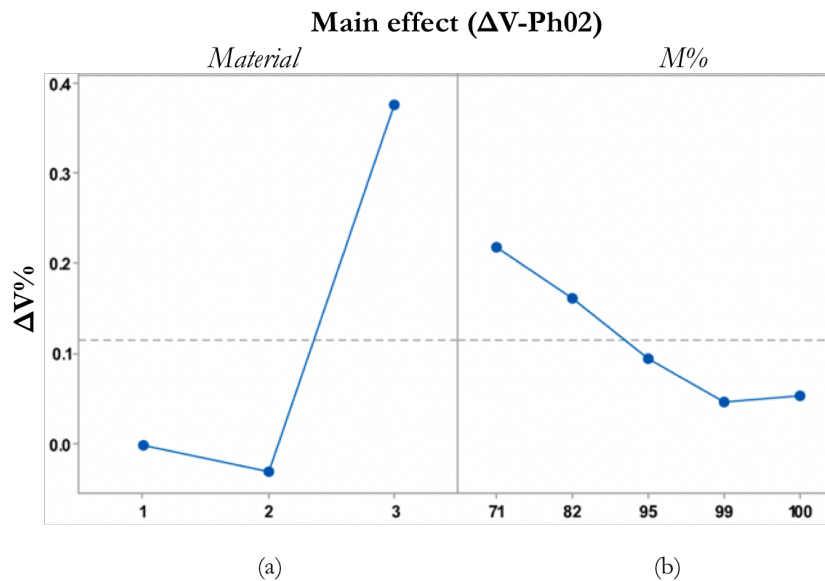


Figure 3.11: *The ANOVA main effects concerning (a) materials and (b) geometries of the volume variations induced by Ph02*

The ANOVA results are illustrated in Fig. 3.11 and Fig. 3.12. Close to zero volume variations are pointed out for materials "1" and "2" due to the absence of previous carburising, Fig. 3.11 (a). The material microstructures were characterised by starting carbon percentages (0,18%C for 18NiCrMo5 and 0,2%C for 20MnCr5) and thus, resulting in less-distorted martensite microstructures in comparison with material "3" that was identified by 1% of carbon percentage, as reported in Tab. 1.3.

Higher volume variations were induced by more rapid cooling conditions that were considered by the theoretical thermal modules. An enhancement in volume variations were obtained coming across the disc (M=100%) to the thinnest ring (M=71%), as shown in Fig. 3.11 (b). Any relevant variations were addressed to the combined effect of materials and geometries for the whole carburising samples whereas a typical trend was identified for the hardening material. An increase in volume changes was detected by decreasing the theoretical thermal module, or in other word accelerating the cooling

phase. This is observable in Fig. 3.12.

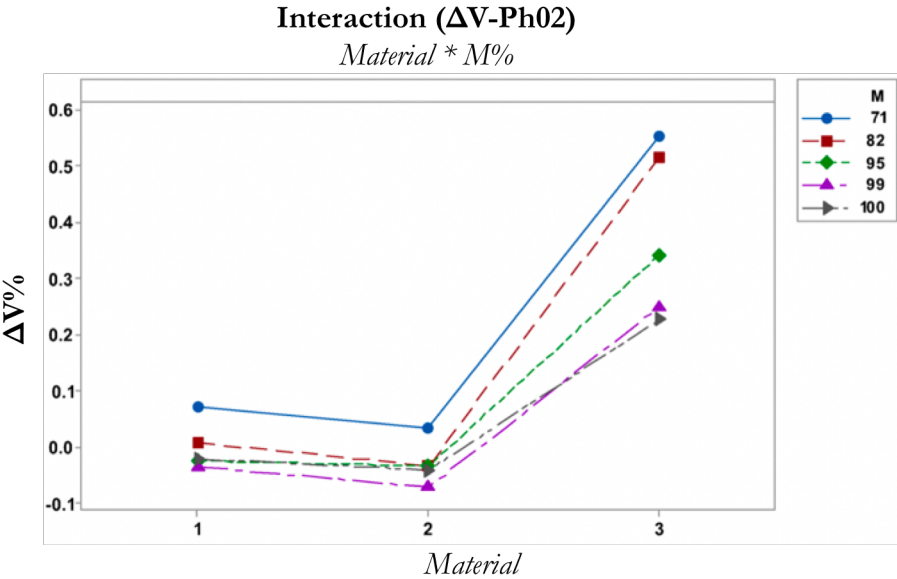


Figure 3.12: The ANOVA interaction regarding the volume variations induced by Ph02

3.5.3 DAOQ-Volume variations

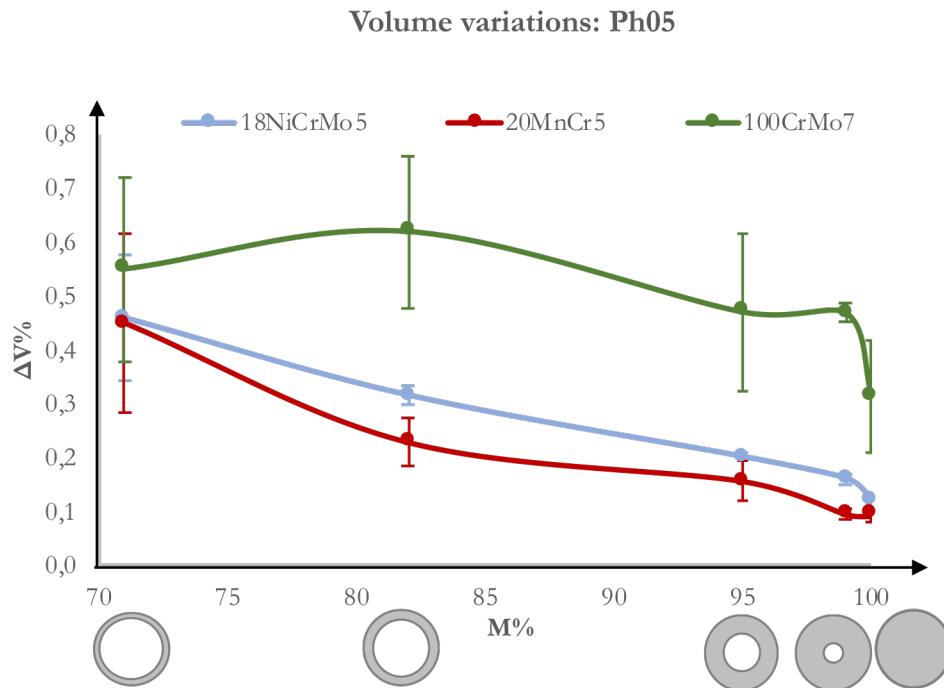


Figure 3.13: Volume variations induced by Ph05

Fig. 3.13 illustrates the volume variations caused by DAOQ, examining all the materials and geometries in terms of mean values and standard deviations. In this case, as opposed to Ph02, major volume changes were determined not only for the hardening steel but also for the carburising materials due to a previous enrichment in carbon percentage induced by Ph04-a, as illustrated in Fig. 3.3.

The carburising materials display comparable trends and for 18NiCrMo5 a quasi-linear behaviour was identified. Overlapping values were estimated for 18NiCrMo5 and 20MnCr5 - Set A and Set E (red and blue lines in Fig. 3.13). A standardization of the quenching outcomes for the carburising materials was also evidenced due to the same treated components, carburising depths and final carbon percentages. The bearing ring steel revealed different levels of volume variations depending on the theoretical thermal module. The lowest variation was determined for Set A, while comparable alterations were obtained for Set D and Set E as well as for Set B and Set C. This is reported in Fig. 3.13.

An ANOVA analysis was also conducted. It is notable that each factor had a significant influence on the volume variations. The material effect was not as influential

as the geometry, yielding a lower F-Value ($F\text{-Value}_{\text{material}}=16,2$ and $F\text{-value}_{\text{geometry}}=39,9$). Fig. 3.14 shows that volume variations decrease from Material 3 to Material 5 as well as from $M\%=71$ to $M\%=100$.

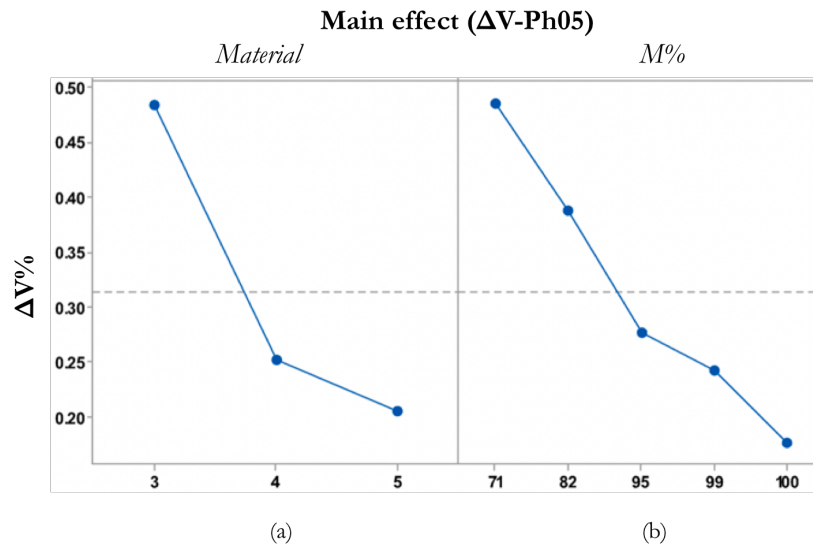


Figure 3.14: The ANOVA main effects concerning (a) materials and (b) geometries of the volume variations induced by Ph05

Any significant changes were attributed to the interaction between the investigated factors. A more rapid cooling can be achieved decreasing the theoretical thermal modules, and by combining geometries with increasing carbon percentages, higher volume variations can be produced through the martensitic transformation. This is shown in Fig. 3.15.

3.5.4 Conclusion concerning volume variations

High volume variations were recorded for 100CrMo7 for both quenching processes due to martensitic microstructures characterized by a carbon percentage equal to 1%.

Fig. 3.16 documents the differences between Ph02 and Ph05 for 100CrMo7. A more effective martensitic transformation was assessed after DAOQ and Ph05 produced major volume variations in comparison with Ph02, especially for the heavier geometries (Set A, Set B and Set C). The highest volume variations were registered for Set D and Set E, resulting in the most shape distortions following Ph05. This is illustrated in Fig. 3.16.

Volume modifications were negligible in 18NiCrMo5 and 20MnCr5 after Ph02 due

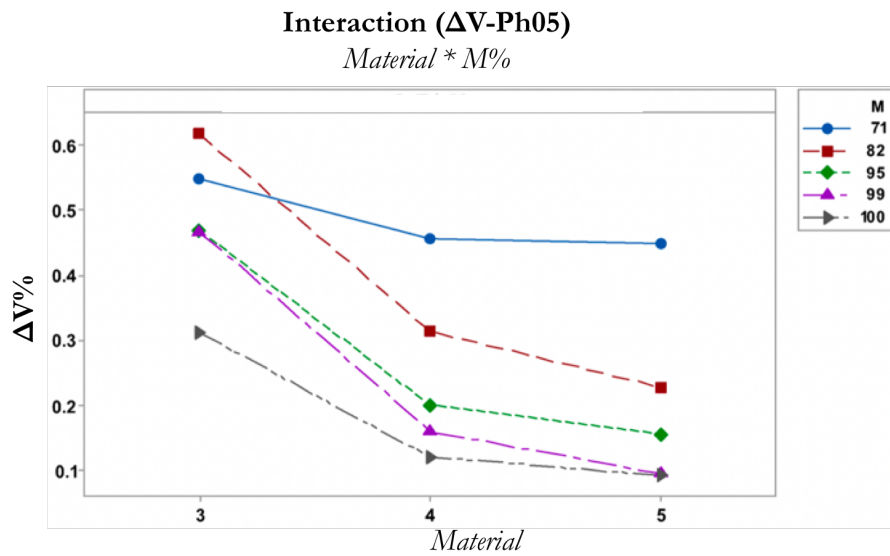


Figure 3.15: The ANOVA interaction regarding the volume variations induced by Ph05

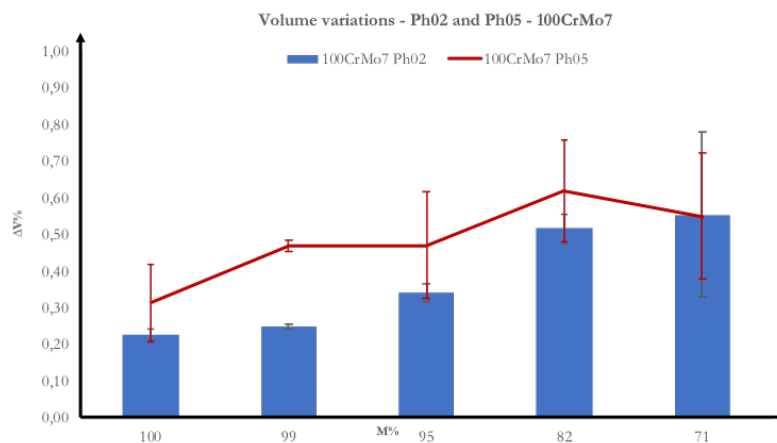


Figure 3.16: Direct comparison among volume variations induced by Ph02 and Ph05 for the case of 100CrMo7

to the absence of the carburising stage. The obtained martensite was identified as having carbon percentages equal to 0,18% and 0,20% respectively; rather than 0,8%, the usual requirement for carburising materials. Therefore, the absence of the carburising phase decreases the volume variations. The variations increase with the addition of the carburising stage produced overlapping trends for both considered materials from Set A to Set E. This is illustrated in Fig. 3.17 and Fig. 3.18.

Volume variations represent macroscopic indicators regarding how geometries deform throughout quenching processes. These variations were calculated through experimental estimations of diameters and thicknesses and the following paragraphs will look closely

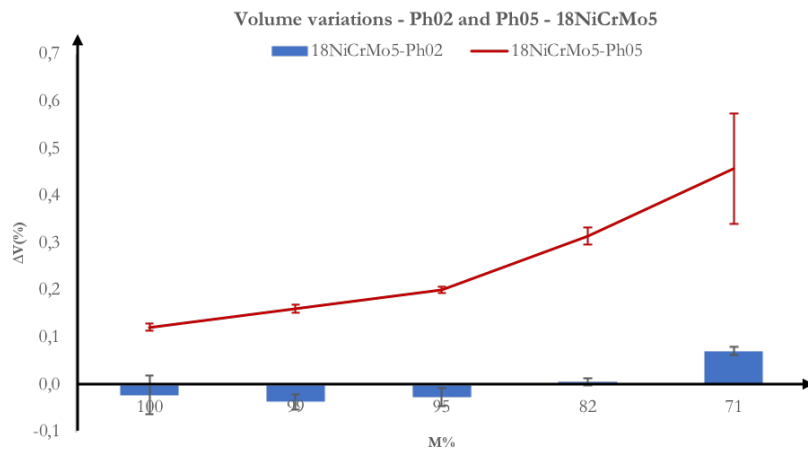


Figure 3.17: Direct comparison among volume variations induced by Ph02 and Ph05 for the case of 18NiCrMo5

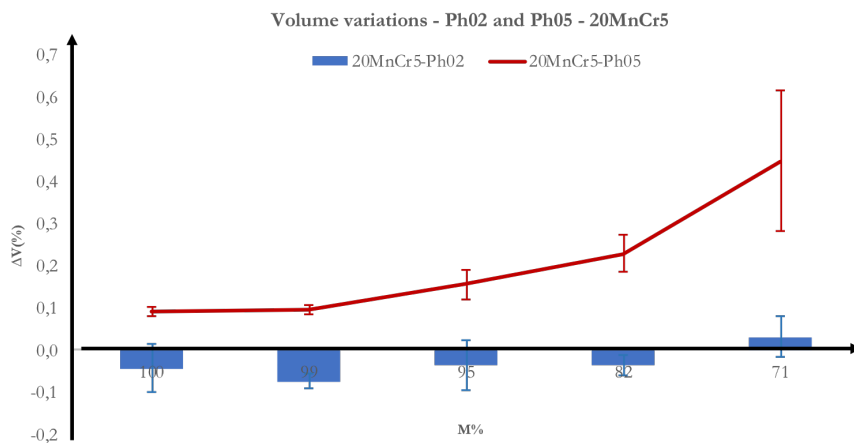


Figure 3.18: Direct comparison among volume variations induced by Ph02 and Ph05 for the case of 20MnCr5

at the variations in these dimensions for OTOQ and DAOQ.

3.6 Inner Diameter

As discussed, quenching processes typically modify the design of treated parts, particularly affecting shapes and dimensions. In this phase, a deep analysis regarding inner diameter modifications was conducted, considering both the OTOQ and DAOQ processes. Firstly the ANOVA technique was utilised for analysing what effects material

and geometry have on the inner diameter deformations induced by Ph02 and Ph05. The variations were compared with Ph01 except for the final conclusions that were drawn by selecting both quenching operations from the previous manufacturing step. Hence, Ph01 was compared with Ph02, and Ph04 with Ph05, Fig. 3.3.

3.6.1 OTOQ-Inner diameter variations

The variations of inner diameter regarding the whole set of samples are displayed in Fig. 3.19. A negative deformation was detected for Set B of the hardening steel; whereas decreasing the transversal sections of the samples, turned the variations into positive values, reaching the maximum evaluation for Set D. This is visible in Fig. 3.19. 18NiCrMo5 and 20 MnCr5 show the same deformation trends, reaching the maximum for Set B. The geometrical variations also decreased from Set B to Set E, showing minute differences. Increasing M% produced the highest values of deformations for geometry B (blue and red lines in Fig. 3.19).

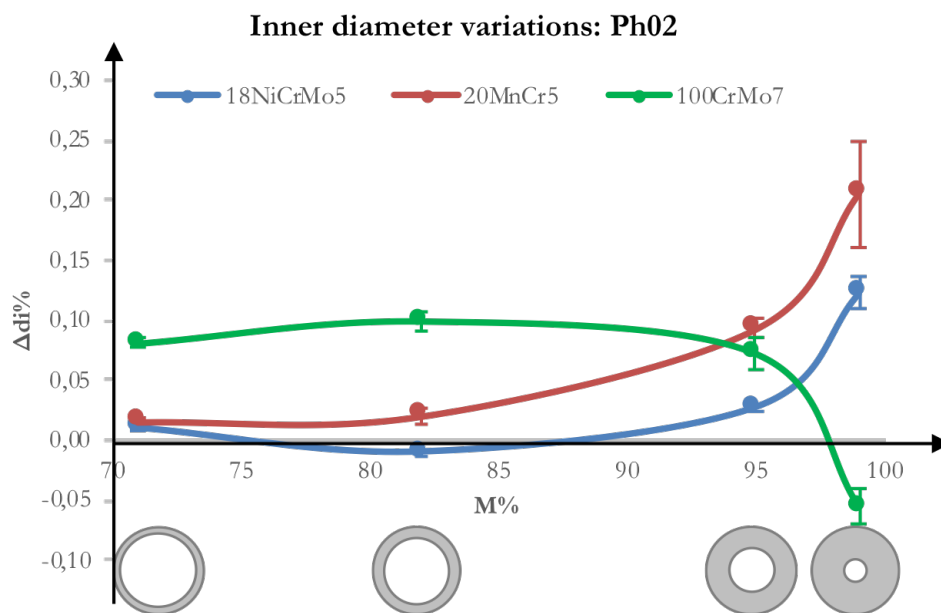


Figure 3.19: Inner diameter variations induced by Ph02

The ANOVA investigation evaluated not only the influence of the material selection (F-Value=30,1) and M% (F-Value=27,4) but also the interaction, which played a fundamental role in obtaining the maximum F-Value, 93,1. Fig. 3.20 keeps account of the main effects of M% and materials on the dimensional modifications of the inner

diameters.

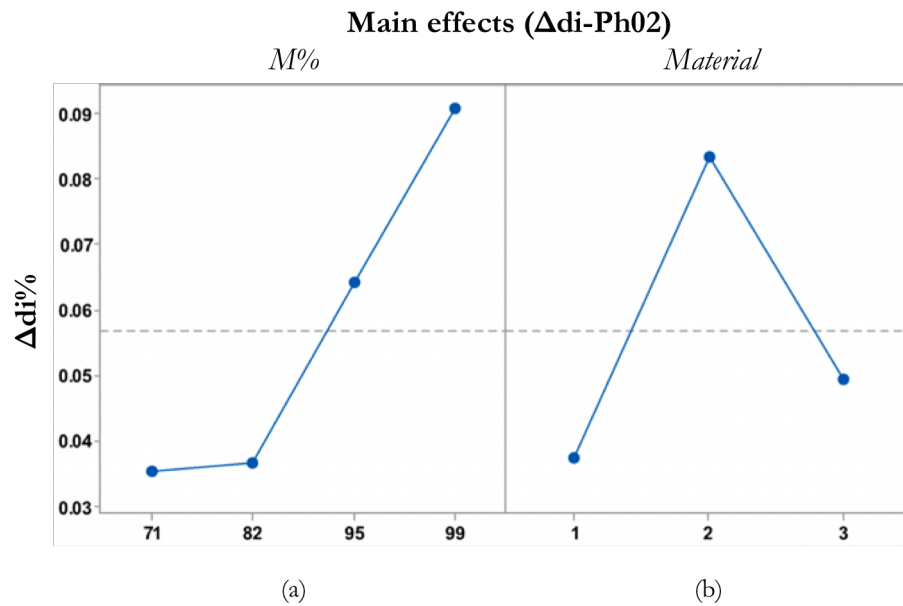


Figure 3.20: The ANOVA main effects concerning (a) materials and (b) geometries of the inner diameter variations induced by Ph02

The deformations noticeably augmented when increasing the virtual thermal modules (Fig. 3.20 a) whereas a trend which go up and down is induced by the materials Fig. 3.20 (b). 18NiCrMo5 had the lowest level of overall deformations and 100CrMo7 presented more relevant inner diameter distortions than 20MnCr5, Fig. 3.20 (b). An inner diameter enhancement is seen when decreasing the theoretical thermal module for 100CrMo7, whereas an inverse effect is reported for the carburising materials, Fig. 3.21.

3.6.2 DAOQ-Inner diameter variations

Fig. 3.22 displays the inner diameter variations with the entire set of geometries and materials. The variations of 100CrMo7 are always negative and increase from Set B to Set E, showing also restricted standard deviations. 18NiCrMo5 and 20MnCr5 show positive changes and show the same trends and an overlapped maximum value - blue and red lines in Fig. 3.22.

These different trends can be attributed to the comparison between Ph05 and Ph01, although several important issues could be overlooked if previous manufacturing operations are not also considered. Fig. 3.23 displays inner diameter changes compared

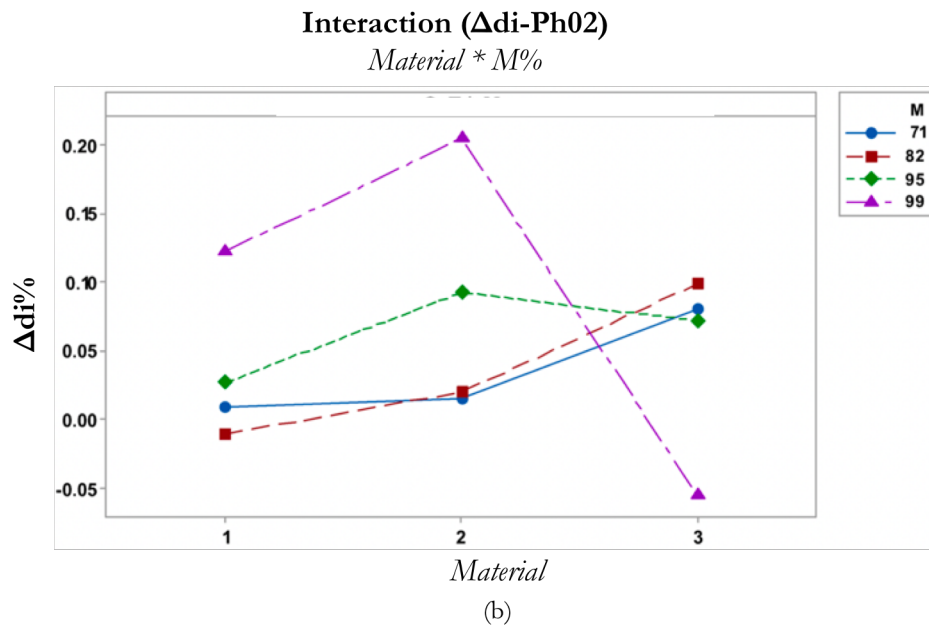


Figure 3.21: The ANOVA interaction regarding the inner diameter variations induced by Ph02

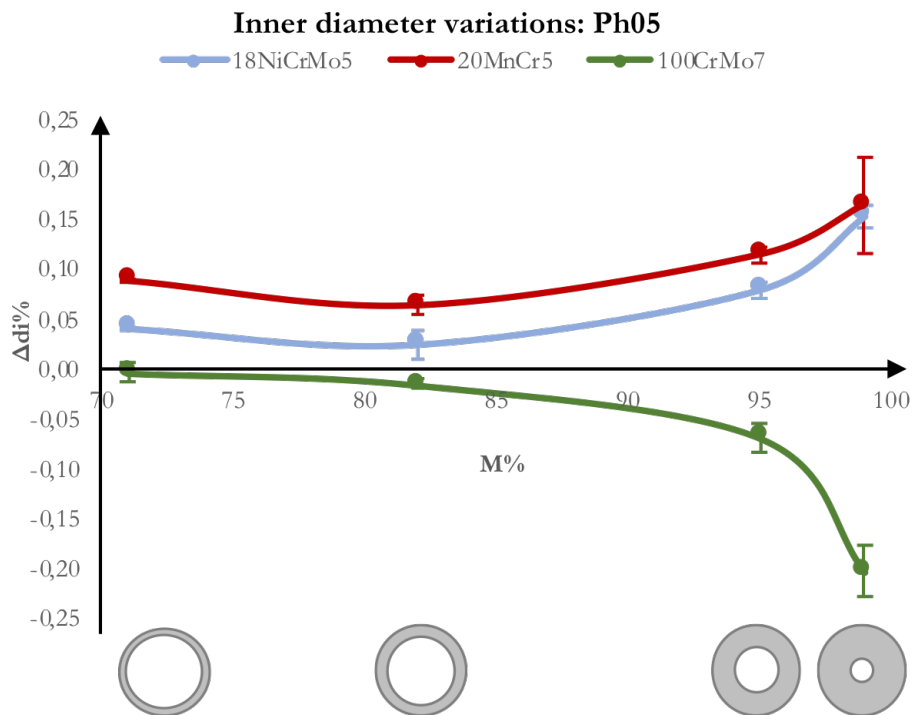


Figure 3.22: Inner diameter variations induced by Ph05

with Ph04 (either a or b depending on investigated materials, Fig. 3.3).

The deformations are always positive, showing similar tendencies that are based neither on the materials nor the geometries and thus illustrating the replicable effect of the press and the mould on the treated parts. Regarded through the ANOVA analysis, these effects

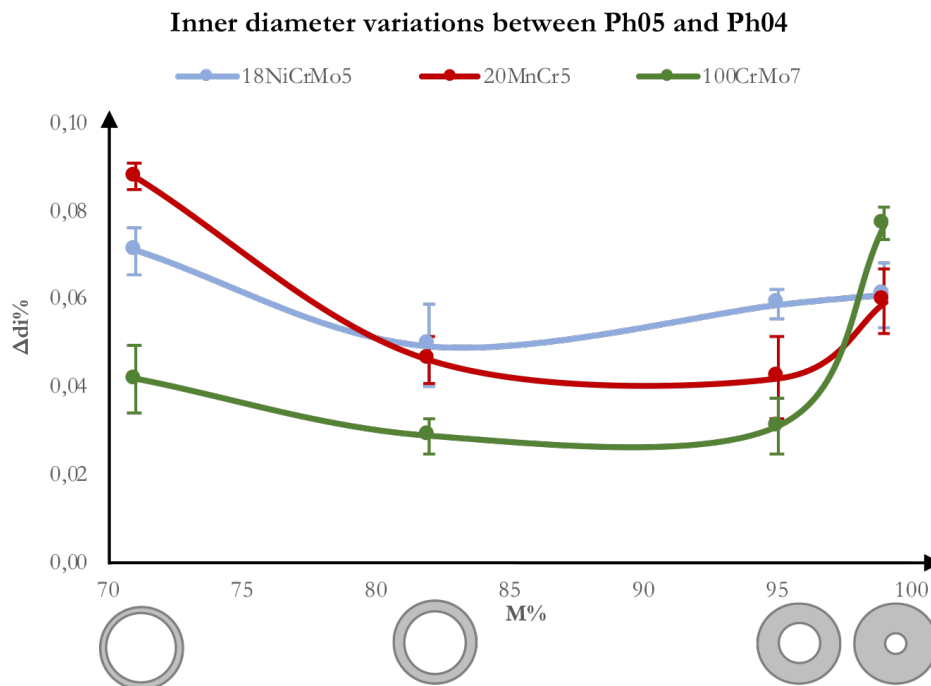


Figure 3.23: Inner diameter variations induced by Ph05 compared with Ph04

are more noticeable; restricted variations of inner diameters were revealed for all geometries with 1.84 as F-Value, Fig. 3.24 (b).

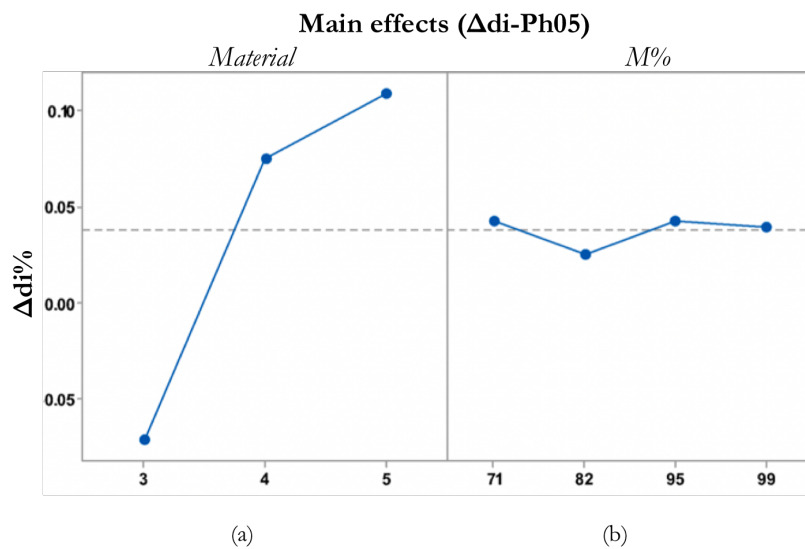


Figure 3.24: The ANOVA main effects concerning (a) materials and (b) geometries of the inner diameter variations induced by Ph05

A significant influence was evaluated for the materials with an F-Value equal to 330,7. Fig. 3.24 (a) portrays the modifications that increase from Material 3 to Material 5.

Significant differences were also attributed to the interaction. The inner diameter variations increased from material 3 to material 5 showing a range of trends dependent on the geometries.

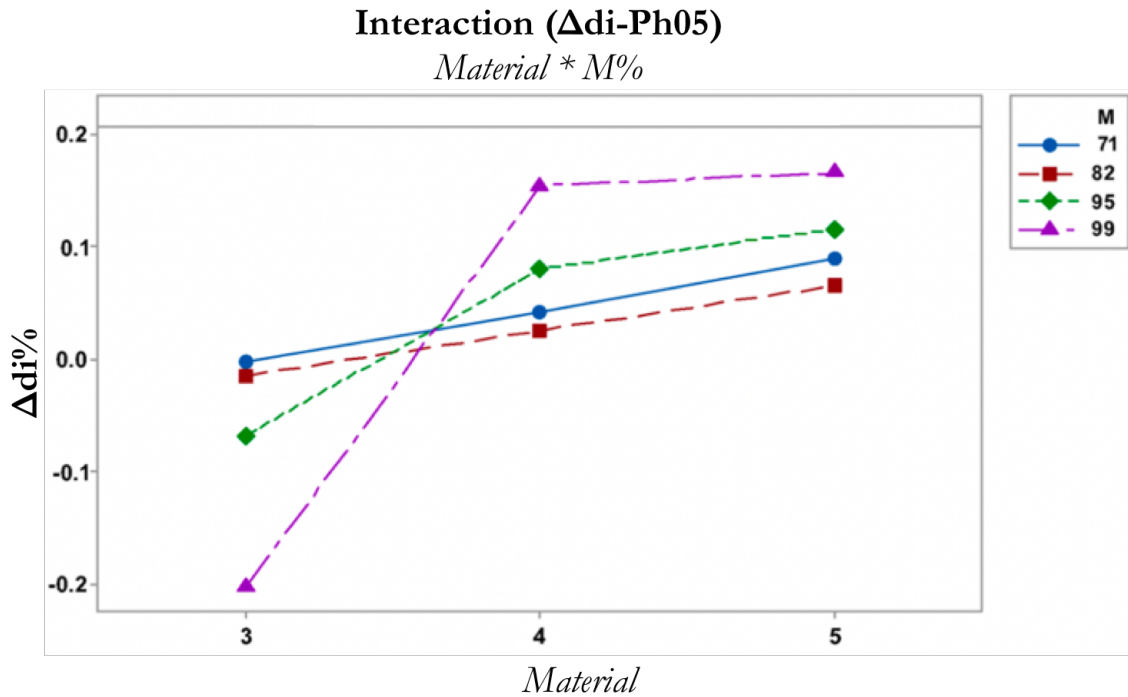


Figure 3.25: The ANOVA interaction regarding the inner diameter variations induced by Ph05

3.6.3 Conclusion regarding inner diameter variations

The inner diameter variations were affected by both Ph05 and Ph02 as well as by the materials and geometries, revealing a range of different trends of impact on the outcomes. The following graphs directly compare the differences induced by Ph02 and Ph05 (matched against Ph04) and clearly point out the higher level of control in terms of diameter modifications achieved by Ph05. Fig. 3.26 overlaps the variations of 100CrMo7 for both quenching processes.

Set B was characterised by a negative variation after Ph02, which then transformed into a positive one after Ph05 and actually produced the maximum distortions. A levelling of distortions was derived from DAOQ process across Set C to Set E; while OTOQ obtained major distortions as well as standard deviations in comparison with Ph05. This is visible in Fig. 3.26.

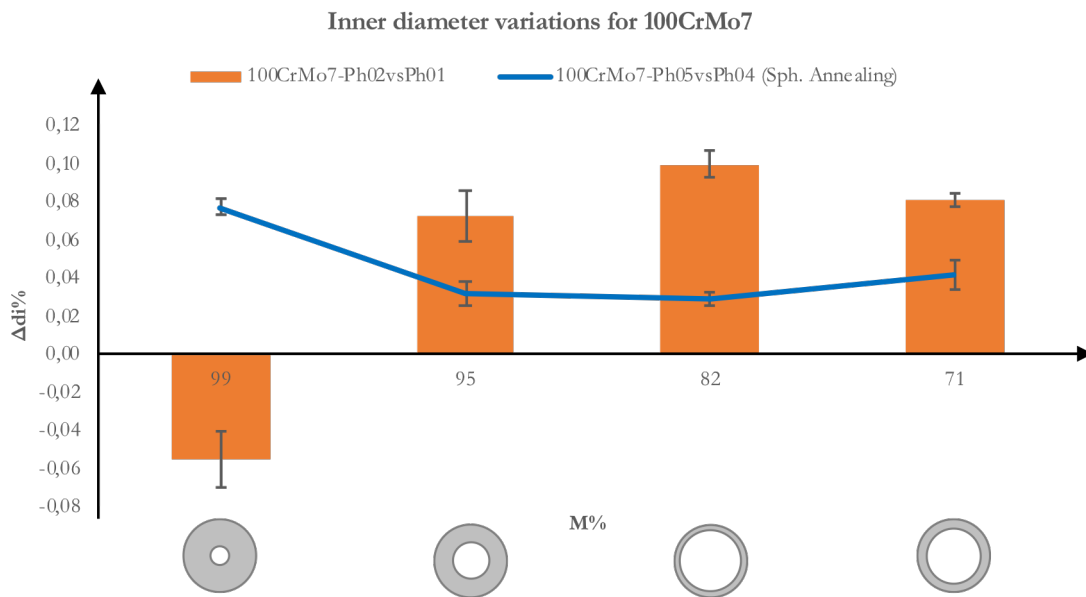


Figure 3.26: Inner diameter variations induced by Ph02 and Ph05 for 100CrMo7

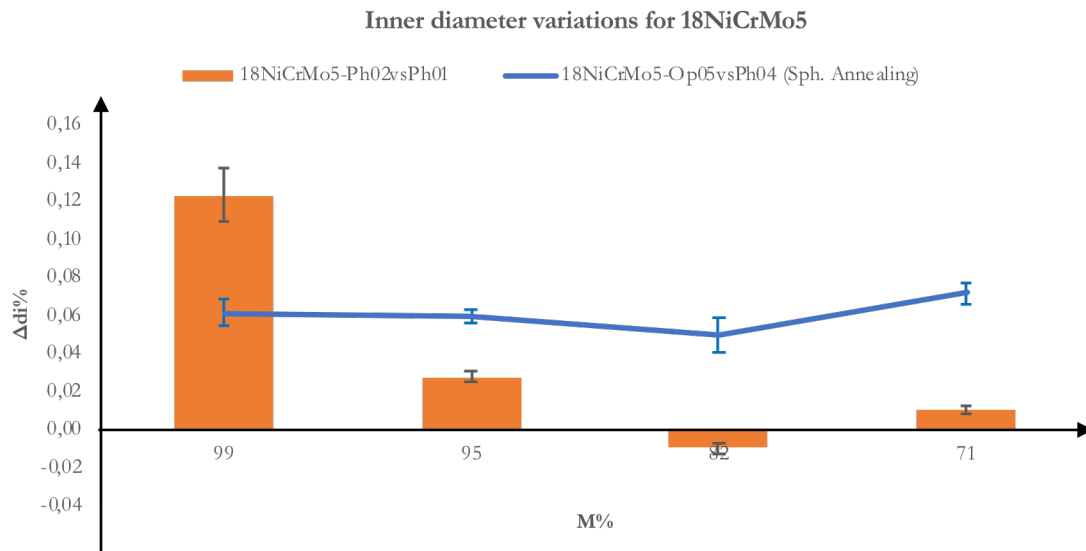


Figure 3.27: Inner diameter variations induced by Ph02 and Ph05 for 18NiCrMo5

Fig. 3.27 and Fig. 3.28 show the minute variations for both carburising materials expected for Sets B. These negligible deformations are linked and attributed to the martensitic microstructures, constituted by the initial carbon percentages 0,18%C and 0,20%C. A standardization of the inner diameter deformations can be observed for 18NiCrMo5 and 20MnCr5 after Ph05. Similar deformations were determined across the entire range of experimental samples, as reported in Fig. 3.27 and Fig. 3.28.

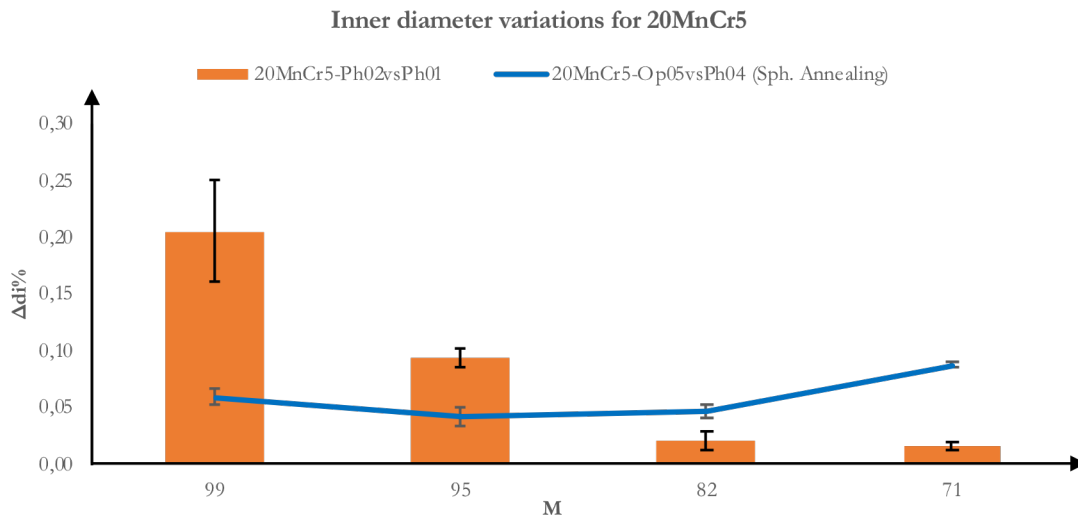


Figure 3.28: Inner diameter variations induced by Ph02 and Ph05 for 20MnCr5

3.7 Outer Diameter

An investigation regarding the outer diameter modifications was conducted in order to individuate the effects of OTOQ and DAOQ on this dimension. The experimental findings were reported through mean values and standard deviations and aided by the ANOVA analysis.

3.7.1 OTOQ-Outer diameter variations

Fig. 3.29 portrays the variation of outer diameters for all the samples following Ph02. The outer diameters changes were all positive and they increased when the transversal sections for 100CrMo7 were decreased. Similar variations were identified for Set A and Set B, magnitude enhancements were determined for Set B to Set D and a decreasing trend was obtained from Set D to Set E, as illustrated in Fig. 3.29. Carburising materials produced close to zero changes due to the absence of the carburising phase prior to Ph02. In fact, higher carbon percentages led to higher deformations, as shown by Fig. 3.29.

The most relevant influence was attributed to the material effect (F-Value=326,4), followed by the interaction (M*Material, F-Value=13,9) and finally by the geometry (M%, F-Value=9,9). The material impact is clearly portrayed in Fig. 3.30(a), while no identifiable trends can be drawn for the geometrical factor due to minute alterations, Fig.

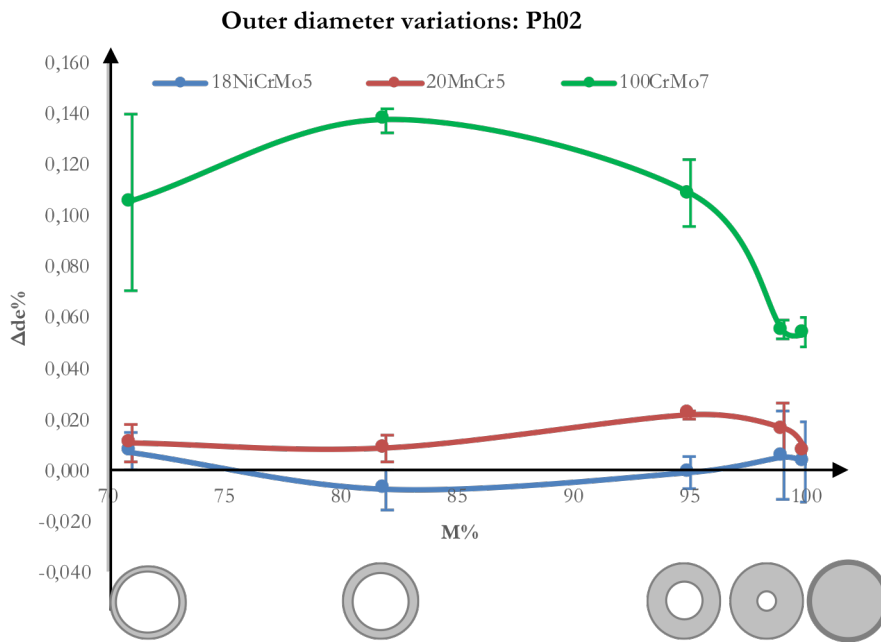


Figure 3.29: Outer diameter variations induced by Ph02

3.30 (b). The interaction displays notable increments of deformations from material 1 to Material 3 along with a decreasing in the theoretical thermal modules, Fig. 3.31.

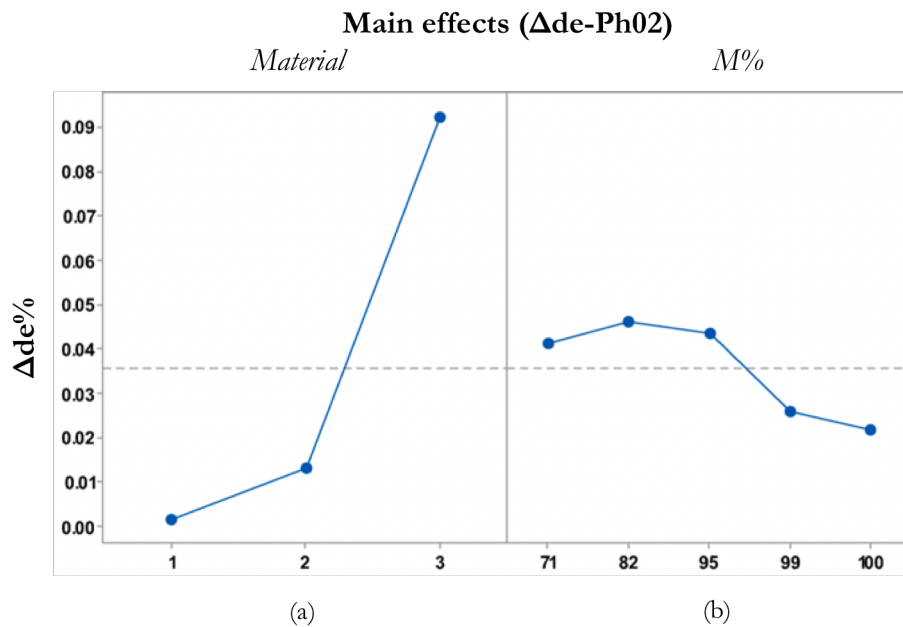


Figure 3.30: The ANOVA main effects concerning (a) materials and (b) geometries of the outer diameter variations induced by Ph02

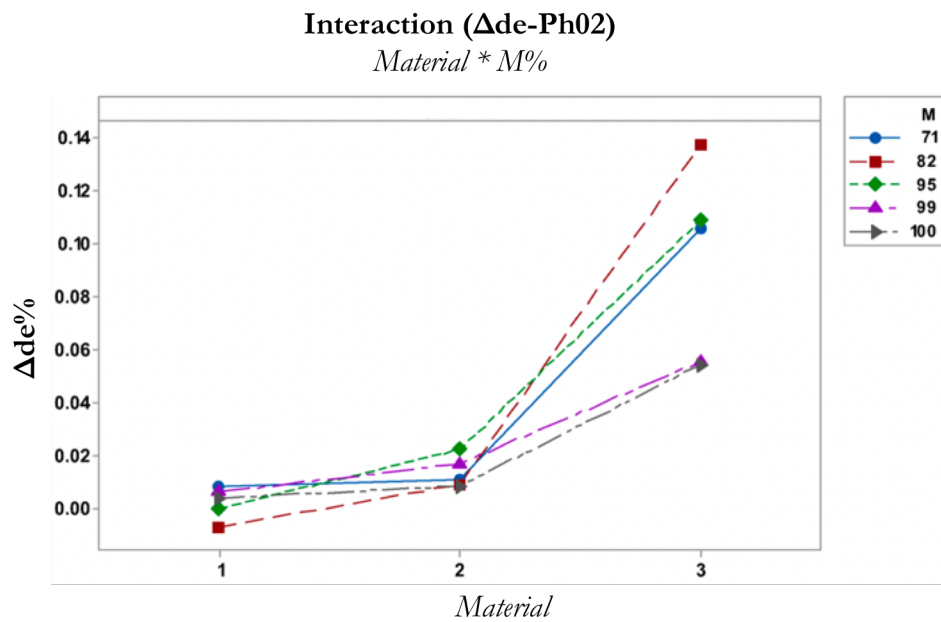


Figure 3.31: The ANOVA interaction regarding the outer diameter variations induced by Ph02

3.7.2 DAOQ-Outer diameter variations

Fig. 3.32 illustrates the dimensional variations of outer diameters after Ph05, reporting the experimental measurements for all the materials and geometries. Regarding the carburizing materials, comparable deformation trends were obtained from Set A to Set C – depicted by the red and blue lines in Fig. 3.32; whereas higher distortions were evaluated for 100CrMo7. Increasing variations were detected from Set C to Set E for 18NiCrMo5 and 20MnCr5, while a reduction was noted for the hardening steel when selecting the same geometries. In summary, different trends of the outer diameter were observed, depending not only on the geometries of the treated parts but also on the materials.

The ANOVA analysis was carried out, reporting any significant outer diameters variations induced by both materials (F-value=0,7) or geometries (F-value=1,0), Fig. 3.33. The interaction was characterised by an F-Value equal to 10.9 and thus, a relevant impact could be assessed on the investigated dimensions. Fig. 3.34 depicts this interaction, illustrating the differences through each theoretical thermal module. Quasi-linear trends can be observed for Set E across the materials, reaching the maximum value for Material 5. Decreasing behaviour was detected from Sets A to C as

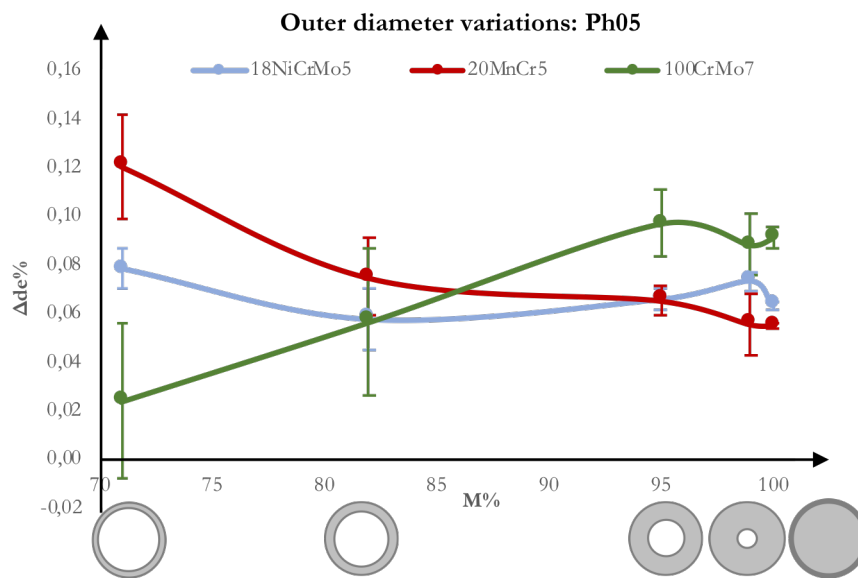


Figure 3.32: Outer diameter variations induced by Ph05

well as from materials 3 to 5. A levelling trend was observed for Set D throughout the carburising materials, whereas an enhancement was evaluated between 20MnCr5 and 100CrMo7 for the same geometries.

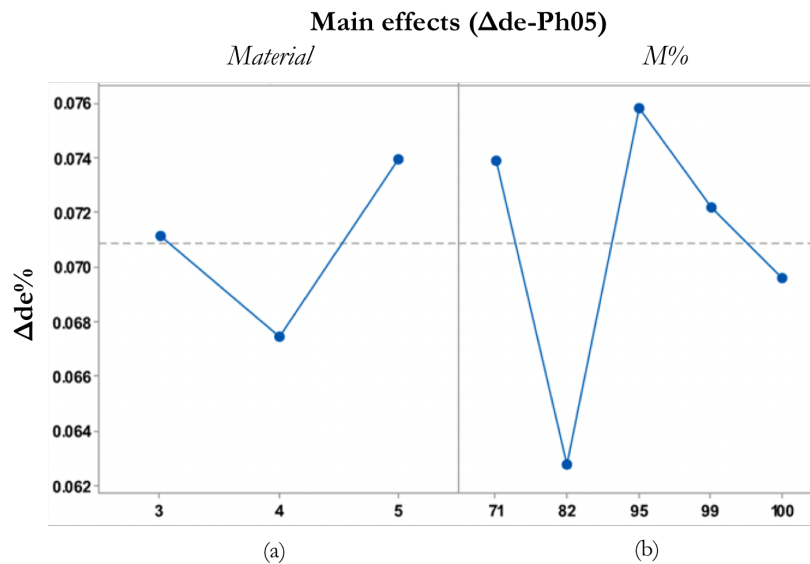


Figure 3.33: The ANOVA main effects concerning (a) materials and (b) geometries of the outer diameter variations induced by Ph05

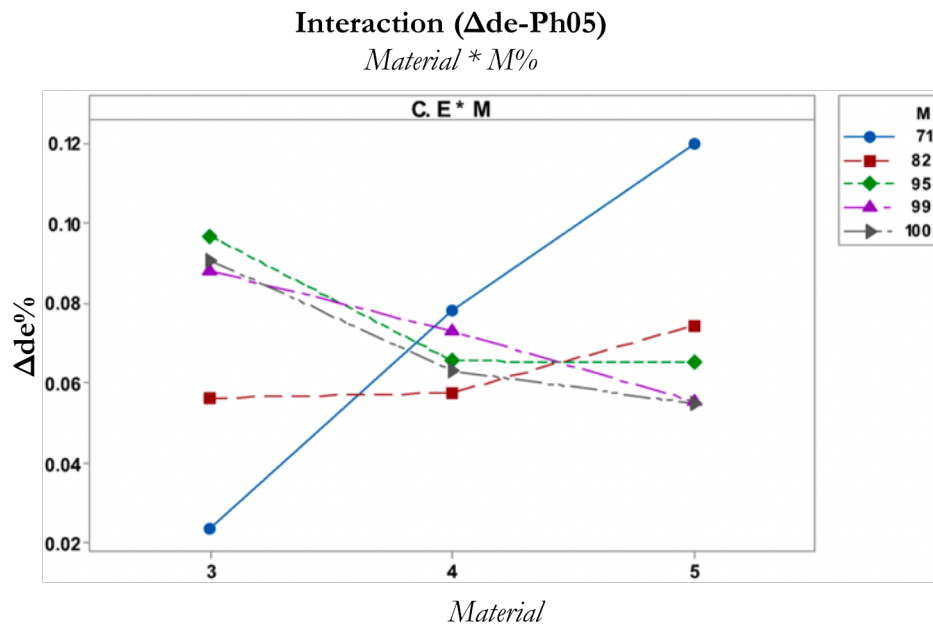


Figure 3.34: The ANOVA interaction regarding the outer diameter variations induced by Ph05

3.7.3 Conclusion regarding outer diameter variations

A comparison between Ph02 and Ph05 for each material showing the outer diameter variations is summarised in Fig. 3.35, Fig. 3.36 and Fig. 3.37. Increasing variations are seen in the bearing ring steel (100CrMo7) from Set A to Set D after Ph02, whereas a decreasing trend is observable from Set D to Set E. The highest standard deviation is in Set E, orange bars in Fig. 3.35. Comparable distortion magnitudes are evident for Set A to Set B in terms of means values as well as standard deviations. After decreasing the theoretical thermal module, an enhancement was visible from Set B to Set D and a plateau from Set D to Set E, the blue line in Fig. 3.35. To summarise, Set A and Set B showed major deformations after Ph05 as opposed to Set D and Set E in the case of Ph02, while Set C revealed comparable values of outer diameter variations for both quenching processes.

Minute variations were induced by Ph02 for the carburising materials due to martensitic microstructures respectively characterised by 0.18%C and 0.20%C, orange bars in Fig. 3.36 and Fig. 3.37. Close outer diameter distortions were also evidenced for 18NiCrMo5 (0.06-0.08 percentage variations), blue line in Fig. 3.36. 20MnCr5 showed linear enhancement from Set A to Set D subsequently followed by a changing in the gradient

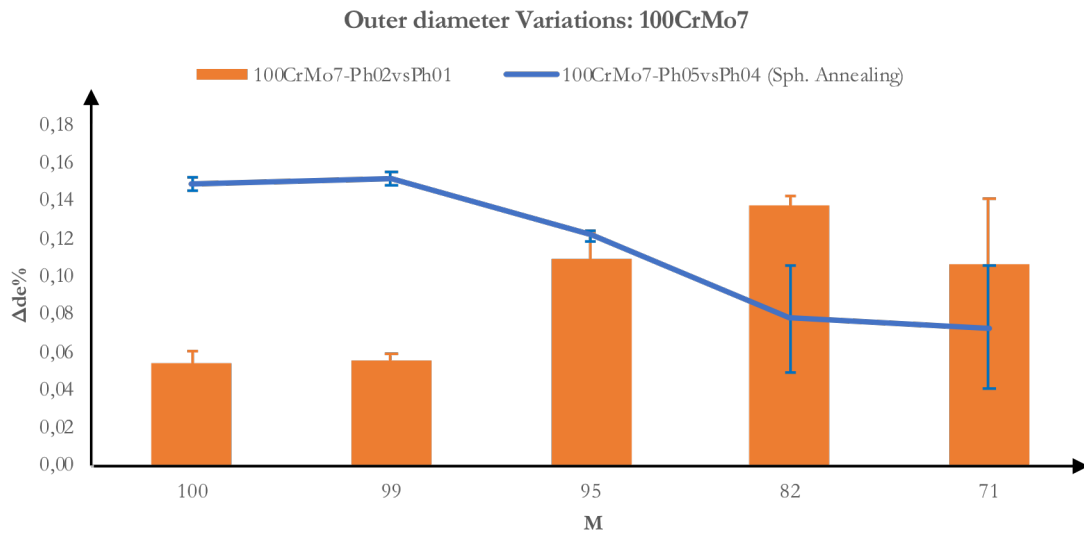


Figure 3.35: Outer diameter variations induced by Ph02 and Ph05 for 100CrMo7

from Set D to Set E (blue line in Fig. 3.37).

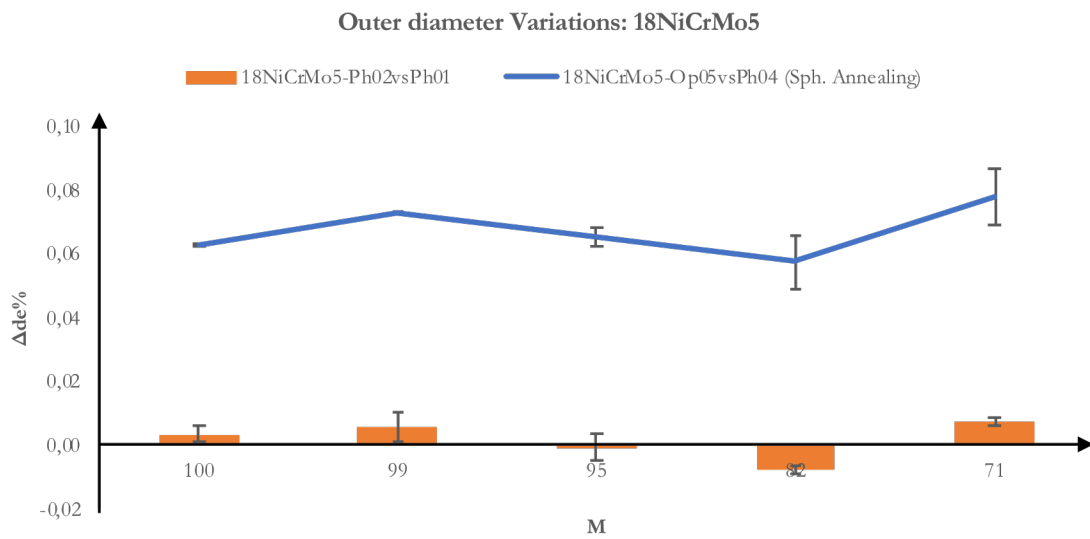


Figure 3.36: Outer diameter variations induced by Ph02 and Ph05 for 18NiCrMo5

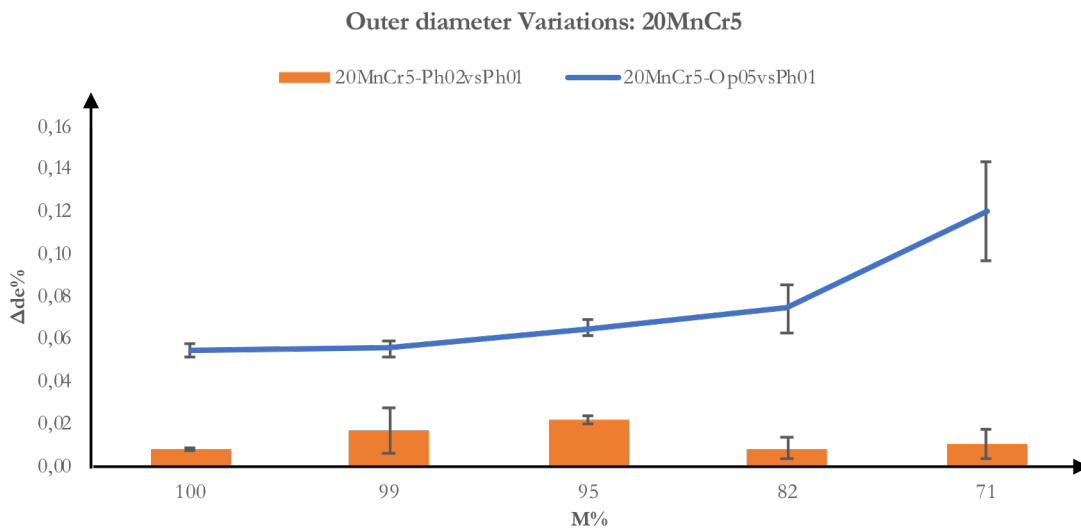


Figure 3.37: Outer diameter variations induced by Ph02 and Ph05 for 20MnCr5

3.8 Thickness

The thickness analysis was carried out through the same methodology that governed the diameters investigations presented in the previous paragraphs.

3.8.1 OTOQ-Thickness variations

Fig. 3.38 displays the thickness distortions for the whole materials and samples induced by Ph02. The variations increase when the theoretical thermal modules decrease. Faster cooling rates were achieved from Set A to Set E, inducing a more effective martensitic transformation. 18NiCrMo5 and 20MnCr5 were characterised by minute changes in comparison with 100CrMo7 due to the absence of a prior carburising phase. This is shown in Fig. 3.38.

ANOVA analysis attributed the major influence to the material effect (F-Value=378,5), followed by the geometry impact (F-Value=63,6) and finally by the interaction that was not relevant due to F-Value=2 (below the threshold=2,7). Fig. 3.39 and Fig. 3.40 illustrate the ANOVA results, looking at both main effects as well as the interaction. The variations enhance from M%=100 to M%=71, display a linear behaviour from Set A to Set D and a maximum value for geometry E, Fig. 3.39 (a). Overall distortions were close to zero after Ph02 due to the absence of the carburising phase for 18NiCrMo5 and 20MnCr5 and,

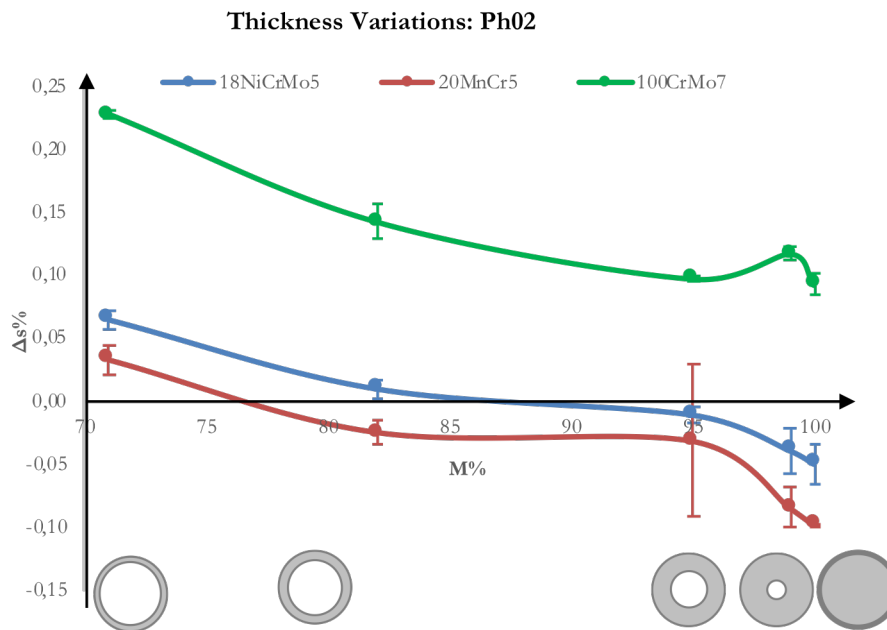


Figure 3.38: Thickness variations induced by Ph02

thus, the correct microstructure was only induced for 100CrMo7, which fully-hardened and produced the highest distortion. This is visible in Fig. 3.39 (b). Fig. 3.40 shows the

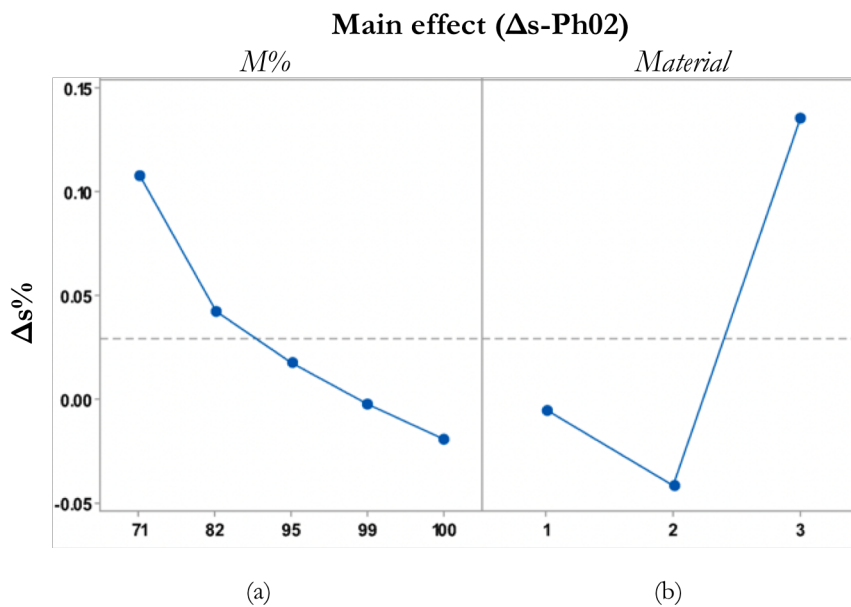


Figure 3.39: The ANOVA main effects concerning (a) materials and (b) geometries of the thickness variations induced by Ph02

comparison of thickness variations in material 1 and material 2 for all sets of geometries. The highest variations occurred in Material 1 while 100CrMo7 presented an increasing

trend from M%=100 to M%=71.

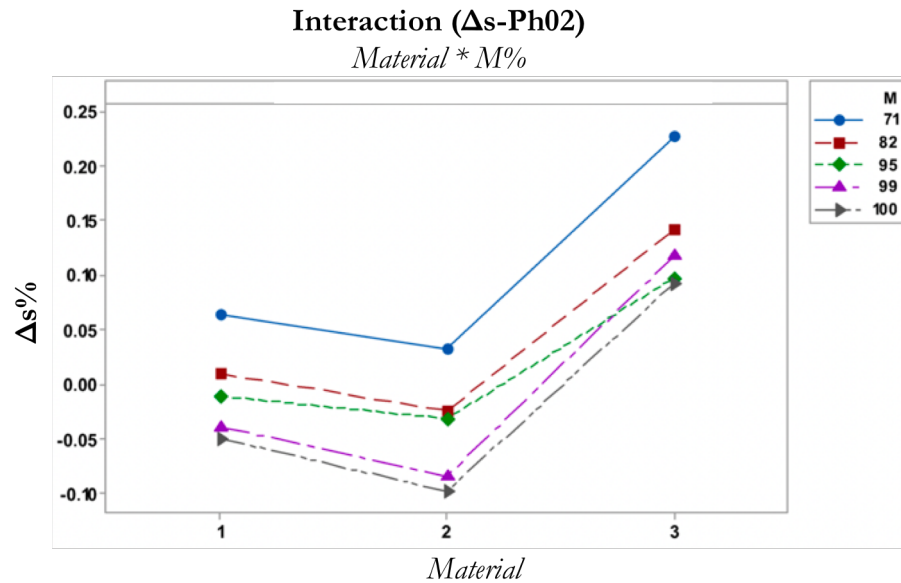


Figure 3.40: The ANOVA interaction regarding the thickness variations induced by Ph02

3.8.2 DAOQ-Thickness variations

Fig. 3.41 illustrates the thickness variations induced by Ph05 for all the experimental samples. The carburising steels display lower distortions in comparison with 100CrMo7. 18NiCrMo5 shows an increasing trend from Set A to Set C that then turns into a plateau until Set E. 20MnCr5 also portrays a similar trend for the heavier geometries, followed by a linear enhancement from Set C to Set E, red and blue lines in Fig. 3.41.

100CrMo7 reveals an enhancement from Set A to Set B, a plateau from Set B to Set C and a linear increase from Set C to Set E, the green line in Fig. 3.41.

The ANOVA analysis determined the highest effect of material (F-value=808), followed by the M% (F-Value=99,3) and then the interaction (F-Value=8,4). Fig. 3.42 (a) pictures a linear increase from M%=100 to M%=71, while Fig. ??(b) illustrates the highest variations for Material 3, followed by Material 4 and then Material 5.

The highest deformations were obtained for Set E, while lower distortions were determined for the other sets depending on the transversal sections. No substantial increases in thickness variations were determined for the carburising materials, whereas significant changes were evidenced for 100CrMo7. This is illustrated in Fig. 3.43.

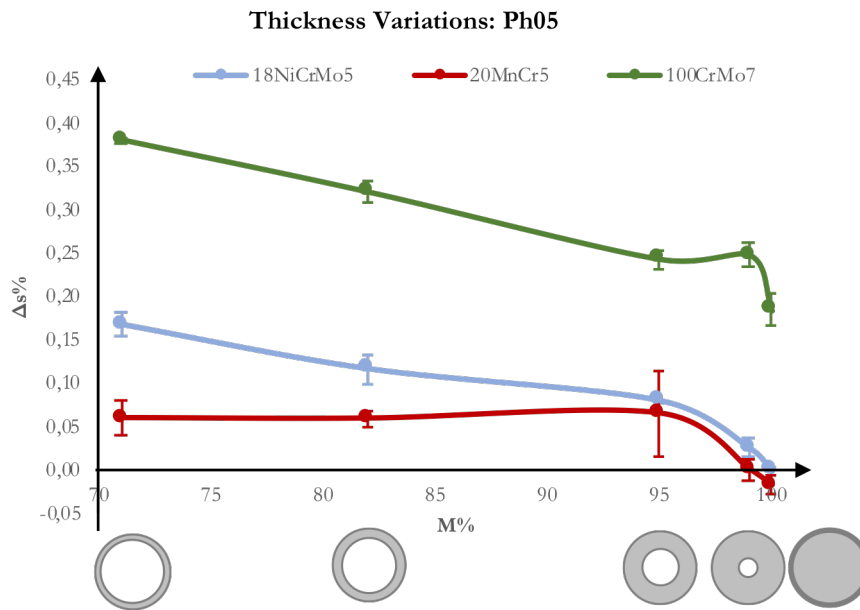


Figure 3.41: Thickness variations induced by Ph05

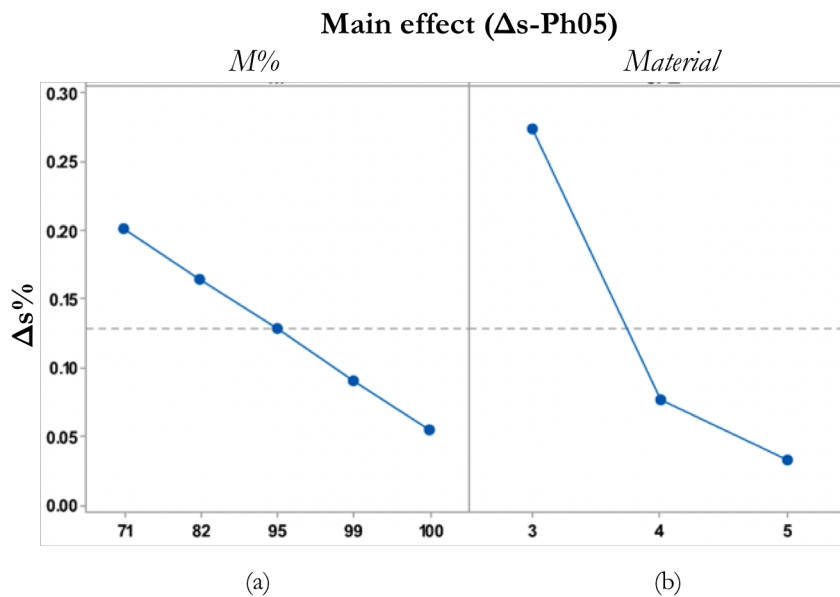


Figure 3.42: The ANOVA main effects concerning (a) materials and (b) geometries of the thickness variations induced by Ph05

3.8.3 Conclusion regarding thickness variations

The final analyses regarding the thicknesses were conducted comparing both quenching processes with previous manufacturing steps (Ph02-Ph01) and (Ph05-Ph04). Fig. 3.44 displays the variations induced by Ph02 and Ph05 for 100CrMo7. Higher magnitudes after Ph05 were determined for the hardening steel and the 18NiCrMo5 in all geometries when

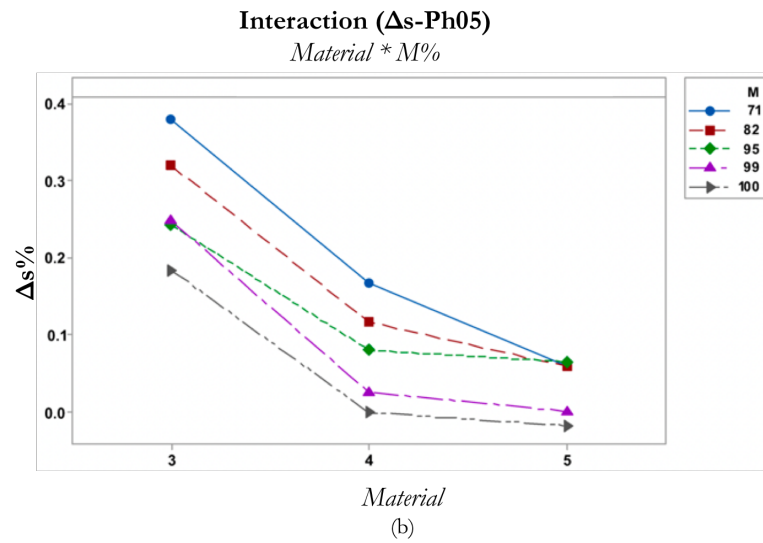


Figure 3.43: The ANOVA interaction regarding the thickness variations induced by Ph05

compared with Ph02. This is visible in Fig. 3.44 and Fig. 3.45. Fig. 3.46 portrays the variations for 20MnCr5. No identifiable trend for Ph05 can be seen but an enhancement can be assessed from Set A to Set E.

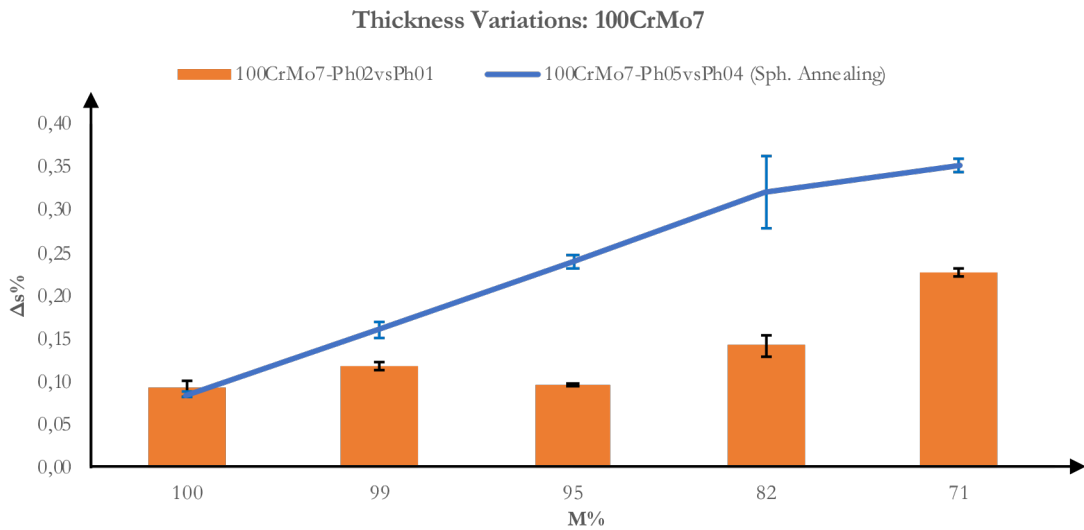


Figure 3.44: Thickness variations induced by Ph02 and Ph05 for 100CrMo7

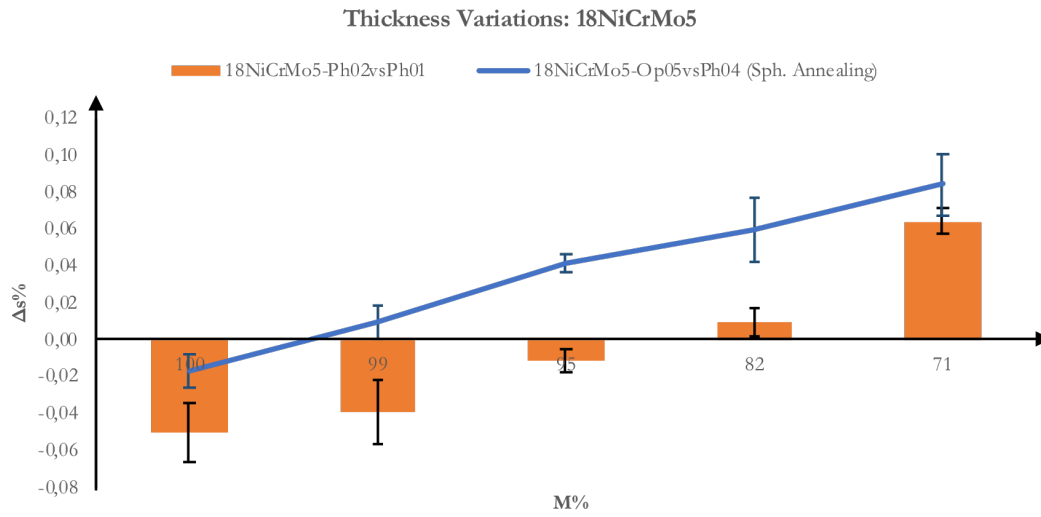


Figure 3.45: Thickness variations induced by Ph02 and Ph05 for 18NiCrMo5

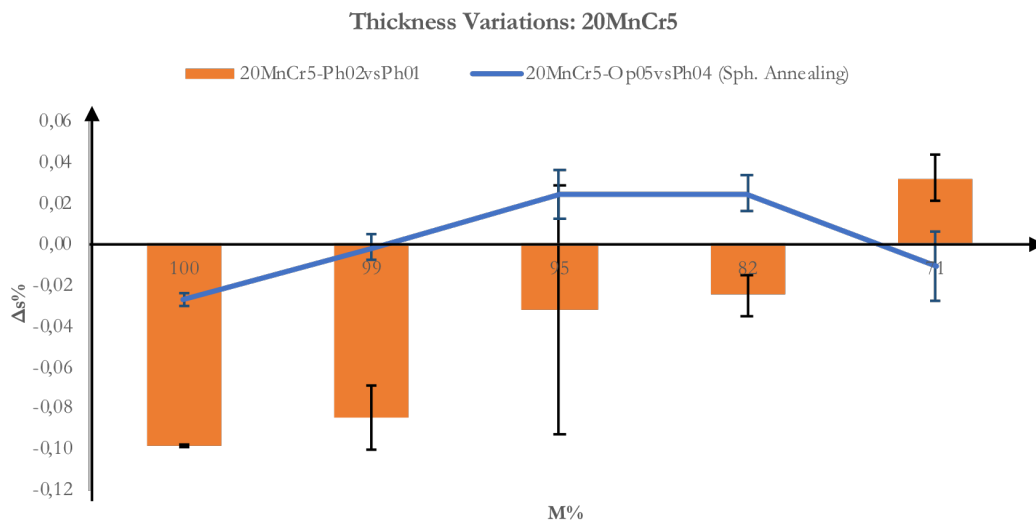


Figure 3.46: Thickness variations induced by Ph02 and Ph05 for 20MnCr5

3.9 Shape Tolerance: investigation into the Planarity Tolerance

As well as the quenching process distortions examined, there are also alterations regarding shape tolerances. This section investigates the planarity variations induced by both Ph02 and Ph05, taking into account the experimental finding and comparing them for each material, firstly looking at changes in 100CrMo7, then carburising materials and finally conclusions regarding the planarity modifications.

Each statistical value, expressed by a mean value and a standard deviation, was determined through the replications that characterised each set of material and geometry. All data were evaluated in percentage values comparing Ph02 with Ph01 as well as Ph05 with Ph04 through the following equations:

$$\Delta_{\text{plane}}\%Ph02 = \frac{Plane_{Ph02} - Plane_{Ph01}}{Plane_{Ph01}} 100 \quad (3.2)$$

$$\Delta_{\text{plane}}\%Ph05 = \frac{Plane_{Ph05} - Plane_{Ph04}}{Plane_{Ph04}} 100 \quad (3.3)$$

The figures show the planarity variations regarding Plane 1 and Plane 2, individually considering 100CrMo7, 18NiCrMo5 and 20MnCr5. When the changes were positive, the planarity tolerances enhanced due to the induced quenching distortions, whereas when the differences were negative the flatness tolerances recovered along the process. Across the whole set of geometries and materials, Plane 1 and Plane 2 displayed similar behaviours, in particular, a worsening after the OTOQ process but an improvement after DAOQ, signifying that tolerance levels were returned by Ph05 thanks to the combined effect of press and mould. Fig. 3.47, Fig. 3.48, Fig. 3.49, Fig. 3.50, Fig. 3.51, Fig. 3.52.

Fig. 3.47 and Fig. 3.48 display the planarity variations for 100CrMo7.

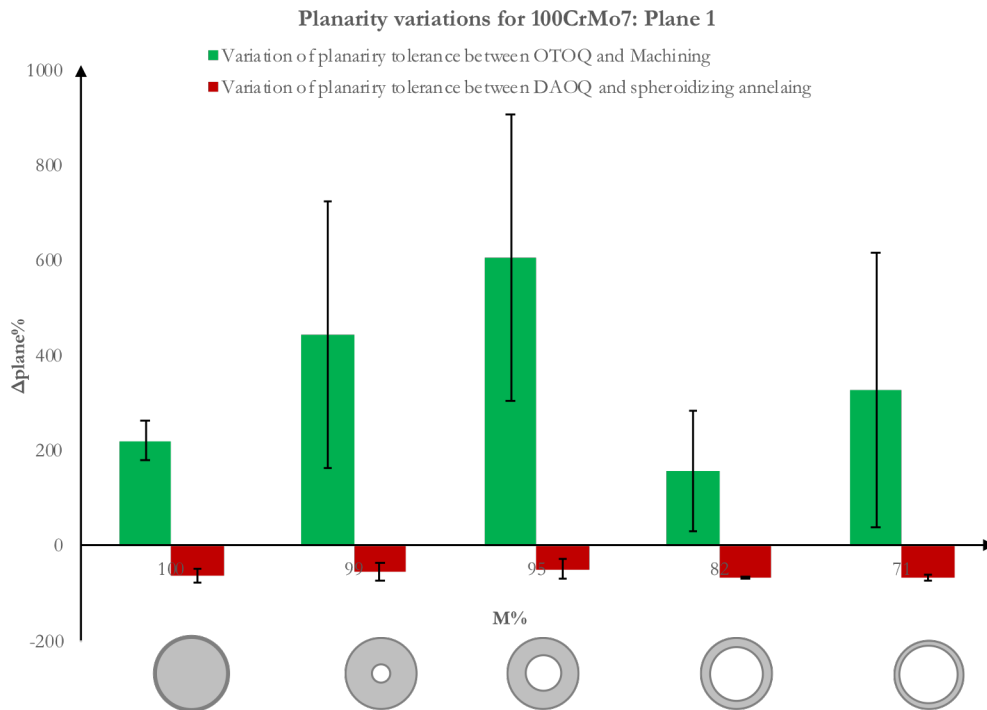


Figure 3.47: Plane 1 - planarity tolerances induced by Ph02 and Ph05 for 100CrMo7

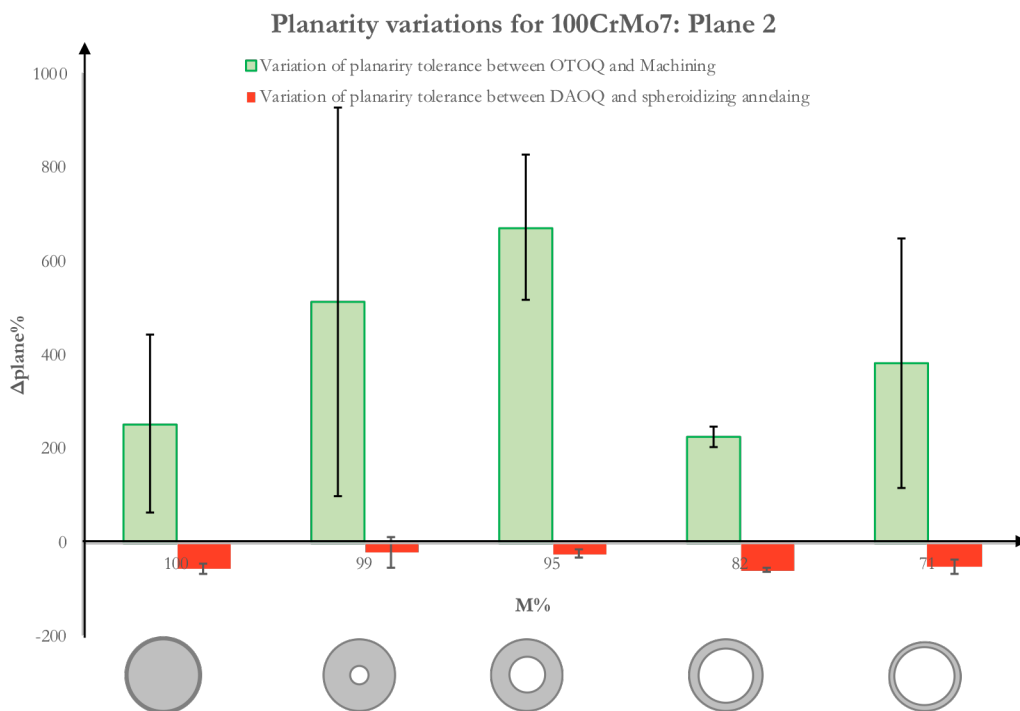


Figure 3.48: Plane 2 - planarity tolerances induced by Ph02 and Ph05 for 100CrMo7

Fig. 3.49 and Fig. 3.50 portray the planarity variations for 18NiCrMo5.

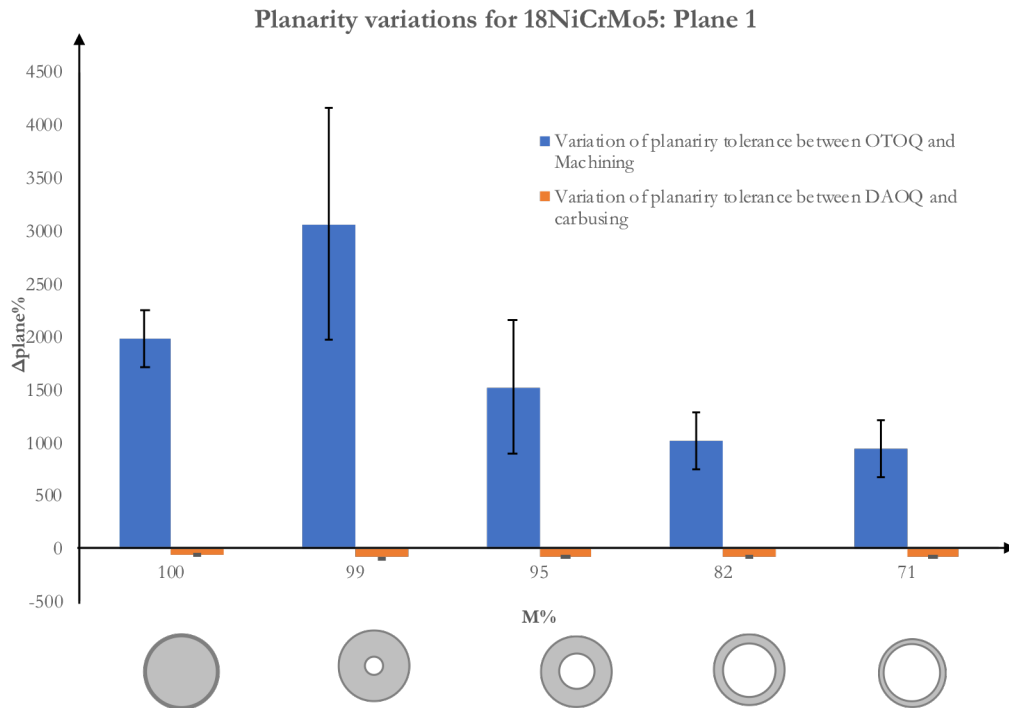


Figure 3.49: Plane 1 - planarity tolerances induced by Ph02 and Ph05 for 18NiCrMo5

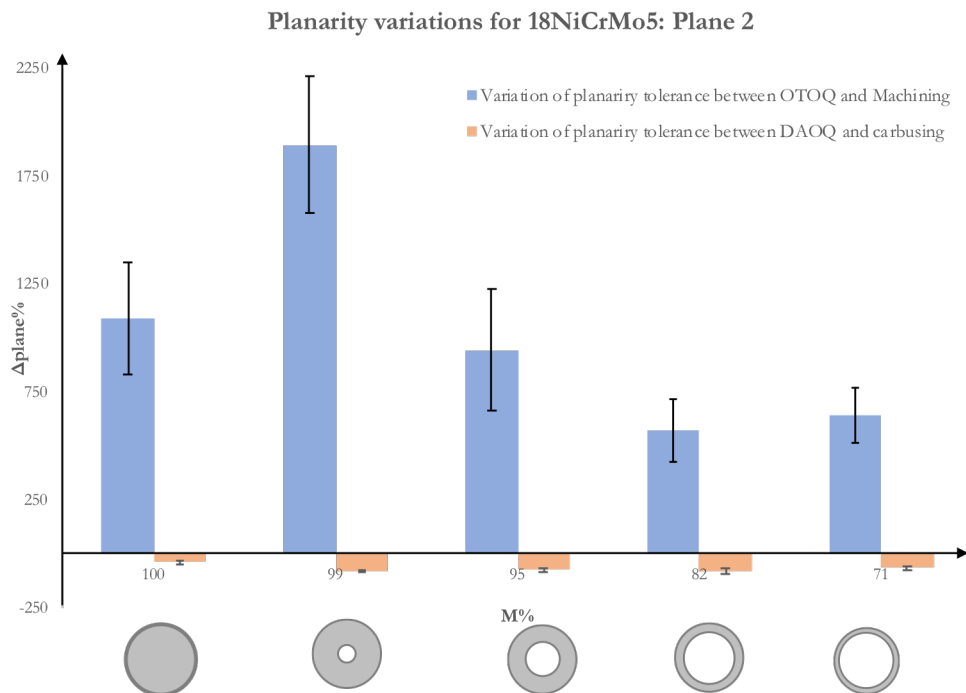


Figure 3.50: Plane 2 - planarity tolerances induced by Ph02 and Ph05 for 18NiCrMo5

Fig. 3.51 and Fig. 3.52 illustrate the planarity variations for 20MnCr5.

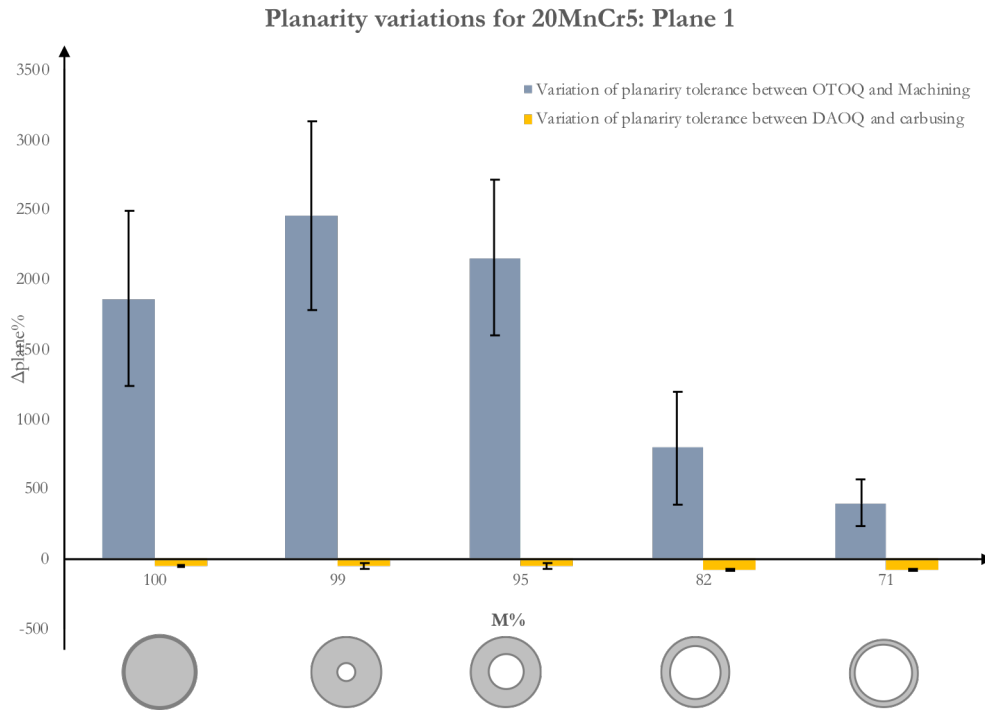


Figure 3.51: Plane 1 - planarity tolerances induced by Ph02 and Ph05 for 20MnCr5

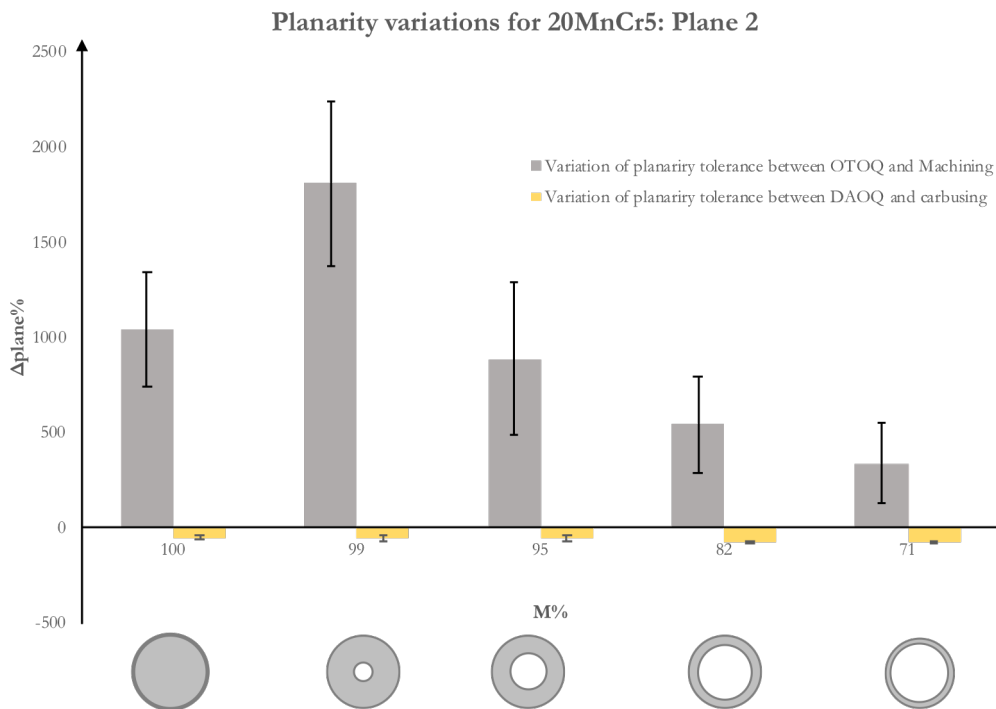


Figure 3.52: Plane 1 - planarity tolerances induced by Ph02 and Ph05 for 20MnCr5

Results show that the DAOQ process minimises distortions, which allows for lower

machining allowances during the product design and consequently a reduction in the amount of employed material as well as a decrease, or perhaps even avoidance, of post-process quenching operations.

3.10 Comparison between Mineral and Vegetable Quenching Oils

A study was also conducted of different quenching oils derived from petroleum or vegetable base-stocks. The cooling properties and in-process performances were analysed, focusing evaluation on their sustainability aspects.

3.10.1 Cooling curve analysis

A preliminary comparison was conducted to understand the main characteristics and differences between a vegetable based oil (named "tempro G Bio Plus") and a petroleum based quenchant (named "tsp6"). A technical comparison was realised by the cooling test to determine the oily in-process performances, [33]. Fig. 3.53 shows the experimental curve for both the oil formulation [29]. A notable difference is that the "tempro G Bio Plus" displays a reduced vapour formation at a higher temperature and its maximum cooling rate is at 640°C, as opposed to 575°C in the case of the mineral medium.

Fig. 3.53 displays the quenching cooling stages realised by liquid mediums. The petroleum-based oil shows a more extended vapour blanket stage than the vegetable medium due to the lower boiling temperature, [31]. A shorter boiling stage results in a more effective boiling section, reaching the maximum cooling rate at the higher temperature and hence a more rapid cooling could be ensured by the vegetable medium. The Convective stage was achieved equally by means of both oils. Decreasing the quenchant severity meant a better control of shape and dimensions could be obtained although it induces unwanted microstructural phases such as upper bainite.

Thus it was observed that the selection of the right mediums is a critical choice when aiming to reduce distortions. The film boiling, that surrounds the part, should collapse at the same time ensuring equal cooling conditions in terms of HTC across the quenched

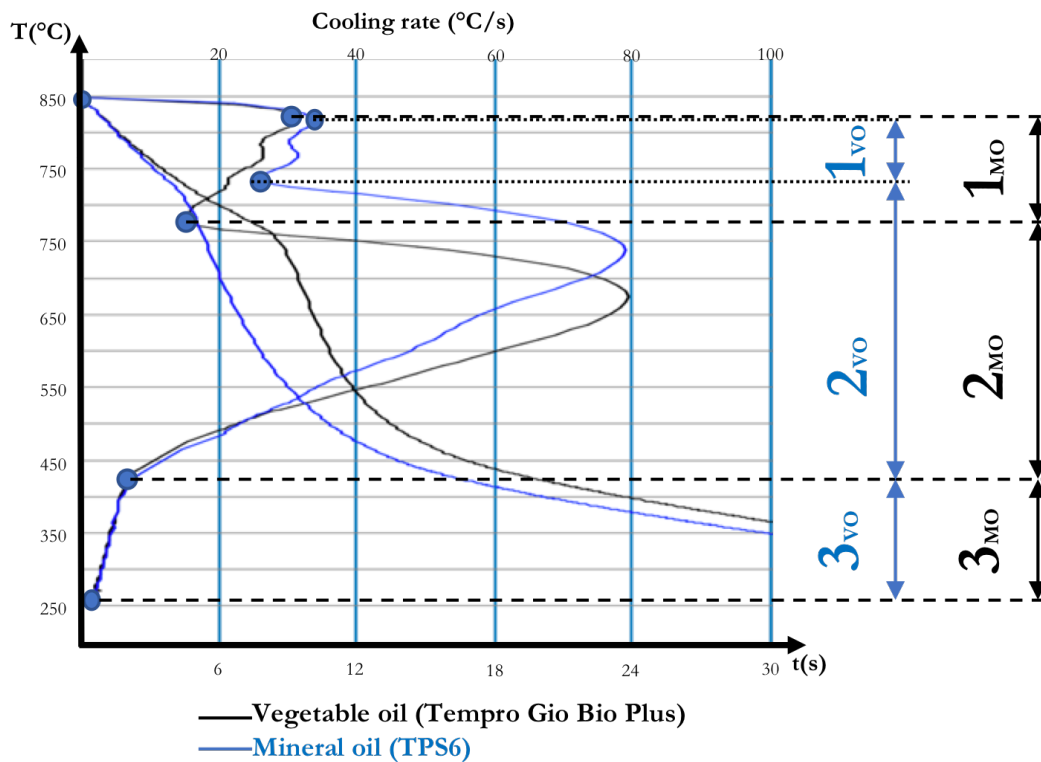


Figure 3.53: Cooling rate as a function of the oil temperature. Experimental curves of the vegetable (blue curve) and mineral (black curve) quenching medium

part. Consequently, homogeneous decreasing in temperature reduces residual stresses and distortions. In this respect, the vegetable based mediums performed better.

3.10.2 Impact comparison

In [54] a Life Cycle Assessment (LCA) was realized by comparing petroleum-based diesel oil with a soy-based lubricant. Only the production chain was considered without additives. Agriculture, crushing and refining were taken into account for the production of vegetable medium whereas extraction, finish and refining were accounted for the mineral based oil.

The soy-based oil presented lower impact evaluations in terms of global warming, acidification potential, water intact, air pollution and human toxicity. The eutrophication potential was higher in the case of the vegetable quenching media; this could be also related to the use of unsafe substances such as pesticides that modify soil conditions. The impact assessments of vegetable quenching media were also correlated to the working method implied for the growing of the oily based plants as well as to the

in-working conditions that can change the oil properties. These innovative fluids have to be appropriately modified with additives especially for increased oxidation resistance [29], [55].

The main sustainability indicators were modelled by means of an LCA regarding the production of the vegetable quenching oil. Agriculture and crushing were determined by utilising bibliography data [30] and by considering the production of the investigated oil as equal with the data presented in the reference study for the soybean quenchant [30]. The refining stage was set by using real data obtained from the oil manufacturer but with no estimation of the additive influences. The LCA of the mineral quenching oil was also deducted from [30]. Fig. 3.54 shows the adopted structure of the LCA that was implemented by the Open LCA software. Fig. 3.55 displays the main results of the impact comparison between the vegetable and mineral media.

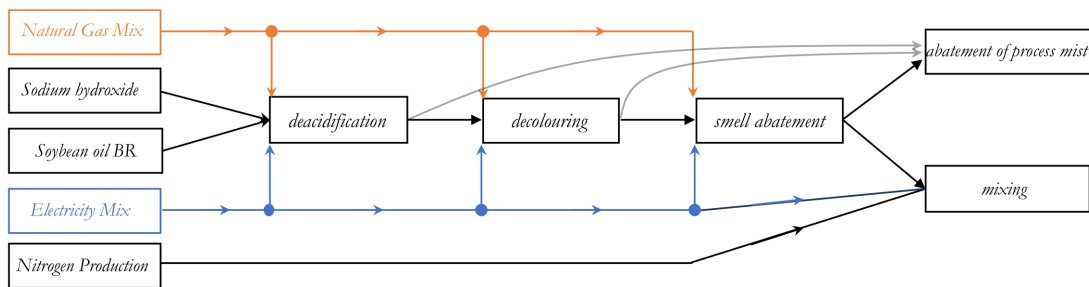


Figure 3.54: Open LCA software model for a soybean vegetable oil

An increasingly notable issue in manufacturing is the factor of climate change. GWP100 indicates a negative trend for the vegetable quenchant: a life cycle for the oily plant with an increased absorption of carbon dioxide and a decreasing of the GWP100 indicator. The mineral quenching oil also shows a low GWP100 impact, indicating the high standards utilised in its production. [30]. Ozone Layer Depletion (OLD) and Acidification potential could be further reduced by means of the vegetable quenching oil, as reported in Fig. 3.55.

3.10.3 Experimental activity

Sustainable manufacturing promotes improvements of processes and products in order to achieve a better working environment by enhancing the manpower value without compromising manufacturing results. The following experimental activity investigates

Results from LCA	Vegetable oil	Mineral oil
<i>GWP100</i>		
<i>Climate Change</i> (kg CO ₂ eq.)	-1.34	0.97
<i>OLP</i>		
<i>Ozone layer depletion</i> (kg CFC-11 eq.)	7.30E-09	7.6E-07
<i>Acidification potential-average Europe</i> (kg SO ₂ eq.)	0.01	0.03

Figure 3.55: Comparison between mineral and vegetable oils for relevant impacts

the performance of mineral and vegetable oil for quenching, determining mechanical and metallurgical outcomes, geometrical results and the emission of quenching fumes.

Conical bevel gears made of steel were chosen as the sample geometries. Three geometries were used, characterised by means of the following parameters: the inner diameter (d_i), the ratio between d_i and the outer diameter (d_e) as well as the proportion between the part thickness (s) and d_i , see Fig. 3.2 (a).

Three batches - one batch for each considered geometry - composed of a total amount of 420 mechanical components - 140 part/batch - were submitted to the carburizing phase (Ph_{01}), then to the DAOQ process (Ph_{02}) and, finally, to temper (Ph_{03}). Each half batch was hardened by the use of mineral oil (210 parts, 70x3 specimens) and the rest by the vegetable-based medium. An in-line process control was realised by means of dimensional analyses of each component after Ph_{02} . The dimensional analyses were carried out by utilising manual micrometres and altimeters for the evaluation of diameters, thicknesses and planarity tolerances, as showed in Fig. 3.56 (b). A specific standard for the measurements was established by defining characteristic detection points. 5+5 parts per batch out of the 70+70 components per batch were randomly selected to be submitted to a further dimensional control after the carburizing phase (before the DAOQ process) and after the tempering phase (after the DAOQ process). In the following sections, these selected parts are referred to as the "TOP 5".

Metallurgical samples were analysed through an optical microscope in order to determine the final material microstructure. Quenching fumes were also detected by

	d_i (mm)	I_{g01} $\frac{d_i}{d_e}$	I_{g02} $\frac{s}{d_i}$	Carburising Steels
Geometry1	159,60	0,59	0,23	20MnCr5
Geometry2	159,60	0,53	0,23	19MnCr5
Geometry3	116,00	0,48	0,32	19MnCr5

(a)



(b)

Figure 3.56: (a) Identification of the investigated conical bevel gears; (b) measurement equipment for the evaluation of the planarity tolerances

means of a probe through a by-pass installed above the quenching chamber that directly captured the fumes from the hardening zone. Oily fog and CO contents were measured in-process. The in-process fume equipment is depicted in Fig. 3.57.

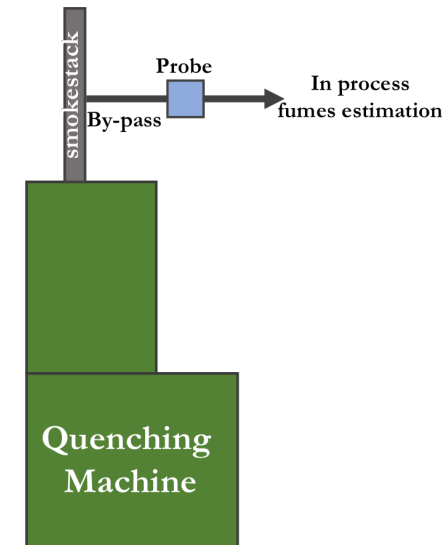


Figure 3.57: *In-process equipment for the detection of quenching fumes*

3.10.4 Analysis of the experimental data

The mentioned t-test was carried out for the TOP5 selection by comparing the dimensions of each controlled geometrical characteristics after Ph_{01} , Ph_{02} , Ph_{03} .

The t-critical value was set for the two sides t-distribution with 0,95 as the probability reference [56]. The comparison generated eight degrees of freedom for the experiment, which resulted in a critical value equal to 2,3.

Table 3.1 collates, for each geometrical investigation, the t-test parameter matched with the corresponding threshold value. These variations point out the impact of the quenching oils on to the detected geometrical characteristics (Ph_{02}). Ph_{02} analysis is also compared.

Table 3.1: *In-process equipment for the detection of quenching fumes*

TOP5	Geometry 1	Geometry 1	Geometry 2	Geometry 2	Geometry 3	Geometry 3
selection	<i>t-value</i>	<i>t-value</i>	<i>t-value</i>	<i>t-value</i>	<i>t-value</i>	<i>t-value</i>
Detected phase	Ph_{01}	Ph_{02}	Ph_{01}	Ph_{02}	Ph_{01}	Ph_{02}
inner diameter	0.1	3.3	-1.2	-1.7	0.0	-1.8
outer diameter	-1.3	2.2	0.5	3.3	-0.1	3.3
thicknesses	1.9	0.0	-2.6	1.9	0.9	1.8
planarity tolerance	-0.3	3.6	-1.1	1.0	2.1	0.6

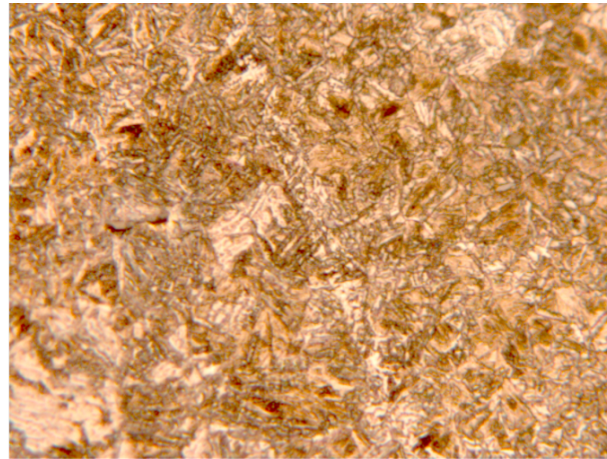
The outer diameters were virtually always affected by the use of mineral or vegetable quenching oil. The inner diameter of geometry 1 showed the same behaviour while geometry 2 and geometry 3 presented a different result. Thicknesses did not produce relevant variations (in comparison with the Ph_{01}). Planarity tolerances had relevant

variations only in the case of geometry 1.

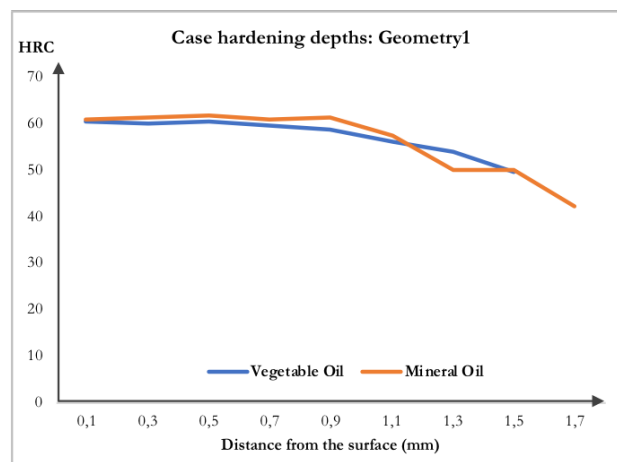
The DAOQ equipment controls and modifies the heat extraction by means of a direct metallic contact between the part and the die surfaces, which are cooled through the quenchant. The process outcome is then connected not only to the quenching media but also to the process equipment and related parameters (die contact-surface and pressure, oil flux and pressure, etc.). The experiment showed that the DAOQ process in particular allowed the control of some distortion magnitudes (planarity and thicknesses) whereas the effect of different cooling oils is evident on the dimensions that are not influenced by the constrained heat flux (the inner and outer diameters).

Metallurgical and hardness inspections

The cooling curves (Fig. 3.53) of investigated oils show comparable trends also if relevant differences are present. It implied that, concerning the cooling severities of the considered media, no large dissimilarities were observed. In fact, both the oils determined the formation of the martensite microstructure after the DAOQ process. Furthermore, the hardening depths of the two oils show overlapping trends, thus implying the same mechanical results in terms of superficial hardnesses (equal to 60 HRC) and process effectiveness seen by the absence of noteworthy hardness variations, see Fig. 3.58 (b). The presence of comparable hardening depths underlines the effectiveness of the vegetable quenching oil on heat treatment outcomes.



(a)



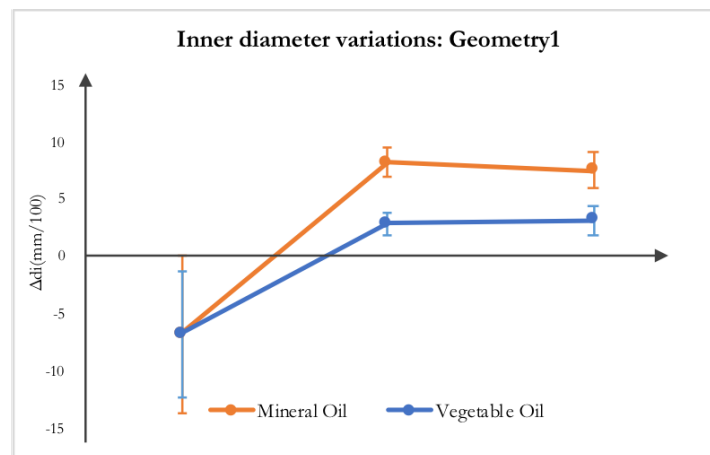
(b)

Figure 3.58: (a) *Martensite microstructure obtained by the usage of mineral and vegetable quenching oils; (b) Experimental evaluation of superficial hardnesses and case depths for both mediums*

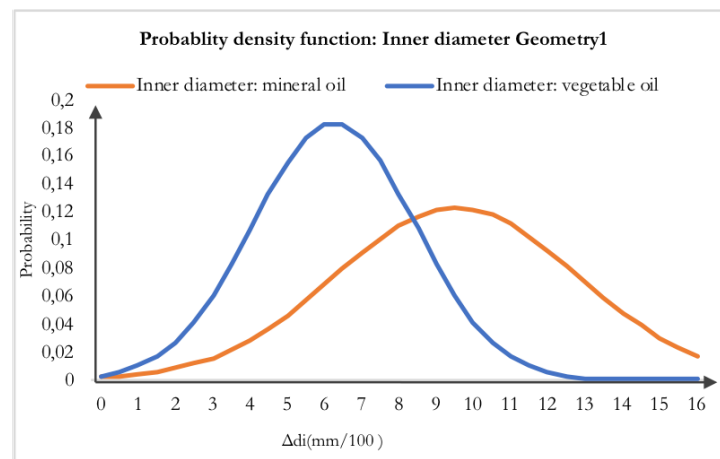
Analysis of part dimensions

After the carburising phase, due to the absence of process dissimilarities at his stage of the manufacturing cycle, no relevant dimensional variations were reported for the considered geometrical characteristics thus leading to the same starting conditions for the quenching phase. Following the DAOQ process, it is notable that the inner hole of geometry 1 was significantly increased. After starting from equal conditions following the carburising phase, all the dimensions unavoidably increased. One example is the inner diameter variation using the vegetable quenching oil, which was lower than the one determined by the mineral medium, Fig. 3.59 (a). A further and more important

difference is a more accurate quenching stage as the in-process analysis clearly evidences in Fig. 3.59 (b).



(a)



(b)

Figure 3.59: (a) TOP 5 analysis: Evolution of inner diameters of geometry1 along the process stages; (b) In-line process control: Gaussian distributions of distortions regarding the inner diameters of geometry1

To summarise, the renewable based medium achieves an equal metallurgical microstructure, Fig. 3.58, and equivalent mechanical results by increasing the possibility of dimension control, Fig. 3.59.

Oily fog measurements

Samplings of quenchant fumes were recorded for one hour through an in-process experimental measurement for both the considered oils. The vegetable quenching medium put in evidence the presence CO (1.7 mg/Nm³) and the absence of oily fogs (less than 0.01 mg/Nm³). The mineral oil showed both these pollutants in its emission with 1.8 mg/Nm³ of CO and about 1.2 mg/Nm³. By considering a yearly industry scenario (220 days/year and 8 hrs/day), the mineral oil produces 7 kg/year of oily fog. Air purification is required before its re-introduction in the environment and the choice of vegetable based mediums would create additional sustainable savings by reducing the energy used in this purifying process.

Conclusion regarding the oil comparison

In conclusion, the conducted activities successfully compared the mineral and the vegetable quenching mediums. The same mechanical and metallurgical results were achieved by both oils, the vegetable-based one producing no loss in quality, furthermore it allowed for superior control of specific crucial dimensions, such as in the inner diameter of the considered conical gear. The preliminary LCA analysis puts in evidence several possible points of strength for this production media alongside the evident environmental advantages. Tests have shown the important comparative differences of these mediums through the analysis of a typical production cycle and the measurement of emitted pollutants including oily fogs and carbon monoxide, which must be controlled and purified before the reintroduction of the air into the environment.

The presented work suggested that innovative vegetable-based oils could be a worthy choice and a potentially good starting point to transform the heat treatment production plant into a more sustainable working environment. A more detailed LCA is required in order to completely understand all possible advantages and weaknesses of both solutions. Further tests and investigations are called for to discover the full potential of these mediums.

3.11 Summary of Experimental Activities

This chapter presented the whole range of conducted experimental activities 3.2 3.3, focussing on the differences induced by the OTOQ and DAOQ processes. Procedures to measure all the varying types of distortions and volume variations were outlined and an in-depth analysis concerning the diameters and thicknesses was described. The results can be summarised as follows:

- A more effective martensitic transformation was obtained for the 100CrMo7 sample due to its highest carbon percentage but this also led to the major volume variations for both OTOQ and DAOQ in comparison with 18NiCrMo5 and 20MnCr5, as reported in par. 3.5.
- Levelling distortions were determined for the inner as well as outer diameter variations especially regarding the carburising materials. Positive distortions were determined for all the samples except for Set B of 100CrMo7 that showed negative dimensional variations, par. 3.6, par. 3.7.
- The most relevant thickness modifications were determined for the thinner geometries (Set D and Set E) for both OTOQ and DAOQ. Positive variations were also derived from DAOQ even with the pressure effect exerted by the press on the treated part through the outer upper die, par. 3.8.
- Overall, better dimensional and shape controls were performed through DAOQ as highlighted by the investigation on the planarity tolerance, par. 3.9.
- Comparing the two oils, petroleum or vegetable based, the same metallurgical and mechanical outcomes and qualities were achieved. The vegetable quenching medium brought advantages both in improvements to the part geometries and also in reductions in the oily fogs due to a minute vapour blanket stage, par. 3.10.
- The following chapter examines the matching between the modelling achievements and the experimental results. Investigating accuracy and looking at ways to fine-tune and improve both the virtualisation of quenching distortions and the process design.

Chapter 4

Comparison of Model Predictions with Experiments

4.1 Introduction

As discussed, the quenching simulation is a multi-physical process due to the presence of thermal, microstructural and mechanical fields that have to be simultaneously coupled in order to evaluate not only microstructural changes but also the deformations associated with the thermal gradients and volume variations.

Fig. 4.1 illustrates the main results achieved by the OTOQ model through a layered approach, in which the time-dependent conditions manage the entire thermal cycle, as Fig. 4.1 (e) clearly highlights. The presented mathematical model (see Chap. 2) estimates the complete range of process results for each meshing node, generating contour plots Fig. 4.1 (c), aiming at precise outcome previsions in the transversal section. The microstructural evolution was put into practice through Fe-C, as well as the TTT diagrams in the case of 100CrMo7. Several if-then-else conditions were defined to enable the correct path of material evolution, see par. 2.4.4. Fig. 4.1 (a) shows the passage between the initial and austenitic microstructures, leading to a temperature reduction induced by the cooling which activates the development of the final microstructure.

Fig. 4.1 (d) shows the radial displacement evolution and details the dimensional changes encountered by the simulated part during the entire quenching process. During the heating stage, the model is able to manage not only the thermal expansion due to the

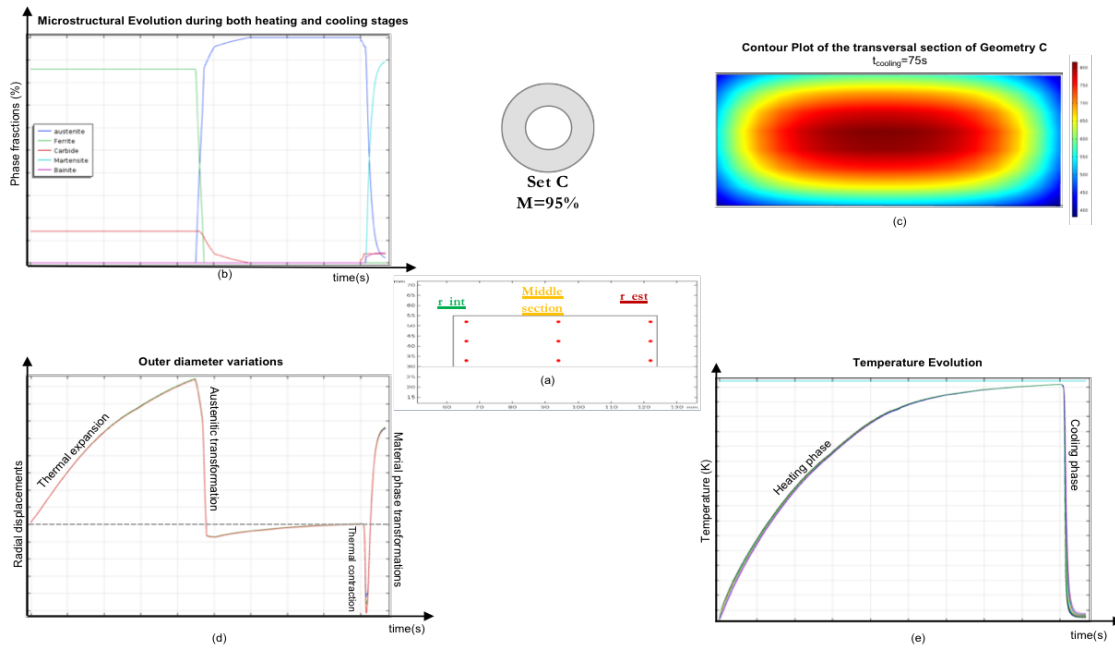


Figure 4.1: (a) 2D axisymmetric model, (b) microstructural evolution, (c) temperature contour plot, (d) evolution of radial displacements, (e) temperature evolution

temperature increase between the treated part and the furnace but also the contraction induced by the austenitic phase transformation. Conversely, the component shows negative radial variations at the beginning of the cooling stage due to the temperature decreasing. The deformation recovers the initial distortions when M_s is reached, becoming positive and achieving a tenth of a millimetre as a final order of magnitude. The mathematical model is able to summarise the mechanical results through an estimation of the hardness, considering all the differing microstructures by means of a mixture rule, eq. 4.1. This is illustrated in Fig. 4.2.

$$HV_{\text{total}} = \%mHV_{\text{martensite}} + \%pHV_{\text{pearlite}} + \%bHV_{\text{bainite}} + \%F_{e_3C}HV_{\text{Fe}_3\text{C}} \quad (4.1)$$

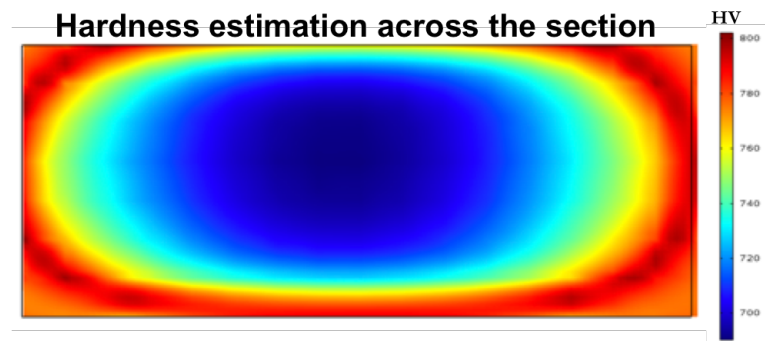


Figure 4.2: *The Hardness estimation taking into account the mixture rule*

4.2 Model setting: definition of the deformations

The deformational modalities were precisely set by selecting coefficients in order to maintain proportion amongst the deformations as presented in par. 2.5. The axisymmetric geometries imposed the definition of two deformational settings in order to replicate the actual part behaviour during the quenching processes.

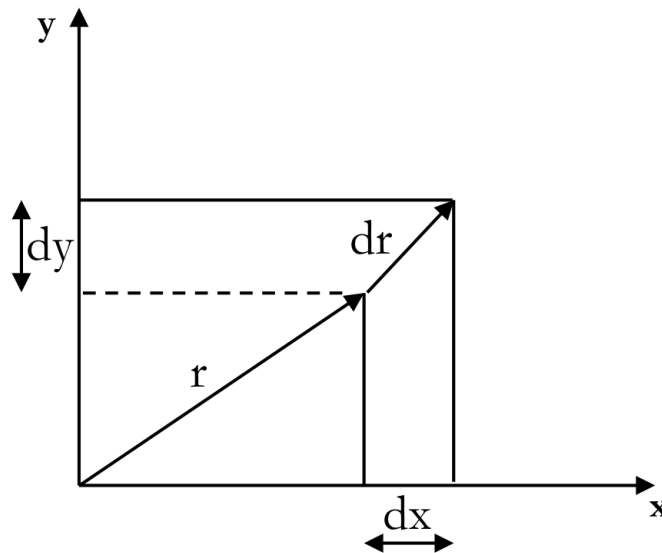


Figure 4.3: *Definition of the proportions among the deformations for model 1*

Following Fig. 4.3:

$$\epsilon r = (\epsilon x + \epsilon y)^{\frac{1}{2}}$$

In addition:

$$\epsilon x = \epsilon y = \frac{\Delta L}{L} = \epsilon l$$

Eq. 2.25 defines:

$$\frac{\Delta V}{V} = 3 * \epsilon l$$

Model 1 was set as follow:

$$\epsilon r = \sqrt{2}\epsilon l$$

$$\epsilon \theta = (2 - \sqrt{2})\epsilon l$$

$$\epsilon z = \mathbf{1}\epsilon l$$

As a counterpart, model 2 was defined by:

$$\epsilon r = \mathbf{1,5}\epsilon l$$

$$\epsilon \theta = \mathbf{0,75}\epsilon l$$

$$\epsilon z = \mathbf{0,75}\epsilon l$$

The quenching model and the real measurements were compared by considering average values of inner diameters and selecting the detection points evaluated through the experimental activity. HTC's were equally assigned to each surface (Fig. 2.3) and derived from [57], [58]. HTC's are investigated in terms of real-trends, [57], and ranges depend on the liquid mediums, [58]. It is crucial to note that the quenching outcomes are strictly connected to the selection of suitable HTC's in order to replicate the in-process conditions.

The multi-physical software was utilised for the simulation of the quenching process by implementing the whole set of partial differential equations as well as the functions and variables of the material properties. Fig. 4.4 illustrates the overlap between virtual and experimental results regarding the setting of model 1. By setting up a constant during the cooling phase as well as an equal HTC for each external surface, the model

can replicate the both experimental trend of the inner diameter variations - particularly well approximated for geometries D, C and B – and also show the negative deformation for geometry B. Thus, the negative variation is both experimentally and virtually obtained, Fig. 4.4. This confirms the capability of the model to well replicate the measured dimensional variations. A more precise quenching model can be achieved for geometry E: components characterised by lower theoretical thermal modules, such as Set E or Set D. The tuning activities are presented in par. 4.3 and investigate the effect of the HTC's on the quenching outcomes.

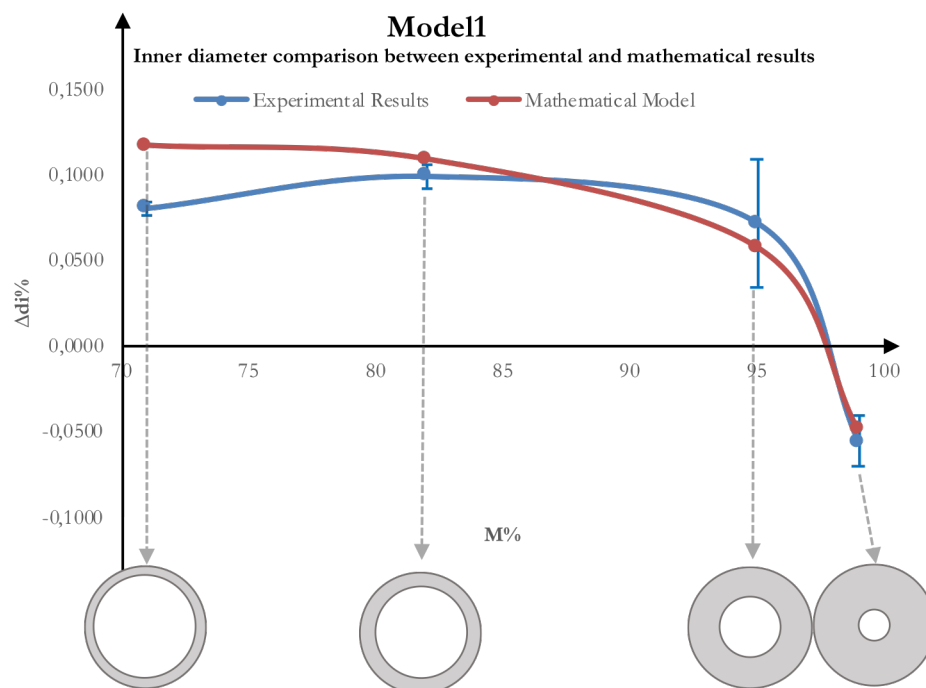


Figure 4.4: *The Overlapping between modelling and experimental outcomes for model 1*

In summary, the self-developed quenching model is able to accurately replicate the experimental outcomes, particularly regarding inner diameters variations. Furthermore, the transformation from negative to positive deformations was successfully addressed not only by the experiments but also by the simulations, obtaining an equivalence of results. Fig. 4.5 portrays the section where the inner diameter deformation becomes non-existent.

Model 2 was based on differing deformational coefficients and it revealed dissimilar modelling results in comparison with Model 1. The negative deformation predicted by Model 1 was not registered by Model 2, nonetheless the overall trend was substantially

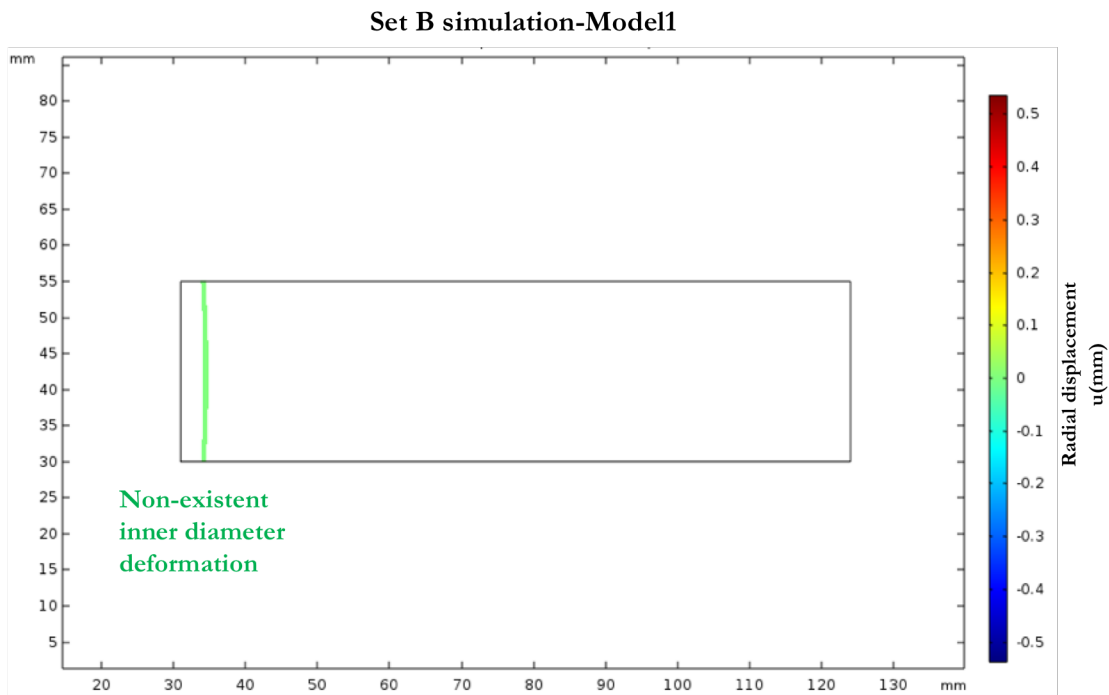


Figure 4.5: Simulated null deformations of inner diameter taking into account model1

approximated. This is visible in Fig. 4.6. Decreasing the inner diameter of the part, Model 2 is also able to evaluate the negative deformations and evidence where the radial displacement becomes close-to-zero, as illustrated in Fig. 4.7.

The virtual outcomes are strictly connected to process conditions. They change by modifying HTCs throughout the heating as well as the cooling stages. Due to the main focus on final predictions, the most suitable HTC values along the cooling stage have to be accurately determined in order to replicate the experimental findings. The following section concerns a virtual design of experiment in which both models were analysed through nine simulations based on the Taguchi method to understand the effects of HTCs on the predictions, [56]. Set C was used exclusively for this investigation.

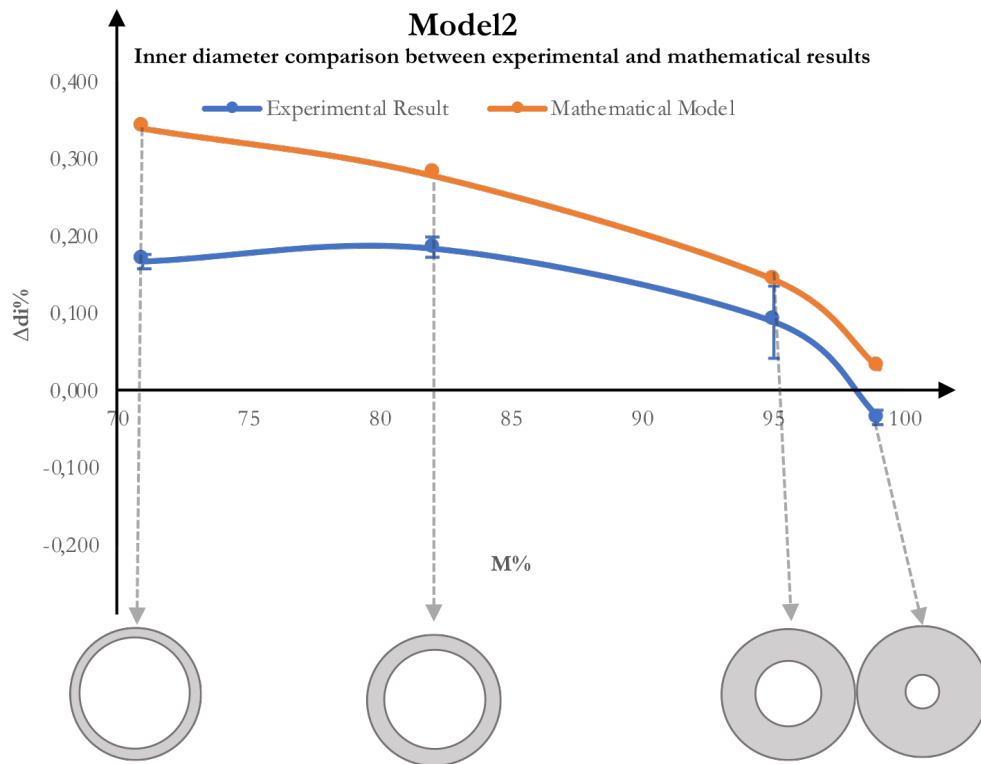


Figure 4.6: The Overlapping between modelling and experimental outcomes for model 2

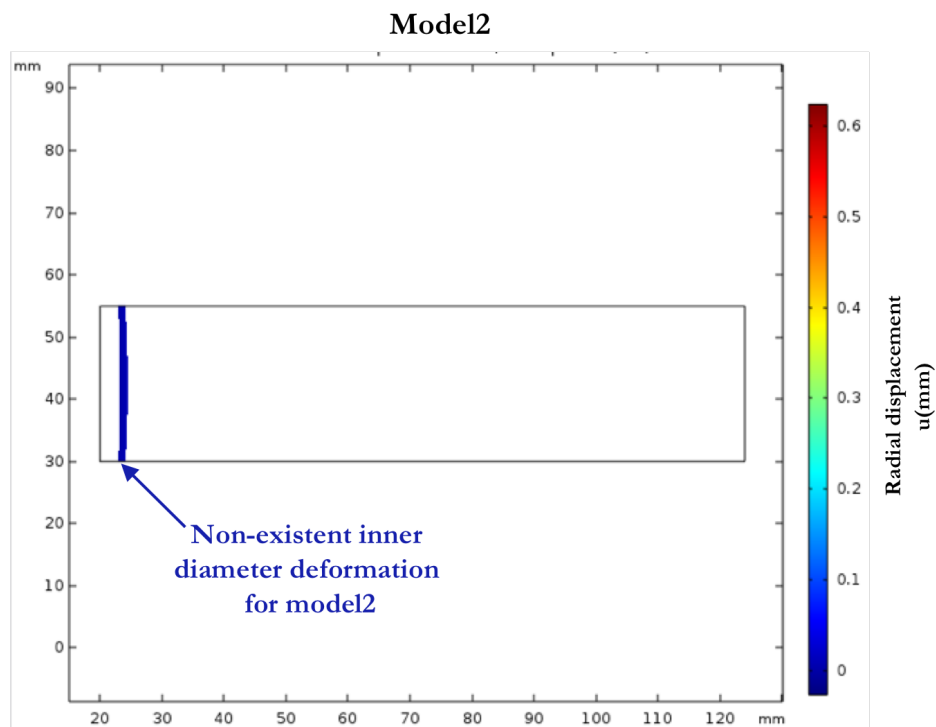


Figure 4.7: Simulated null deformations of inner diameter taking into account model2

4.3 Influence of HTC's on the Predictions

The outcome predictions are linked to the process conditions in which mechanical components are treated. The realised mathematical model is based on the determination of reliable-HTC-values in order to replicate the experimental conditions. This parameter drives the modalities of heat flux exchanges by means of equations and time-dependent interfaces, chap. 2. The analysis regards the magnitudes as well as the assignment of HTC's based on the position of each surface. The investigation was engineered employing DoE concepts and only the HTC's were changed without modifying the other model settings. The HTC's were respectively assigned to:

- HTC1: inner edge that determines heat exchange modality along the internal surface;
- HTC2: bottom edge that determines heat exchange modality along the lower surface;
- HTC3: outer edge that determines heat exchange modality along the external surface;
- HTC4: upper edge that determines heat exchange modality along the upper surface;

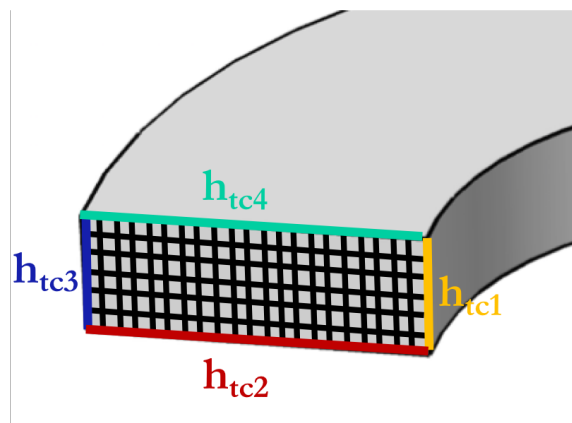


Figure 4.8: Matching between HTC's and model boundaries

HTC's were set at three levels to comprehend all the oily mediums in the experiment, [58]. Tab. 4.1 summarises the developed simulations for both models. Taking into account three levels of HTC's (1500-3000-4500 $\frac{W}{m^2K}$) and four factors

(HTC1-HTC2-HTC3-HTC4), eighty-one simulations were required to develop the virtual experimental plan. The Taguchi Method allowed for a reduction in the total number of simulations, as reported in Tab. 4.1.

Table 4.1: *Realised simulations for both models through Taguchi method*

Simulation	HTC1	HTC2	HTC3	HTC4
I	1500	1500	1500	1500
II	1500	3000	3000	3000
III	1500	4500	4500	4500
IV	3000	1500	3000	4500
V	3000	3000	4500	1500
VI	3000	4500	1500	3000
VII	4500	1500	4500	3000
VIII	4500	3000	1500	4500
IX	4500	4500	3000	1500

Each simulation was analysed by looking at 2D results as well as evaluation points (characterised by r and z coordinates), as explained in par. 2.6 and illustrated in Fig. 4.9.

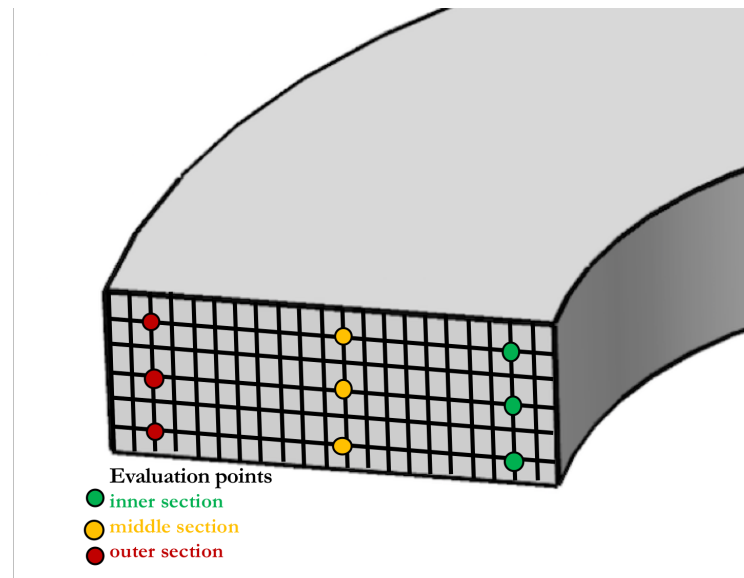


Figure 4.9: *Evaluation points for each simulation*

The following sections show how the analyses were conducted and outline the entire investigation process regarding temperatures, microstructures and displacements.

4.3.1 investigation regarding Model1

Model 1 Results

This section displays the thermal, microstructural and deformation outcomes obtained by Model 1. Firstly, just one random simulation is fully illustrated and then the whole range of results are examined using Taguchi Analysis, graphically representing the influence of each HTC on the selected outcome. The initial temperature investigation is presented in Fig. 4.10.

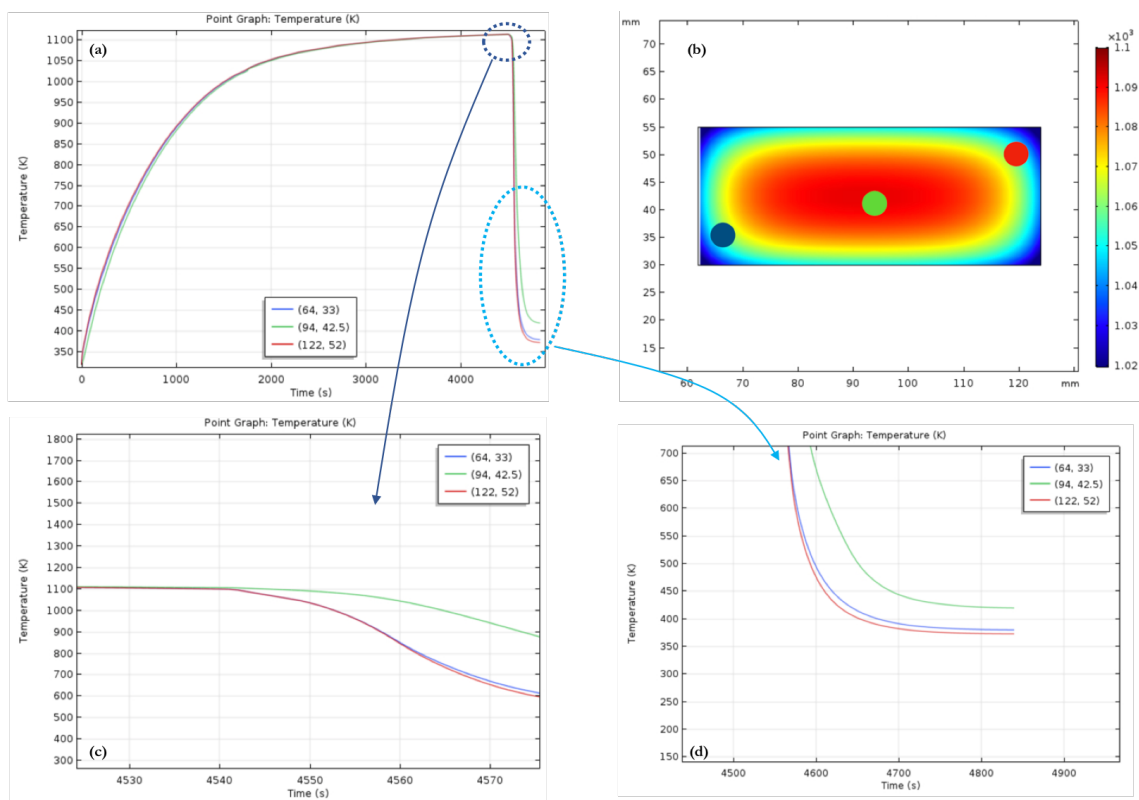


Figure 4.10: *Temperature analysis concerning the first simulation of Model1: (a) complete thermal cycle; (b) 2D temperature contour plot; (c) changing from heating to cooling phases; (d) cooling path of the evaluation points*

Fig. 4.4 (a) displays the whole thermal cycle developed by the part while Fig. 4.4 (c) and Fig. 4.4 (d) show the cooling paths determined for each detection point. It is notable that the inner and outer diameters cool down equally while the middle section reveals a different trend stemming from its absence of contact with the liquid medium and linked to the HTC selection.

Identical cooling paths lead to comparable microstructural results; inner and outer

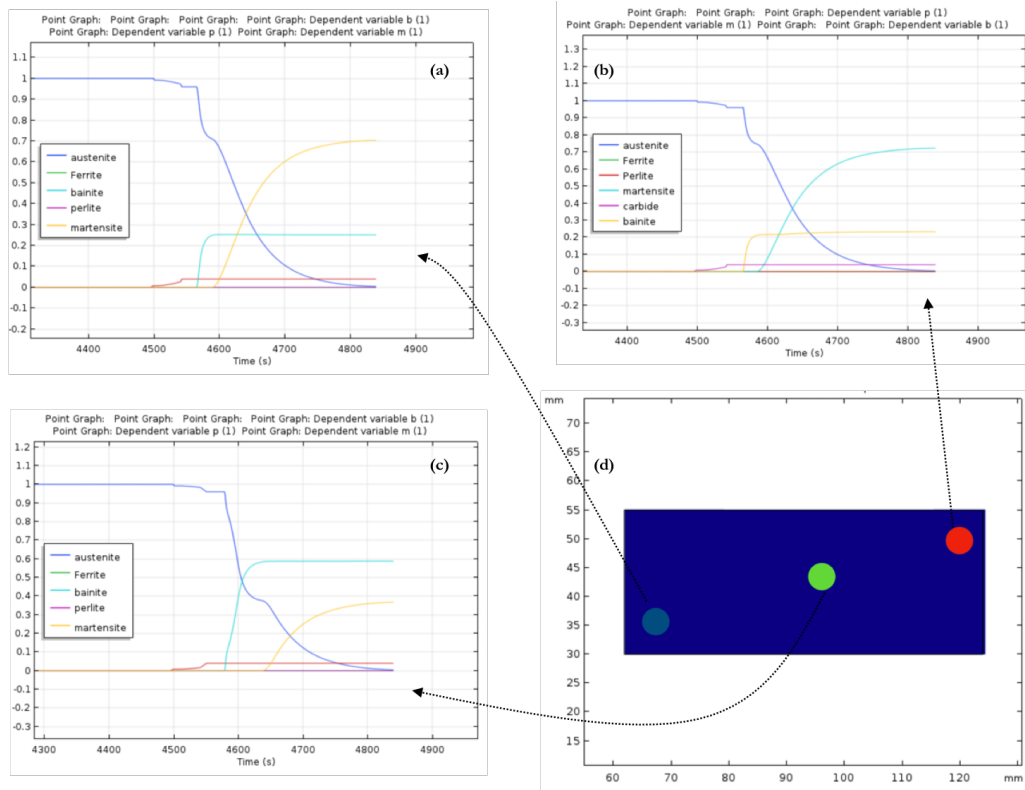


Figure 4.11: *Microstructural evolution concerning Modell: (a) internal, (b) external, (c) middle microstructural evolutions along the cooling phase, (d) detection points*

sections reveal similar microstructures with a relevant presence of martensite, (Fig. 4.11 (a) and Fig. 4.11 (b)) whereas a bainitic material phase is predicted for the middle section due to the slower cooling. This is visible in Fig. 4.11(c). Finally, radial and axial displacements were evaluated throughout the entire quenching cycle, portrayed in Fig. 4.12 and Fig. 4.13.

Taguchi Analysis Modell

The following section investigates the influences of HTC's on the outcomes using Taguchi Analysis, evaluating the final martensitic percentages as well as the radial displacement in the inner, middle and outer sections of the treated part. The martensite is linked to the modalities of the cooling and thus, it augments when the HTC's increase from 1500 to $4500 \frac{W}{m^2K}$. This can be considered a valid statement for all the detection points. The surface boundaries are strictly interconnected and influence the overall results across the whole section of the part. Fig. 4.14 portrays the HTC's influence on the inner martensitic percentages, whereas Fig. 4.15 and Fig. 4.16 display the behaviours of the middle and

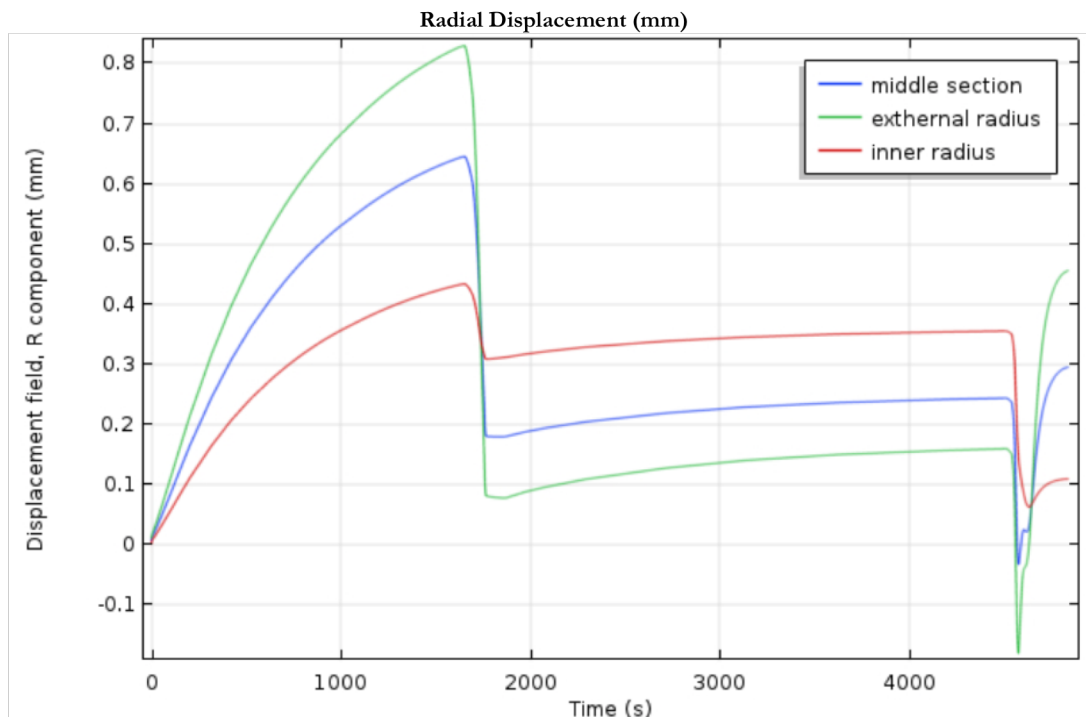


Figure 4.12: Evolution of radial displacements for internal, external and middle sections

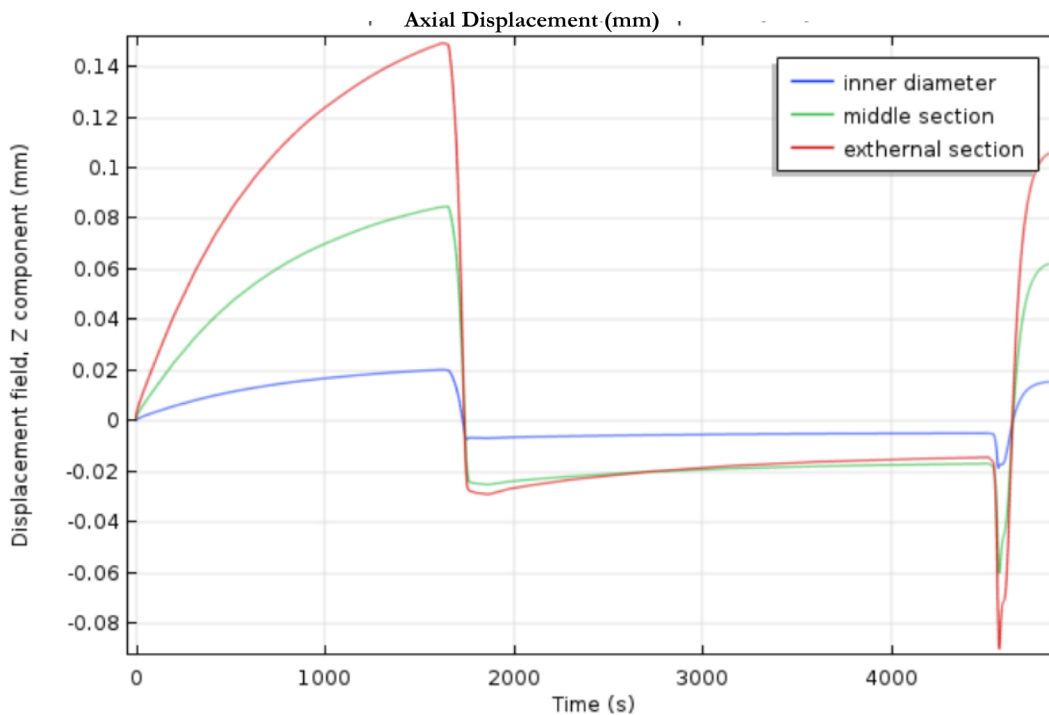


Figure 4.13: Evolution of axial displacements for internal, external and middle sections

the outer sections. In the same manner, HTC1 and HTC3 reduce the martensite for the middle section, Fig. 4.15. Neither HTC1 nor HTC3 has an effect on the outer martensitic

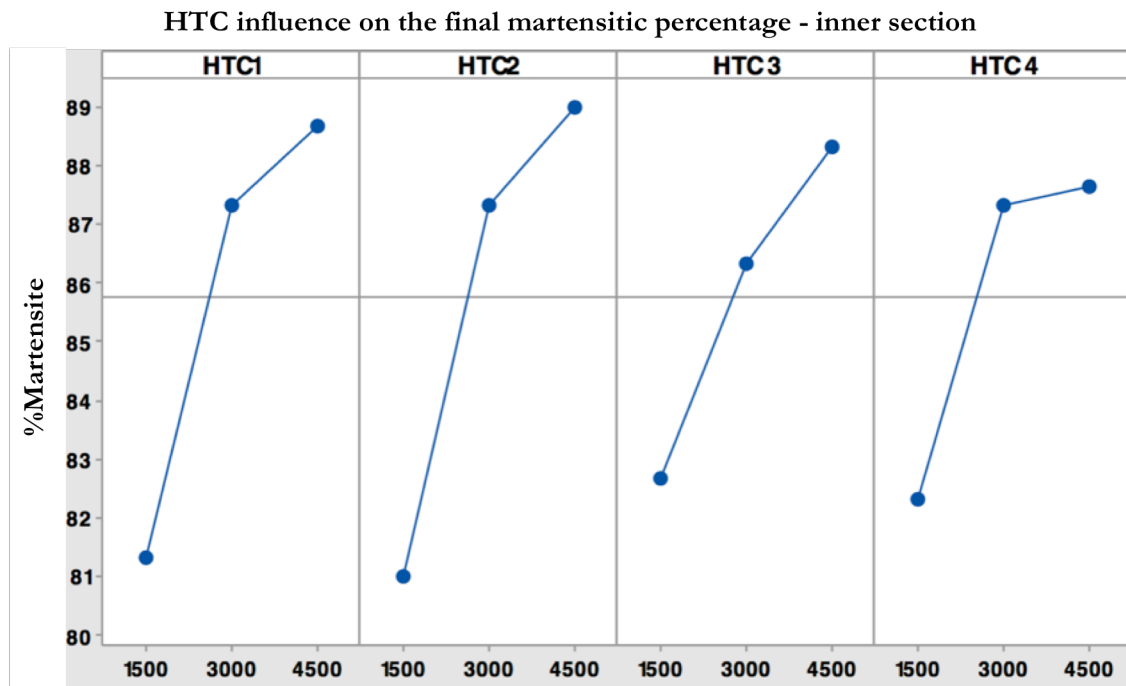


Figure 4.14: Influence of HTCs on the martensitic percentage taking into account the inner section

transformation, Fig. 4.16.

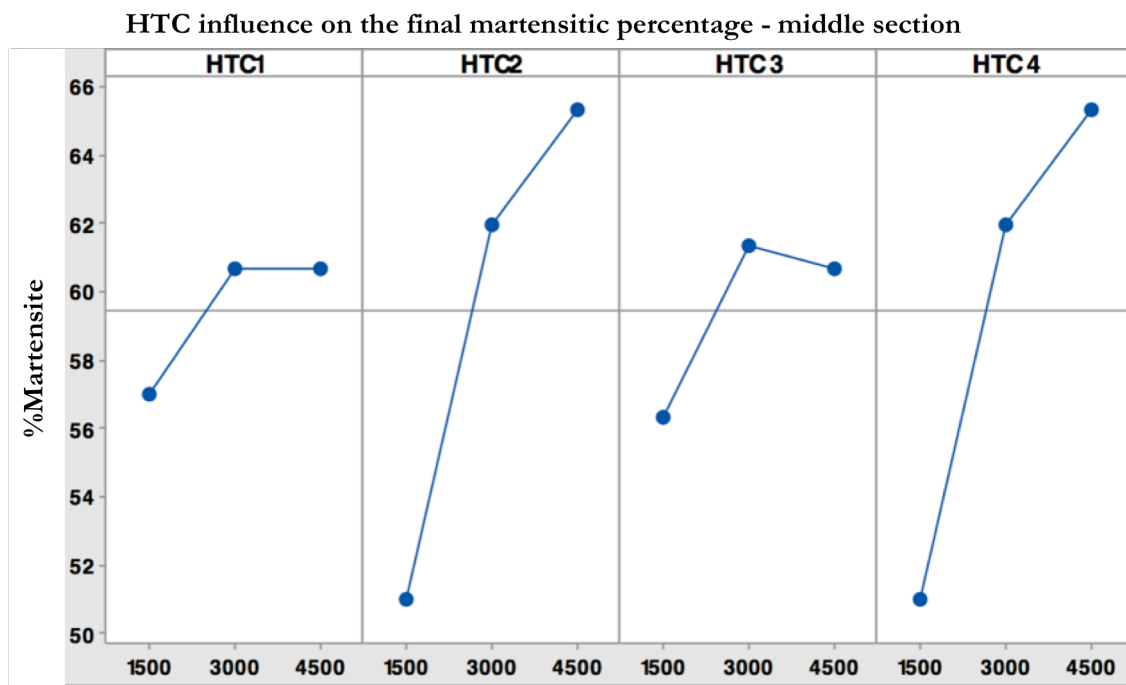


Figure 4.15: Influence of HTCs on the martensitic percentage taking into account the middle section

The results regarding the radial displacements are shown in Fig. 4.17, Fig. 4.18 Fig.

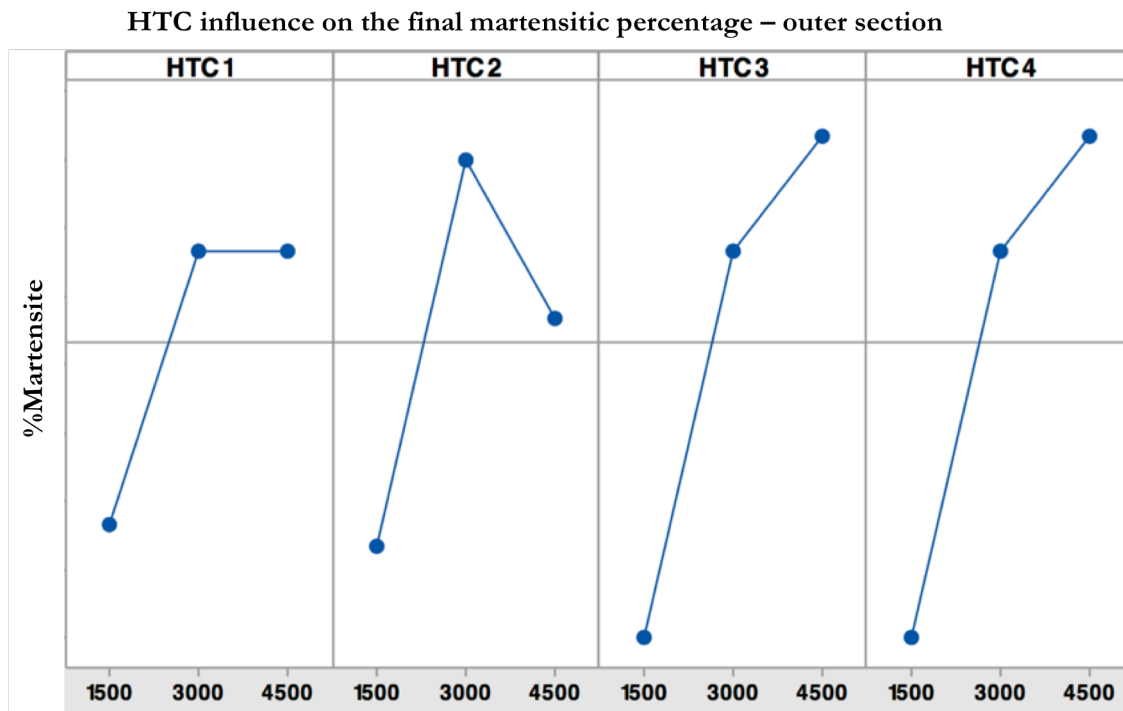


Figure 4.16: Influence of HTCs on the martensitic percentage taking into account the middle section

4.19. The displacements show decreasing trends from 1500 $\frac{W}{m^2K}$ to 4500 $\frac{W}{m^2K}$ for both the inner and middle sections. Conversely, the variations in the outer section of the part are negligible for HTC1, HTC2 and HTC3 while HTC4 produces the highest influence.

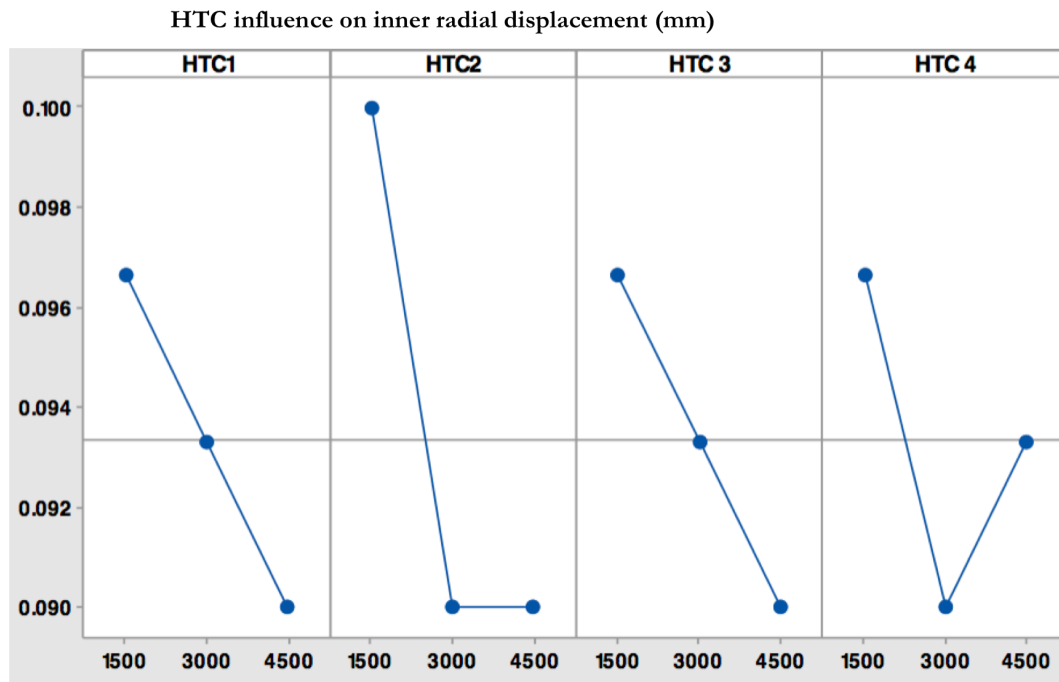


Figure 4.17: Influence of HTCs on the radial displacement in correspondence of the inner section

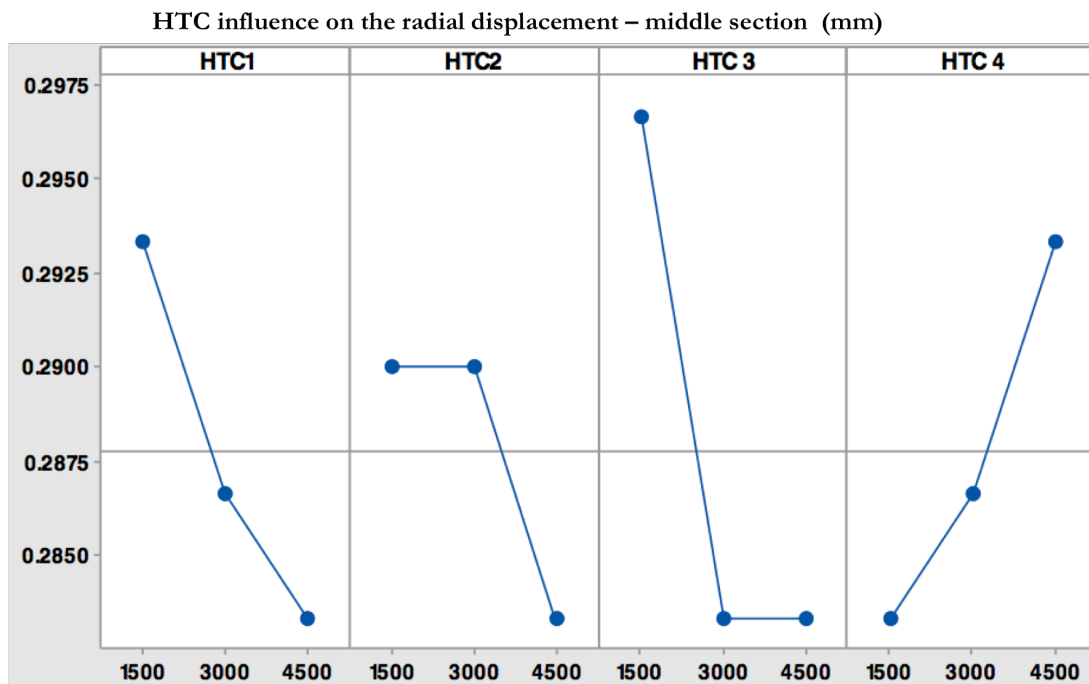


Figure 4.18: Influence of HTCs on the radial displacement in correspondence of the middle section

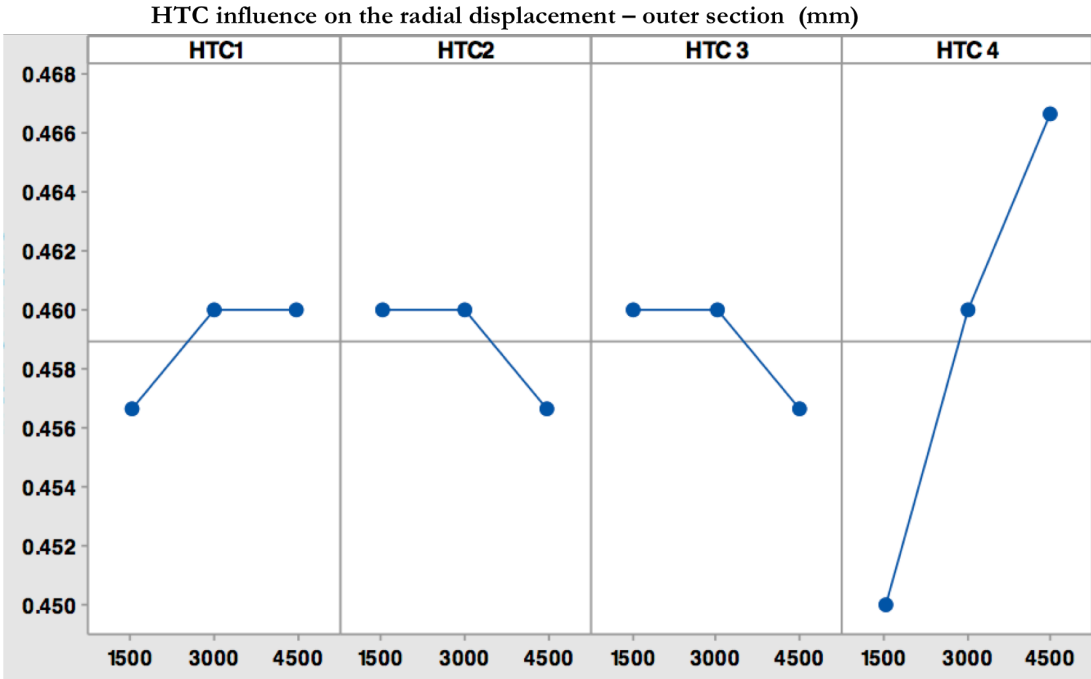


Figure 4.19: Influence of HTCs on the radial displacement in correspondence of the outer section

4.3.2 Investigation regarding Model2

Model 2 Results

This section illustrates the thermal, microstructural and deformation outcomes obtained by Model 2. As previously, a single simulation is first illustrated and then the whole range of results are examined using Taguchi Analysis to show the full outcomes and influence of each HTC. The seventh simulation was chosen at random and detailed. Temperature was firstly investigated, as presented in Fig. 4.20.

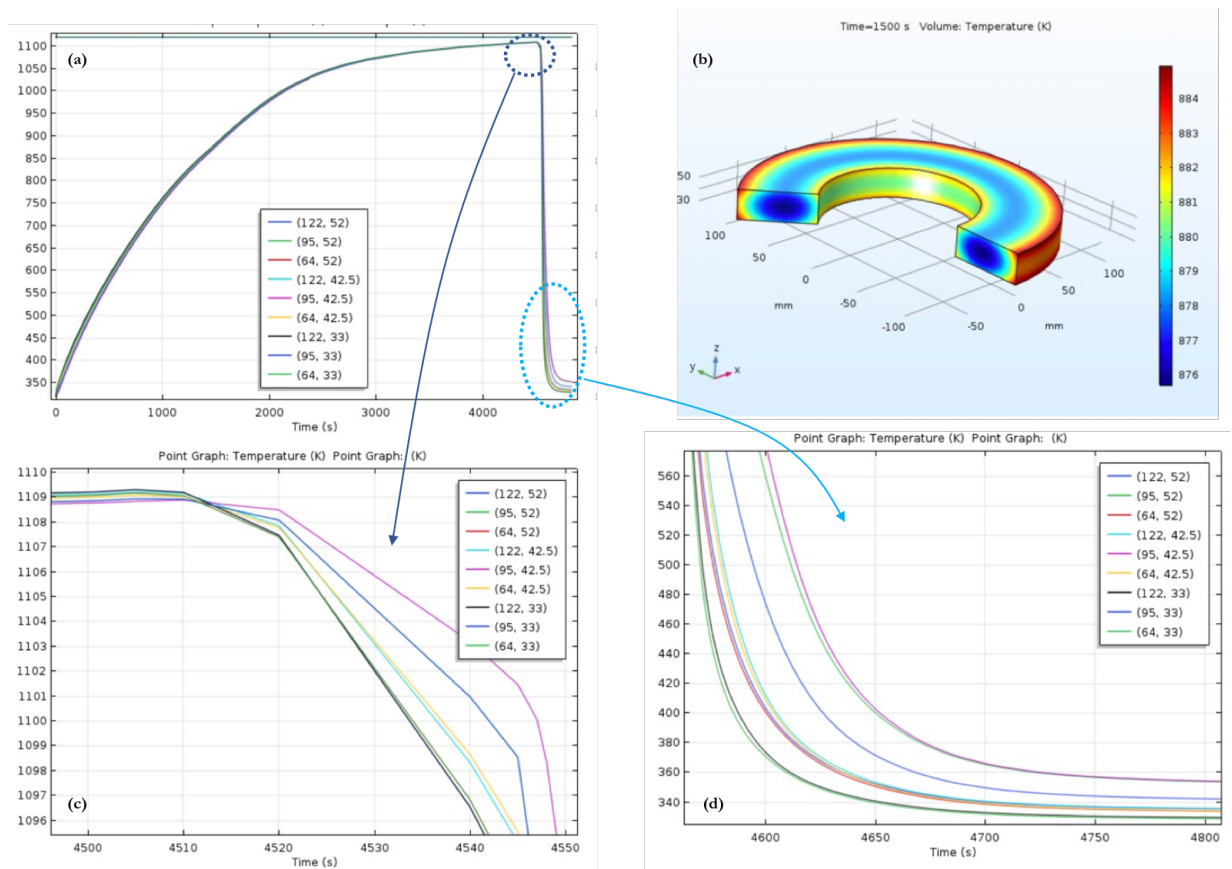


Figure 4.20: Temperature analysis concerning the seventh simulation of Model2: (a) complete thermal cycle; (b) 2D temperature contour plot; (c) changing from heating to cooling phases; (d) cooling path of the evaluation points

The microstructures were then detected, shown in Fig. 4.21. Each detection point was analysed and Fig. 4.21 (a), Fig. 4.21 (b) and Fig. 4.21 (c) display the microstructural evolutions in accordance with the detection points. A map of martensitic microstructure at the end of the quenching thermal cycle is shown in , Fig. 4.21 (d). The major martensitic percentages were obtained in the inner and outer section of the part where the cooling rates are higher than the core of the component.

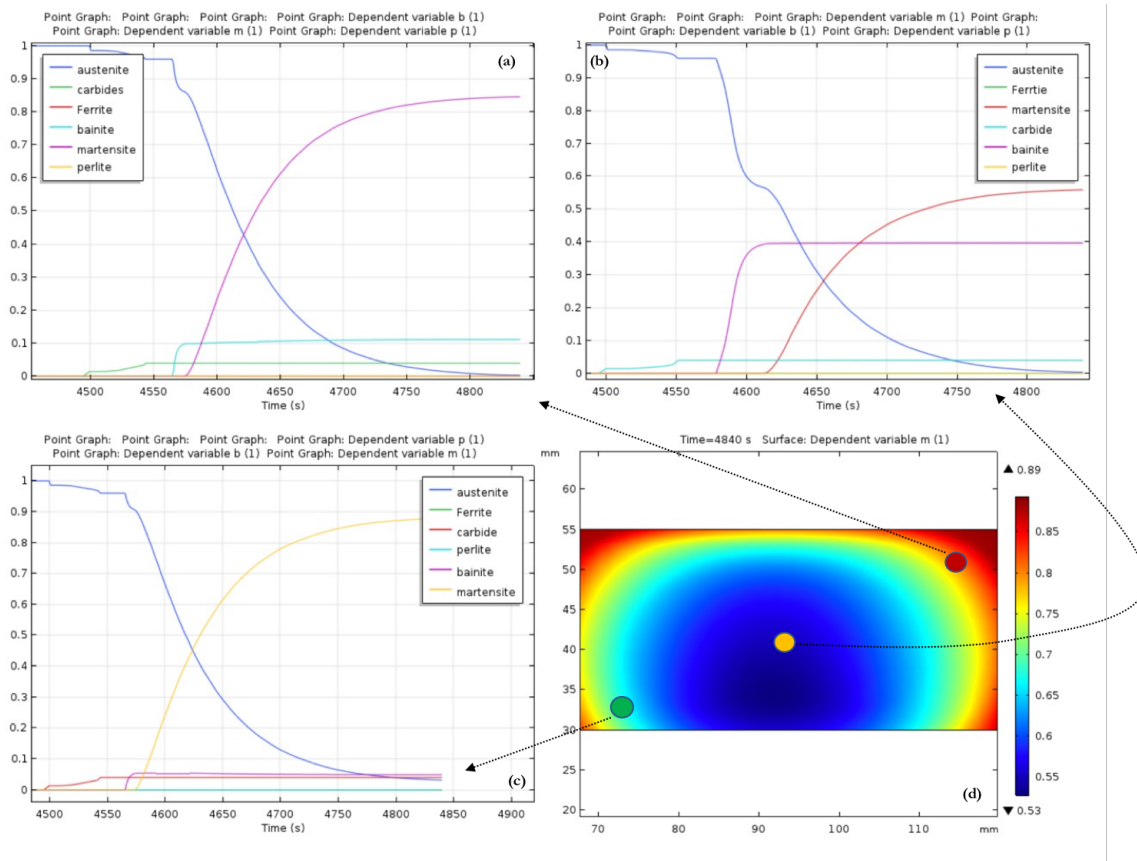


Figure 4.21: *Microstructural evolution concerning Model2: (a) internal, (b) external, (c) middle microstructural evolutions along the cooling phase, (d) detection points*

Finally, the displacements were assessed. The graphs display both the radial displacement in the different zones of the part and also the axial displacement, noting the deformations along the z axis. Fig. 4.22 and Fig. 4.23 show the dimensional developments of the cooling stage. The radial displacement is illustrated in Fig. 4.22. Fig. 4.23 reports the axial variations.

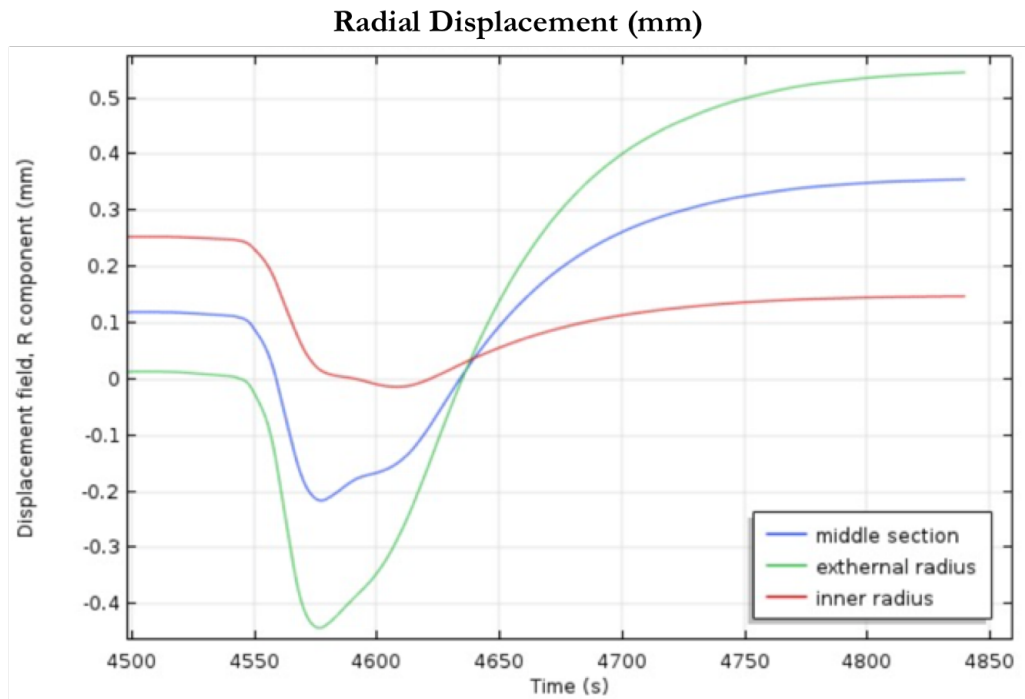


Figure 4.22: Evolution of radial displacements for internal, external and middle sections

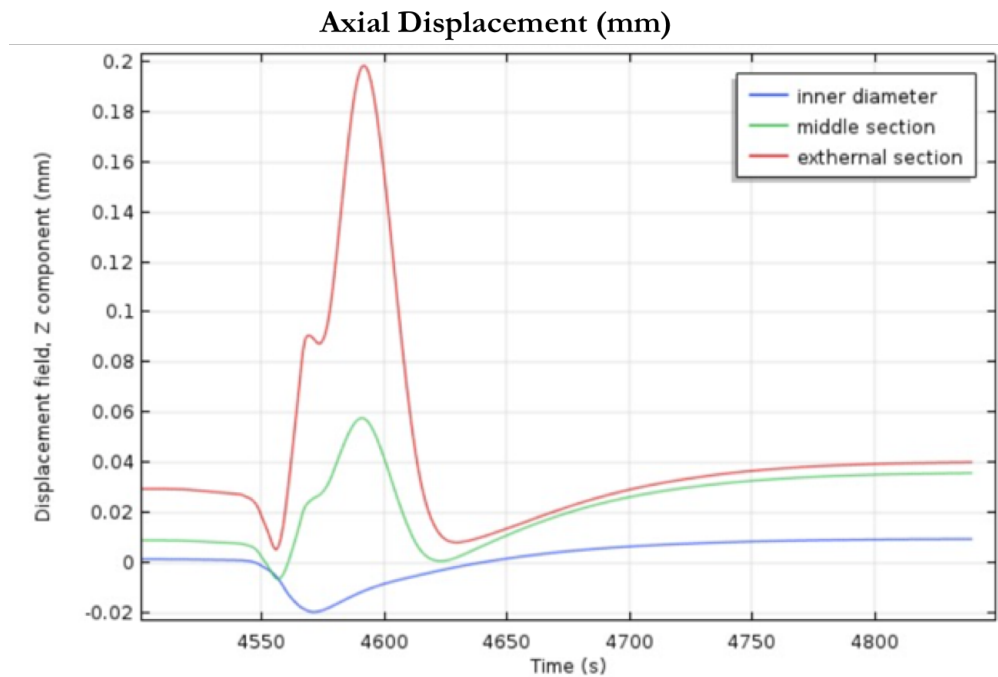


Figure 4.23: Evolution of axial displacements for internal, external and middle sections

Taguchi Analysis of Model 2

The following section investigates the influences of HTC's on the modelling results, using the Taguchi Analysis to consider all the simulations and individuate the effect of each

HTC on the outcomes.

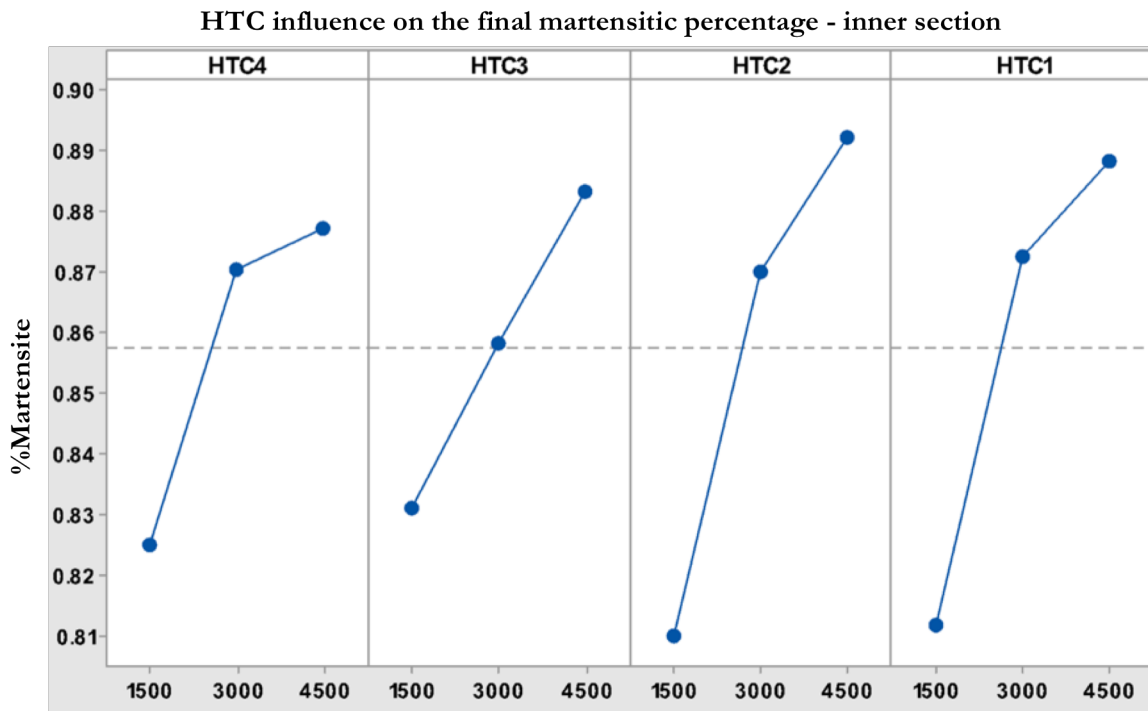


Figure 4.24: influence of HTCs on the martensitic percentage taking into account the inner section

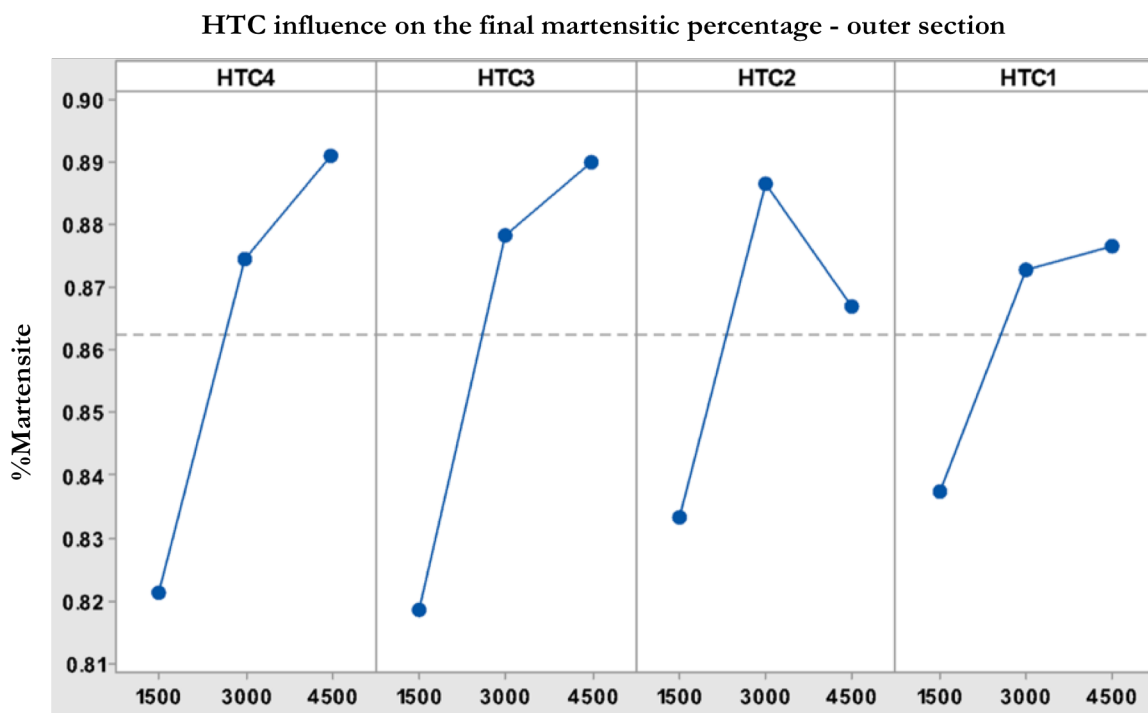


Figure 4.25: influence of HTCs on the martensitic percentage taking into account the outer section

The investigation evidences the increasing impact on martensitic percentages in both

the inner and outer section of the part. The displacement analysis determines a decreasing effect of HTC from $1500 \frac{W}{m^2K}$ to $4500 \frac{W}{m^2K}$. In short, the inner displacements decrease when HTCs increase, as seen in Fig. 4.26. The middle section is relevantly affected by HTC2 and HTC4 whereas HTC3 and HTC1 have less effect on the outcomes.

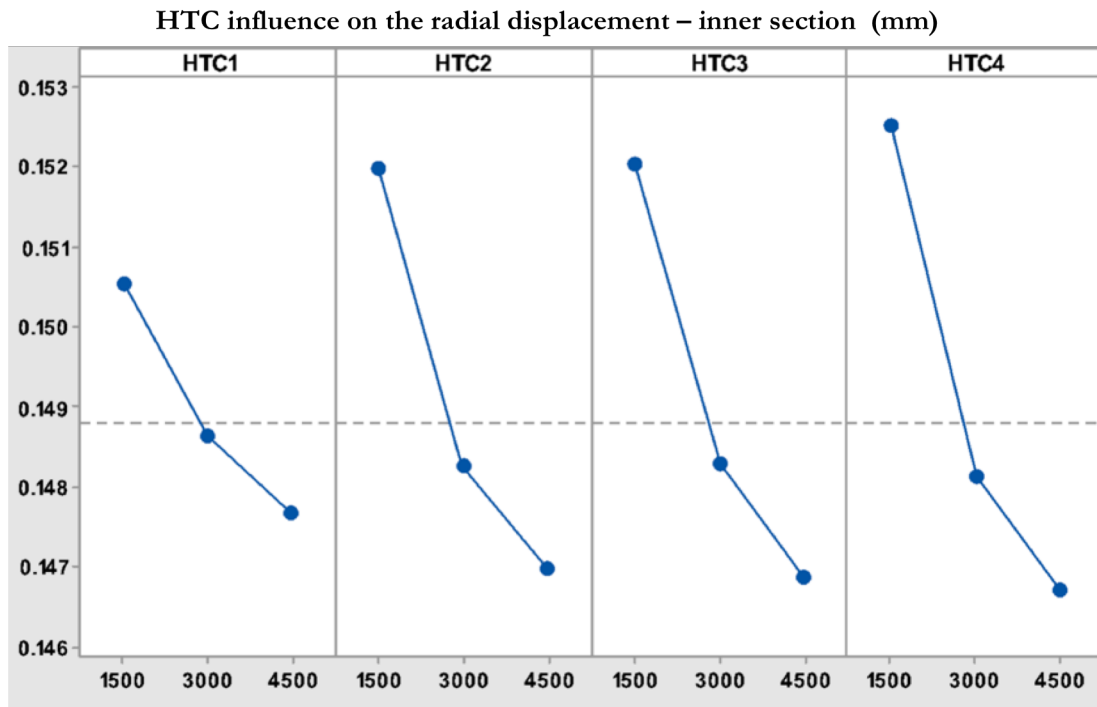


Figure 4.26: Influence of HTCs on the radial displacement in correspondence of the inner section

In addition, HTC1, HTC2, HTC3 show substantially the same effect from $\frac{W}{m^2K}$ to 4500 $\frac{W}{m^2K}$, while HTC4 has the highest influence on radial displacement regarding the outer section of the part.

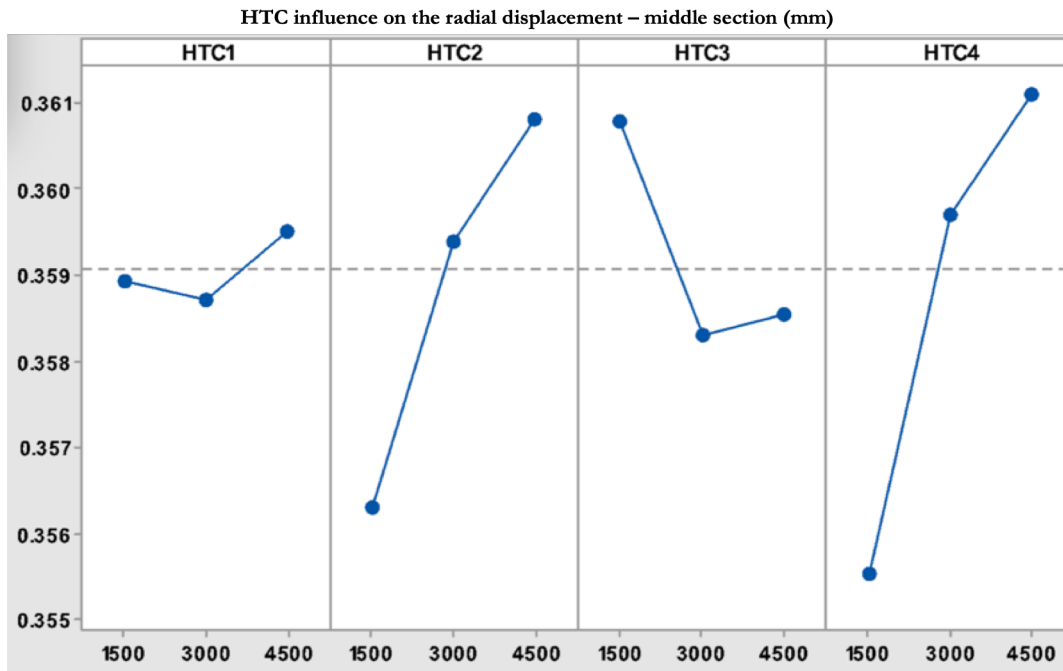


Figure 4.27: Influence of HTC's on the radial displacement in correspondence of the middle section

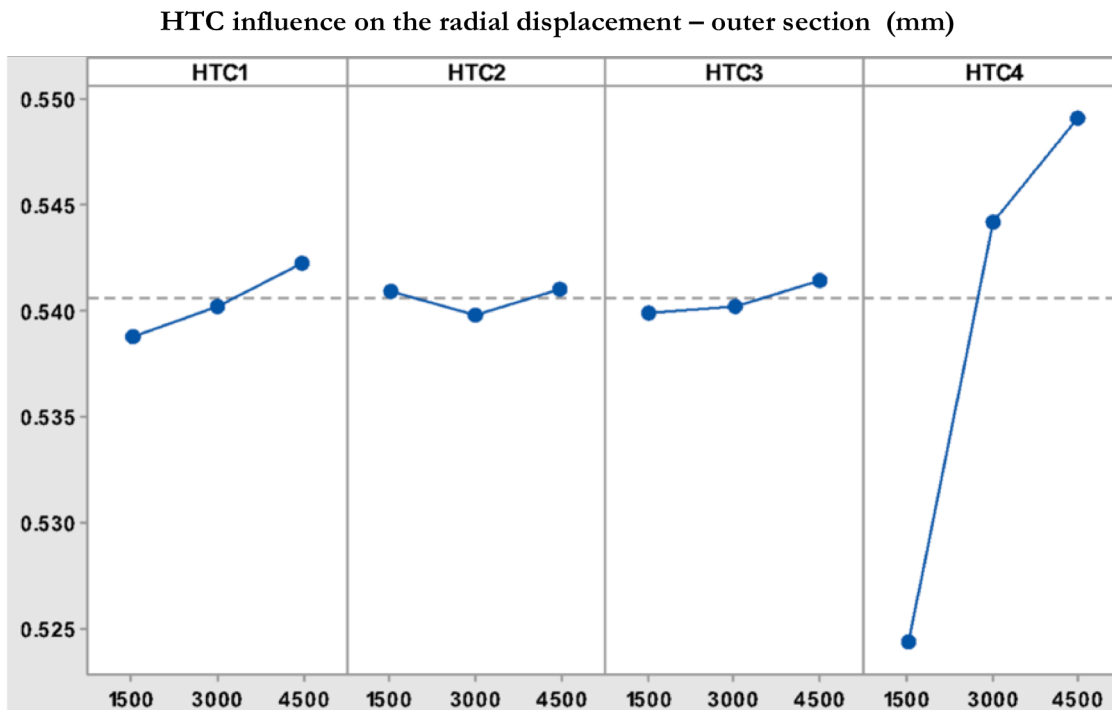


Figure 4.28: Influence of HTC's on the radial displacement in correspondence of the middle section

4.4 Modelling Conclusions

- In this chapter a comparison of the modelling activities and the physical experimentation was investigated. A multi-physical quenching modelling was successfully realised in order to evaluate the main heat treatment outcomes, looking at temperature, microstructures and displacements.
- The model was demonstrated to be an adequate instrument to replicate an actual quenching cycle through the definition of time-dependent interfaces regarding temperatures as well as HTC. The complete microstructural evolution was implemented and approximated the deformations induced by both thermal gradients and material microstructures.
- Regarding the traditional quenching process, the model was able to replicate the inner diameter trends derived from the experimental activity. Negative deformation was also predicted and showed an overlap between real and virtual concerning the null value of radial displacement.
- The modelling outcomes were always affected by the HTC and different results can be obtained through the setting of diverse magnitudes, replicating multiple in-process conditions. With a combination of experiments and modelling activities, the pressure effect for DAOQ can be realised and incorporated by the specific definition of heat transfer coefficients.

Conclusions

A comprehensive investigation into quenching processes was carried out in order to assess and improve the sustainability of the operation in its various forms. Multi-physical modelling and physical experiments were conducted to analyse the quenching processes and focus on the determining of dimensional and shape variations. Die assisted oil quenching (DAOQ) was rigorously tested, compared with the more commonly used Oil-assisted process and shown to be a superior solution in terms of final part precision and the energy and raw material savings that this implies. DAOQ produced a more effective martensitic transformation and this resulted in better overall control of the part geometry and reduced main dimensional variations and planarity tolerances.

DAOQ leads to a precise form of the treated part through a replicable and reliable quenching process; thanks to the combined effect of the press&mould, an accurate quenching stage can be performed. Its drawback, however, is the increased complexity of the whole operation. A more complex tuning process is required due to the regulation of multiple process parameters and more time and precision must be dedicated to the creation of the die design. Nevertheless, the DAOQ technique can significantly reduce machining allowances, reducing or even eliminating the need for post quenching machining operations, which shortens the technological cycle and saves energy, time and materials. The process is particularly suitable for high-value components such as gears or bearing rings that require complex post-quenching machining operations. The achievement of the final design in terms of dimensions and mechanical properties can be directly obtained using DAOQ.

Further measures to increase the sustainability of this sector were found in the choice of the liquid medium. Through comparative experimentation, the vegetable quenching oil

was proved to be more effective than the petroleum-based one used as industry standard, both in the achievement of mechanical, dimensional and metallurgical requirements and in the greatly reduced impact it has on the environment.

To conclude, the adoption of the die-assisted oil quenching process in combination with the use of vegetable oil based mediums can be considered as a solid starting point for this industry sector to improve sustainability and strive for implementation of the 6R concepts. The advancement of virtualising technology can also play a role in these aims. The prediction of manufacturing effects and side effects can provide invaluable assistance to the product design phase, helping improve and streamline the entire technological chain.

Future developments of this research will involve continued refinements to the virtualisation with incorporation of the carburising material into the multi-physical modelling, further testing of the realised model in an actual industrial application and the realisation of experimental investigations into a range of different manufacturing cycles.

Bibliography

- [1] Jovane, F., Yoshikawa, H., Alting, L., Boër, C.R., Westkamper, E., Williams, D., Tseng, M., Seliger, G., and Paci, A.M. (2008). The incoming global technological and industrial revolution towards competitive sustainable manufacturing. *CIRP Annals*, 57, 641–659.
- [2] International European agency (IEA). (2015). Key Trends and CO2 Emissions Excerpt from: CO2 Emissions from Fossil Fuels. Available at: www.iea.org.
- [3] Hapuwatte, B.M., Badurdeen, F., Jawahir I.S. (2017). Metrics-based Integrated Predictive Performance Models for Optimized Sustainable Product Design. *Smart Innovation Systems and Technologies* 68, 25-34.
- [4] United Nations General Assembly, (11 December 1987). Report of the World Commission on Environment and Development, A/RES/42/187, 96th Plenary Meeting.
- [5] Jayal, A.D., Badurdeen, F., Dillon, Jr, O.W., Jawahir, I. S. (2010). Sustainable manufacturing: Modelling and optimization challenges at the product, process and system levels. *CIRP Journal of Manufact. Science and Tech.*, 2 (3), 144-152.
- [6] Jawahir, I.S., Dillon, O.W. (2007). Sustainable Manufacturing Processes: New Challenges for Developing Predictive Models and Optimization Techniques. In: *Proceedings of the 1st International Conference on Sustainable Manufacturing*, 1-19.
- [7] Jawahir, I.S., Badurdeen, F., Rouch, K.E. (2013). Innovation in sustainable manufacturing education. In: Seliger, G. (ed.) *Proceedings of the 11th Global Conference on Sustainable Manufacturing (GCSM)*, 9–16, 23–25 September, Berlin, Germany.

- [8] Dornfeld, D.A. (2013). Green manufacturing: fundamentals and applications. Springer, New York, NY.
- [9] Joshi, K., Venkatachalam, A., Jawahir, I.S. (2006). A New Methodology for Transforming 3R Concept into 6R Concept for Improved Product Sustainability. In: Proceedings of the IV Global Conference on Sustainable Product Development and Life Cycle Engineering, 3-6.
- [10] Jaafar, I.H., Venkatachalam, A., Joshi, K., Ungureanu, A.C., De Silva, N., Dillon Jr O.W., Rouch, K.E., Jawahir, I.S. (2007). Product Design for Sustainability: A New Assessment Methodology and Case Studies. In: Kutz M, (Ed.) Handbook of Environmentally Conscious Mechanical Design. John Wiley & Sons, 25– 65.
- [11] Despeisse, M., Davé, A., Litos, L., Roberts, S., Ball, P., Evans, S. (2016). A collection of tools for factory eco-efficiency. *Procedia CIRP*, 40, 542-546.
- [12] Bilge, P., Badurdeen, F., Seliger, G., Jawahir, I.S. (2015). Conceptual modelling of interactions among value creation factors for improved sustainable value creation. *Int. Journal of Strategic Eng. Asset Management*, 2 (3), 287-311.
- [13] Garetti, M., and Taisch, M. (2012). Sustainable manufacturing: trends and research challenges. *Production Planning & Control* 23, 83–104.
- [14] Bilge, P., Emec, S., Seliger, G. (2017). Leverage of Industrial Engineering Education for Sustainable Manufacturing. *Smart Innovation Systems and Technologies* 68, 3-12.
- [15] Shuaib, M., Seevers, D., Zhang, X., Badurdeen, F., Rouch, K.E., and Jawahir, I.S. (2014). Product Sustainability Index (ProdSI): A Metrics-based Framework to Evaluate the Total Life Cycle Sustainability of Manufactured Products. *Journal of Industrial Ecology*, 18, 491–507.
- [16] MacKenzie, D.S. (2003). Advances in Quenching-A Discussion of Present and Future Technologies. In *Heat Treating And Surface Engineering: Proceedings of the 22nd Heat Treating Society Conference and the 2nd International Surface Engineering Congress*, 228-239, 15-17 September, Indianapolis, Indiana, USA, .

- [17] Heat Treatment Problems Associated with Design and Steel Selection, Heat Treating of Irons and Steels. ASM Handbook, ASM International, 4D 3–28.
- [18] Canale, L.C.F., Vatauvuk, J., Totten, G.E., Luo, X. (2014). Problems Associated with Heat Treating. Steel Heat Treating Technologies. ASM Handbook, ASM International, 4B, 29–73.
- [19] Lübben, T., (2014). Basics of Distortion and Stress Generation during Heat Treatment. Steel Heat Treating Technologies. ASM Handbook, ASM International, 4B, 339–354.
- [20] MacKenzie, D.S. Metallurgical Aspects of Distortion and Residual Stresses in Heat Treated Parts. In: Proceedings of the 23rd IFHTSE Heat Treatment and Surface Engineering Congress 18-21.
- [21] Canale, L.C.F., and Totten, G.E. (2005). Quenching technology: a selected overview of the current state-of-the-art. Materials Research 8, 461–467.
- [22] Campana, G., Lenzi, F., Melosi, F., and Zanotti, A. (2017). Sustainability of Die-Assisted Quenching Technology and Comparison with Traditional Processes. Smart Innovation Systems and Technologies 68, 162–171.
- [23] Jones, L.E. (1994). Fundamentals of Gear Press Quenching, Lindberg Technical & Management Services Group Charlotte, NC.
- [24] Narazaki, M., Totten, G.E., Webster, G.M. (2013). Hardening by Reheating and Quenching. Approved by the ASM Handbook Committee for addition to the ASM Handbook Supplements Online, Distortion and Residual Stress, ASM International.
- [25] ASM Handbook, (2013). Press Quenching, Steel Heat Treating Fundamentals and Processes, ASM Int., Vol. 4A 252-256.
- [26] Gupta, K., Laubscher, R.F., Davim, J.P., and Jain, N.K. (2016). Recent developments in sustainable manufacturing of gears: a review. Journal of Cleaner Production 112, 3320–3330.
- [27] Totten, G.E., Dossett, J.L., Kobasko, N.I., Dossett, J. (2013). Quenching of Steel. ASM Handbook, 4, 91-157.

- [28] Kerekes, G., Baan, M.K., Felde, I. (2016). Possibility of use of bio oils as quenchant. In: Proceedings. of the Int. Multidisciplinary Scientific Conference, 10.26649/musci.2016.082, University of Miskolc, Hungary, 21-22 April.
- [29] Nebbe, J., Mackenzie, D.S. (2015). Application Of Vegetable-Based Quench Oil To Achieve Safety And Environmental Advantages. In: Proceedings of the 28th ASM Heat Treating Society Conference, 20–22 October, Detroit, Michigan, USA.
- [30] Raimondi, A., Girotti, G., Blengini, G.A., Fino, D. (2012). LCA of petroleum-based lubricants: state of art and inclusion of additives. *Int. J. of Life Cycle Assessment*, 17 (8), 987-996.
- [31] Souza, E.C., Fernandes, M.R., Augustinho, S.C.M., Canale, L.C.F., Totten, G.E. (2009). Comparison of Structure and Quenching Performance of Vegetable Oils. *J. ASTM International*, 6 (9), JAI 102188.
- [32] Davis J.R., (1992). *ASM Materials Engineering Dictionary*, ASM International, 407.
- [33] MacKenzie, D.S. (2017). Understanding the cooling curve. *Thermal Processing Magazine*, 2, 28-32.
- [34] Lenzi, F., Campana, G., Lopatriello, A., Mele, M., Zanotti, A. (2018). About the use of mineral and vegetable oils to improve the sustainability of steel quenching, 16-th Global Conference on Sustainable Manufacturing, 2-4 October 2018, city of Lexington, USA.
- [35] Mourtzis, D., Doukas, M., Bernidaki, D. (2014). Simulation in manufacturing: Review and challenges. *Procedia CIRP*, 25, 213-229.
- [36] Rao, S.S. (2017). *The finite element method in engineering*. Butterworth-Heinemann
- [37] Xiao, G., Di, H., Zhu, F., Chen, B., Qiu, B. (2010). Influence of direct quenching on microstructure and mechanical properties of steel plate for large oil storage tanks. *Journal of materials engineering and performance*, 19, 868-872.
- [38] Kaymak, Y., (2007). Simulation of Metal Quenching Processes for the Minimization of Distortion and Stresses. *Otto-von-Guericke-Universität Magdeburg*, Magdeburg.

- [39] Nejad, R. M., Shariati, M., Farhangdoost, K. (2017). Three-dimensional finite element simulation of residual stresses in UIC60 rails during the quenching process. *Thermal Science*, 21, 1301-1307.
- [40] Şimşir, C., Gür, C.H. (2008). 3D FEM simulation of steel quenching and investigation of the effect of asymmetric geometry on residual stress distribution. *Journal of Materials Processing Technology*, 207 (1-3), 211-221.
- [41] Oliveira, W.P., Savi, M.A., Pacheco, P.M.C. (2013). Finite element method applied to the quenching of steel cylinders using a multi-phase constitutive model. *Archive of Applied Mechanics*, 83, 1013-1037.
- [42] Dossett, J., Totten, G.E. (2014). Modeling and Simulation of Steel Heat Treatment—Prediction of Microstructure, Distortion, Residual Stresses, and Cracking. *Steel Heat Treating Technologies*, ASM Handbook, ASM International, 4B, 409-466.
- [43] Fasano, A., Hömberg, D., Panizzi, L., (2009). A mathematical model for case hardening of steel, *Mathematical Models and Methods. Applied Sciences*, 19 (11), 2101-2126.
- [44] Ramberg, W., Osgood, W.R. (1943). Description of stress-strain curves by three parameters. *National advisory committee for aeronautics*, 902.
- [45] Beswick, J. M. (2007). Bearing steel technology: Advances and state of art in bearing steel quality assurance. *ASTM International*, 7 (1465), 250-257.
- [46] Wolff, M., Acht, C., Böhm, M., Meier, S. (2007). Modelling of carbon diffusion and ferritic phase transformations in an unalloyed hypo-eutectoid steel. *Archives of Mechanics*, 59 (4-5), 435-466.
- [47] Lenzi, F., Campana, G., Zanotti, A. (2017). A multi-physics approach to model a Die Assisted Oil Quenching process. In: *Proceedings accepted for the oral session at the international CAE conference*, 6-7 November, Vicenza, Italy.
- [48] Freborg, Li, Z., Ferguson, A.M., Ding, B.L.P., and Hebbes, M. (2016). Press Quench Process Design for a Bevel Gear using Computer Modelling. In: *Proceedings of the 23rd IFHTSE Heat Treatment and Surface Engineering Congress*, 78-87.

- [49] Nallathambi, A.K., Kaymak, Y., Specht, E., and Bertram, A. (2010). Sensitivity of material properties on distortion and residual stresses during metal quenching processes. *Journal of Materials Processing Technology*, 210 (2), 204–211.
- [50] Felde, I., Simsir, C. (2014) Simulation Trends in Quenching Technology for Automotive Components. *International Heat Treatment and Surface Engineering*, 8 (1), 42–48.
- [51] Zhichao, L., Ferguson, B.L., Sims, J., and Yu, T. (2017). Sources of Distortion Study during Quench Hardening Using Computer Modelling. In: *Proceedings of the 29th ASM Heat Treating Society Conference*, 24-26 October, Columbus, Ohio, USA.
- [52] Zhang, Y., Shi, W., Yang, L., Gu, Z., and Li, Z. (2016). The Effect of Hardenability Variation on Phase Transformation of Spiral Bevel Gear in Quenching Process. *Journal of Materials Engineering and Performance* 25 (7), 2727–2735.
- [53] Reardon, A.C., Freborg, A., Li, Z.C., and Ferguson, B.L. Understanding Process Sensitivities in Press Quenching: An Integrated Approach. In: *Proceedings of the 28th ASM Heat Treating Society Conference* 233-251.
- [54] Board, U.S. (2013). Life cycle impact of soybean production and soy industrial products.
- [55] Schneider, L., Finkbeiner, M. (2013). Life Cycle Assessment of EU Oilseed Crushing and Vegetable Oil Refining, Report, Technische Universitaet Berlin, Berlin, Germany.
- [56] Montgomery, D.C., Runger, G.C. (2010). *Applied statistics and probability for engineers*. John Wiley-Sons.
- [57] Buczek, A., and Telejko, T. (2013). Investigation of heat transfer coefficient during quenching in various cooling agents. *International Journal of Heat and Fluid Flow* 44, 358–364.
- [58] Ferioli, E. G. T. T., Rivoli-To, G. S. Drasticità di tempra dei gas e dei liquidi a confronto.

- [59] Petta, D., Trombini, F. Toffanin, L., Micheletti, I., Ghidini, A. (2010). Scelte ottimizzate di trattamento termico nel rispetto di Sicurezza ed Ambiente. *La Metallurgia Italiana*, 4, 9-19.
- [60] Lenzi, F. Campana, G. Zanotti, A. (2018). An experimental comparison between traditional and die assisted quenching manufacturing processes aided by multi-physical modelling, accepted for the oral session at the XXVI Convegno Nazionale Trattamenti Termici, 16 June, Mestre, Venice, Italy.
- [61] Campana, G. Lenzi, F., Zanotti, A. (2016). Modellazione del processo di tempra libera per un acciaio ad alto contenuto di carbonio. In: *Proceedings of the 36° Convegno Nazionale AIM*, 21-23 September, Parma, Italy.